Evaluation of Halogen-Free Laminates Used in Handheld Electronics

by

David Yuk Ho Lau

A thesis
presented to the University of Waterloo
in fulfillment of the
thesis requirement for the degree of
Master of Applied Science
in
Mechanical Engineering

Waterloo, Ontario, Canada, 2009

© David Yuk Ho Lau 2009

AUTHOR'S DECLARATION

I hereby declare that I am the sole author of this thesis. This is a true copy of the thesis, including any required final revisions, as accepted by my examiners.

I understand that my thesis may be made electronically available to the public.

Abstract

The purpose of this study is to examine the thermal and mechanical properties of various halogen-free laminates used in handheld electronic products and to correlate these properties to the manufacturing requirements and mechanical performance. Thermal properties determined for the laminates are the glass transition temperature, x,y,z-axis CTE, time to delamination at 260˚C and 288˚C, temperature to decomposition and interconnect stress test. SEM and EDS mapping analyses have been done on the laminates to determine the chemical composition and area fraction of the filler used in the epoxy. Three different fillers are identified from the laminates: $Al(OH)_3$, $Mg(OH)_2$, SiO_2. Results show that the SiO_2 fillers presented in the laminates reduce the z-axis CTE changes and increase the time to delamination. The x and y axis CTE is found to be lower than the z-axis CTE due to the glass fibers reinforcement in both the x and y directions. The temperature to decomposition is dependent on both the fillers and epoxy chemistry. $Al(OH)_3$ starts to decompose above 200˚C and increases the rate of decomposition at 260˚C. Its decomposition also leads to an increase in z-axis CTE above 240˚C. Interconnect stress test results show that laminates with higher temperature to decomposition exhibit longer cycles to failure.

Mechanical test results indicate that the halogenated laminates without fillers perform better than the halogen-free laminates with fillers. High fillers loading increase the flexural modulus and Vickers hardness properties of the laminates but decrease both the flexural strength and energy to fracture. Silica fillers in particular are susceptible to weaken these mechanical properties. Laminates without any fillers show plastic deformation of the epoxy matrix after fracture and result in a high energy to fracture. The adhesion of fillers to the matrix is important as the better the adhesion the higher the flexural strength is for the laminates. Results show that laminates with $Al(OH)_3$ as the major filler have higher flexural strength than laminates with silica fillers, which also demonstrates that adhesion of the $Al(OH)_3$ fillers are better than the silica. Laminates without any filler have higher copper peel strength than laminates with fillers.

Acknowledgements

I would like to thank my academic supervisor, Dr. Y. Norman Zhou and my industrial supervisor, Dr. Laura Turbini for their time, guidance, support and assistance for this study. I would also like to thank Dr. Julie Liu and Madusha Cooray at Research in Motion for their training on laboratory equipment to conduct the experiments in my research.

Financial contributions to this research projects from both the Natural Science and Engineering Research Council of Canada (NSERC) Industrial Postgraduate Scholarship and Research in Motion are acknowledged.

Also, I would like to thank the members from the Materials Interconnect Lab and the Centre for Advanced Materials Joining (CAMJ) for all their contributions to this project.

Table of Contents

List of Figures ... vii

List of Tables ... xi

Chapter 1 INTRODUCTION ... 1

1.1 Driving force for halogen-free ... 1

1.2 Traditional FR-4 laminates ... 1

1.3 Flame retardants substitutes ... 1

1.4 Handheld Electronics ... 3

1.5 Objective ... 4

1.5.1 Manufacturing based parameters ... 4

1.5.2 Performance based parameters ... 5

Chapter 2 LITERATURE REVIEW ... 6

2.1 Role of each component in laminates ... 6

2.2 Effects of fillers and epoxy on thermal properties of composites ... 10

2.2.1 Coefficient of Thermal Expansion ... 10

2.2.2 Delamination ... 12

2.2.3 Decomposition ... 13

2.2.4 Interconnect stress test (IST) ... 15

2.3 Effects of fillers on mechanical properties of composites ... 17

2.3.1 Tensile strength ... 17

2.3.2 Modulus of elasticity ... 19

2.3.3 Toughness ... 20

2.4 Summary ... 21

Chapter 3 EXPERIMENTAL METHODS ... 22

3.1 Fillers and epoxy characterization ... 22

3.1.1 SEM and Mapping Analysis ... 22

3.1.2 Image Analysis ... 24

3.2 Thermal properties analysis ... 25

3.2.1 Glass transition temperature (T_g) ... 26

3.2.2 Coefficient of Thermal Expansion (CTE) in x, y, z-axis ... 30

3.2.3 Time to delamination (T260 and T288) ... 32

3.2.4 Temperature to decomposition (T_d) ... 34

3.2.5 Interconnect stress test (IST) 36
3.3 Mechanical properties analysis 37
3.3.1 Flexural strength 37
3.3.2 Energy to fracture 39
3.3.3 Flexural modulus 39
3.3.4 Vickers hardness 41
3.3.5 Copper peel strength 42
3.4 Electrical properties 43
Chapter 4 RESULTS 44
4.1 Chemical and physical analysis on epoxy and fillers 44
4.1.1 Epoxy characterization 44
4.1.2 Fillers characterization 46
4.2 Thermal properties analysis 49
4.2.1 Glass transition temperature (T_g) 49
4.2.2 Coefficient of Thermal Expansion (CTE) 49
4.2.3 Time to delamination 51
4.2.4 Temperature to decomposition (T_d) 54
4.2.5 Interconnect stress test (IST) 55
4.3 Mechanical properties analysis 57
4.3.1 Flexural strength 57
4.3.2 Energy to fracture 57
4.3.3 Flexural modulus 58
4.3.4 Vickers hardness 59
4.3.5 Copper peel strength 60
4.4 Electrical properties 60
Chapter 5 DISCUSSION 62
5.1 Thermal analysis and correlation with fillers and epoxy properties 62
5.1.1 Glass transition temperature (T_g) 62
5.1.2 Coefficient of thermal expansion (CTE) 63
5.1.3 Time to delamination 70
5.1.4 Temperature to decomposition (T_d) 73
5.1.5 Interconnect stress test (IST) 75

5.2 Mechanical analysis and correlation with fillers properties 77
5.2.1 Flexural strength 77
5.2.2 Energy to fracture 80
5.2.3 Flexural modulus 81
5.2.4 Vickers hardness 82
5.2.5 Copper peel strength 83
5.3 Summary 83
Chapter 6 CONCLUSION 85
6.1 Materials evaluation based on thermal properties 85
6.2 Materials evaluation based on mechanical properties 85
6.3 Materials ranking based on both thermal and mechanical properties 86
6.4 Materials optimization for both thermal and mechanical properties 87
APPENDIX 89
REFERENCES 95

List of Figures

Figure 1-1: Thermal decomposition of metal hydroxides [6] 2
Figure 1-2: Flame retardancy mechanism for metal hydroxides [6]. 3
Figure 1-3: Lead-free reflow soldering temperature profile [10] 4
Figure 1-4: Printed circuit board (PCB) laminate crack under ball grid array (BGA) [13] 5
Figure 2-1: Structure of laminate and role of each component [2] 6
Figure 2-2: Electroplating copper foil [14] 7
Figure 2-3: Cross-section of electrodeposited copper [14] 7
Figure 2-4: Plain weave [14] 8
Figure 2-5: (a) 1080 cloth; (b) 2116 cloth; (c) 7628 cloth. 9
Figure 2-6: Reaction to form difunctional epoxy [14] 9
Figure 2-7: Brominated difunctional epoxy resin [14] 9
Figure 2-8: DOPO chemical structure [6] 10
Figure 2-9: CTE as a function of volume loading for different fillers [15] 11
Figure 2-10: T-288 curves for the different laminates [16] 12
Figure 2-11: Correlation of Td vs T-288 [16] 13
Figure 2-12: Thermogravimetric analysis of different epoxy compounds [17] 13
Figure 2-13: Network formed in phenol aralkyl-type epoxy-resin compounds [17] 14
Figure 2-14: The TGA thermograms of CNE200/DOPO-PN-based epoxy resins under air [18] 15
Figure 2-15: The microsections show distortion of the base material and pad lifting with some resin voids [19] 16
Figure 2-16: IST coupon layout shows the electric current flow 16
Figure 2-17: Tensile strength of polypropylene as a function of the particle size and loading of fillers [11] 17
Figure 2-18: Typical tensile strength-concentration curves for filled polymers showing upper and lower bound responses [21] 18
Figure 2-19: Tensile strength vs. various silica filler content [21] 19
Figure 2-20: Modulus as a function of volume loading for different fillers [15] 20
Figure 3-1: Cross-section of a PWB 22
Figure 3-2 Mapping analysis of a cross-sectioned PWB using EDS 23
Figure 3-3: ImageJ analysis on fillers area percentage 25

Figure 3-4: Glass transition temperature calculated by DSC midpoint method [28] 26
Figure 3-5: Glass transition temperature measured by DSC 27
Figure 3-6: Glass transition measured by TMA method [29] 28
Figure 3-7: TMA curves obtained for measuring glass transition temperature 28
Figure 3-8: Tan delta vs. temperature from DMA curve [30] 29
Figure 3-9: Glass transition temperature measured by tan delta peak from DMA 30
Figure 3-10: CTE in z-axis measured by TMA before and after T_g 31
Figure 3-11: CTE in the x and y axis measured by TMA [31] 32
Figure 3-12: TMA curve indicates reversible event and delamination [32] 33
Figure 3-13: TMA curve indicates delamination at 288˚C 33
Figure 3-14: TGA curve for temperature to decomposition measurement 35
Figure 3-15: The derivative weight change with temperature curve from TGA 35
Figure 3-16: Typical daisy chain test coupon for IST test [34] 36
Figure 3-17: Resistance curve indicated a crack opening in the PTH barrel [34] 36
Figure 3-18: Schematic drawing of the three-point bending test [36] 38
Figure 3-19: Typical flexural strength measurement curve [37] 38
Figure 3-20: Load-extension curve obtained from the Instron tensile machine 39
Figure 3-21: Schematic drawing of the dual cantilever bending mode of DMA [38] 40
Figure 3-22: Storage modulus curves for different materials from DMA 41
Figure 3-23: Vickers indent on the epoxy 42
Figure 3-24: Load vs. peel distance obtained from the peel test [39] 43
Figure 4-1: Detection of bromine Lα and Kα peaks from the EDS analysis 45
Figure 4-2: Detection of aluminum from the aluminum hydroxide fillers from EDS 45
Figure 4-3: EDS mapping analysis for material A and material F 46
Figure 4-4: EDS mapping analysis for different types of fillers 46
Figure 4-5: SEM analysis demonstrates the different in shapes for different fillers 47
Figure 4-6: SEM cross-section failure analysis on delamination for each material 53
Figure 4-7: SEM analysis on crack opens in the copper barrel hole from Material D 56
Figure 4-8: SEM analysis on etched copper barrel hole with crack opens from Material D 56
Figure 4-9: Fracture surface for material A (without filler) and material E (with fillers) 58
Figure 4-10: Vickers indentation marks on different materials 60
Figure 5-1: Glass transition temperatures for each material 63

Figure 5-2: Correlation between z-axis CTE before T_g and total filler volume % 64
Figure 5-3: Correlation between z-axis CTE after T_g and total filler volume % 65
Figure 5-4: Correlation between z-axis CTE change and silica filler volume percentage. 66
Figure 5-5: Decomposition of alumnium hydroxide in Material D leads to an increase in CTE above 240˚C 67
Figure 5-6: Storage modulus cruves for different materials 68
Figure 5-7: Comparing between XY and Z axis CTE before T_g 69
Figure 5-8: Comparing between XY and Z axis CTE after T_g 69
Figure 5-9: Correlation between T_{260} and silica fillers volume % 70
Figure 5-10: Correlation between T288 and silica fillers volume % 71
Figure 5-11: Correlation between aluminum hydroxide and derivative weight change at 260˚C 73
Figure 5-12: Decomposition temperature at different weight loss (1, 2 and 5%) for each material 74
Figure 5-13: Correlation between T_{260} and T_d at 1 weight % loss 75
Figure 5-14: Knee cracks propagation in copper with and without etching 76
Figure 5-15: Correlation between IST performance and temperature to decomposition 77
Figure 5-16: Fracture surface analysis using SEM for materials with and without fillers 78
Figure 5-17: Flexural strength as a function of total filler loading 79
Figure 5-18: Flexural strength as a function of silica filler loading 79
Figure 5-19: Relationship between energy to fracture and silica fillers loading 80
Figure 5-20: Flexural modulus as a function of fillers loading in volume percentage 81
Figure 5-21: Relationship between filler loading and Vickers hardness 82
Figure 5-22: Copper peel strength of different materials 83

List of Tables

Table 1-1: Flame retardants substitutes 2
Table 2-1: Fiberglass compositions [14] 7
Table 2-2: Material properties of the resin and fillers [15] 11
Table 2-3: Thermal properties of cured epoxy with various phosphorus contents [18] 15
Table 2-4: Dependence of mechanical properties including toughness for composites with different fillers percentage [25] 20
Table 4-1: Fillers volume percentage for different materials 48
Table 4-2: Summary of different types of fillers and epoxy found in all materials 48
Table 4-3: Summary of glass transition temperatures measuring by different methods 49
Table 4-4: Z-axis CTE data for different materials 50
Table 4-5: X-Y-axis CTE data for different materials 51
Table 4-6: Time to delamination at 260˚C and 288˚C 52
Table 4-7: Temperature to decomposition in ˚C at different weight loss for each material 54
Table 4-8: Derivative weight changes at 260˚C for each material 55
Table 4-9: IST cycles to failure for each material 55
Table 4-10: Flexural strength data for each material 57
Table 4-11: Energy to fracture data for each material 58
Table 4-12: Flexural modulus measurements of each material from the DMA 59
Table 4-13: Vickers hardness for each material 59
Table 4-14: Copper peel strength for materials examined 60
Table 4-15: Dielectric constant and dissipation factors for each material 61
Table 5-1: Relationship between delamination modes and majority fillers 72
Table 6-1: Table summary of the thermal properties for all materials 85
Table 6-2: Table summary of the mechanical properties of all materials 86
Table 6-3: Table summary of the overall ranking for each material 87

Chapter 1
INTRODUCTION

Traditional laminates for printed wiring board (PWB) commonly contain brominated flame retardants, which form dioxins and furans from incineration and can be hazardous to the environment [1]. This becomes a concern for computer manufactures and they have committed to provide more environmentally friendly products with minimal concentration of brominated compounds. Flame retardant substitutes, including metal hydroxides fillers and phosphorous-doped epoxy, are used for the bromine-free (halogen-free) products in order to meet the flammability requirement [2]. However, the impact of the flame retardants for halogen-free laminates to manufacturing and performance of handheld electronics require comprehensive examination and evaluation.

1.1 Driving force for halogen-free

Since the RoHS (restriction of the use of hazardous substances) legislation has been put in place by the European Union (EU), electronic manufacturers are required to eliminate lead, mercury, cadmium, chromium VI, polybrominated biphenyls and polybrominated biphenyl ethers with the latter two used as flame retardants in finished product for the EU market place. Recently, the driving force for halogen-free electronic materials is coming from the computer manufacturers who have committed to offer bromine and chlorine free products. The main concerns about traditional halogenated laminates are the release of highly toxic and corrosive products during combustion [3, 4]

1.2 Traditional FR-4 laminates

Traditional FR-4 laminates are the most commonly used laminates for electronics. FR-4 consists of woven fiberglass and brominated epoxy resin. It has good thermal, mechanical and electrical performance compared to other traditional laminates. The glass transition temperature (T_g) varies from 125 to 135 ºC and it can be improved up to 180ºC depending upon the applications. The chemical resistance can be improved by blending the difunctional epoxy with polyfunctional epoxy resin or using polyfunctional epoxy resin. Difunctional epoxy has two epoxides functional groups while polyfunctional has more than two epoxides to react with the curing agents [5].

1.3 Flame retardants substitutes

Several international organizations have defined halogen-free as bromine- and chlorine-free, and have set different maximum allowable concentrations in the product. For example, the IEC 61249-2-21

(International Electrotechnical Commission) and the IPC suggested that the maximum allowable concentration of bromine or chlorine is 900 ppm but the total concentration of both elements cannot exceed 1500 ppm. The JPCA ES-01 (Japan Printed Circuit Association) defines halogen-free as a maximum concentration of 900 ppm for bromine or chlorine.

If legislation is forthcoming, the brominated epoxy used in the present laminates would have to be replaced. The most common flame retardant substitutes in halogen-free laminates are metal hydroxide fillers such as aluminum and magnesium hydroxides, and phosphorus-doped epoxy, which are summarized in Table 1-1.

Table 1-1: Flame retardants substitutes

Method	Mechanism
$Mg(OH)_2$	Release of water
$Al(OH)_3$	Release of water
Phosphorus doped epoxy	Char formation

The metal hydroxides release water vapor to cool the laminate in the presence of an ignition source [6]. The thermal decomposition of the metal hydroxides into metal oxide and water vapor are shown in Figure 1-1, while the schematic of the flame retardancy mechanism is shown in Figure 1-2.

$$2\ Al(OH)_3 + 1075\ kJ/kg \rightarrow Al_2O_3 + 3H_2O$$

$$Mg(OH)_2 + 1220\ kJ/kg \rightarrow MgO + H_2O$$

Figure 1-1: Thermal decomposition of metal hydroxides [6]

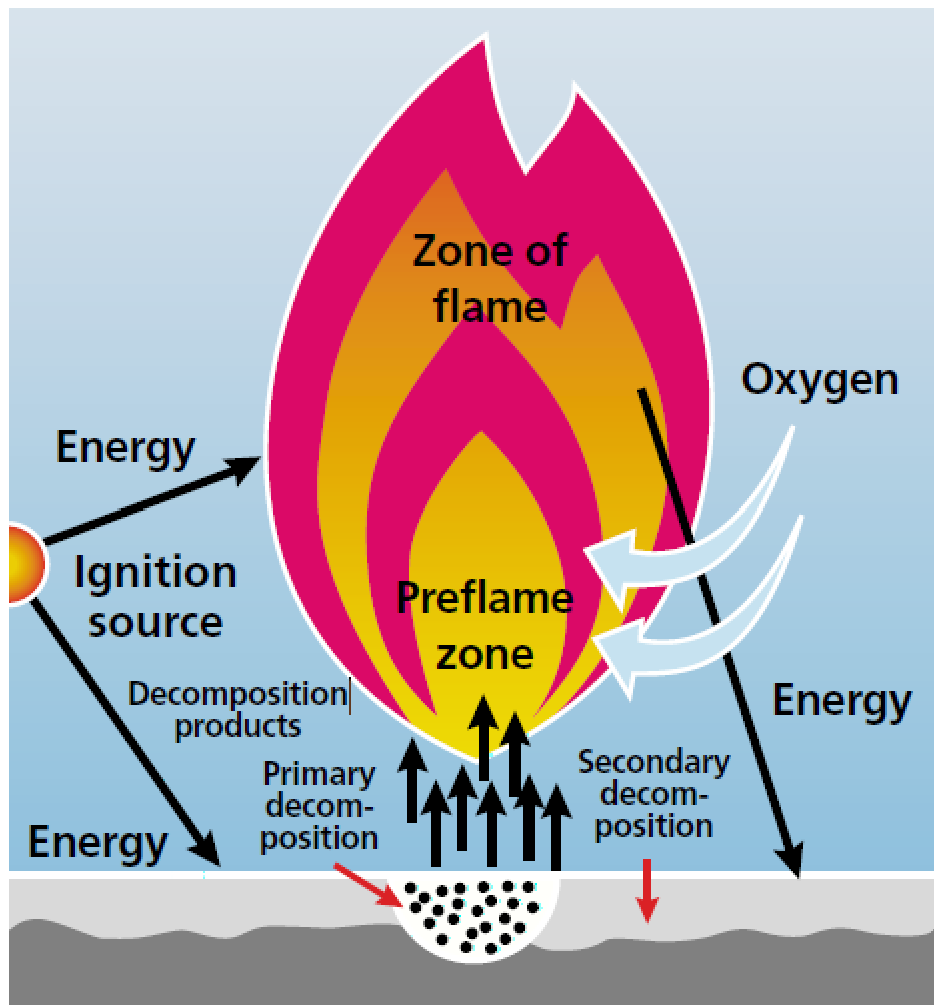

Figure 1-2: Flame retardancy mechanism for metal hydroxides [6].

In addition, phosphorus-doped epoxy suppresses the flame by causing the polymer to char, which forms an insulation layer between the polymer substrate and the zone of flame [7].

1.4 Handheld Electronics

Handheld devices such as mobile phones and PDAs are constrained by the device size, weight, power consumption, reliability and cost [8]. Also, handheld devices are frequently dropped and there are many studies on drop performance using finite element analysis (FEA) [9]. All these factors affect the requirements for laminates. For example, the laminates have to survive numerous drops before permanent damage, which requirement needs to be achieved with reasonable size and cost.

1.5 Objective

The purpose of this study is to examine the thermal and mechanical properties of various halogen-free laminates used in handheld electronic products and to correlate these properties with the manufacturing and performance requirements.

1.5.1 Manufacturing based parameters

Handheld electronics manufacturing involves surface mount assembly and rework processes where the laminates are exposed to multiple heat cycles. The surface mount assembly requires two reflow soldering cycles for double-sided PWB, while rework processes can be up to 10 reflow cycles. Also, the temperature for lead-free reflow soldering is above 245 ˚C as shown in Figure 1-3.

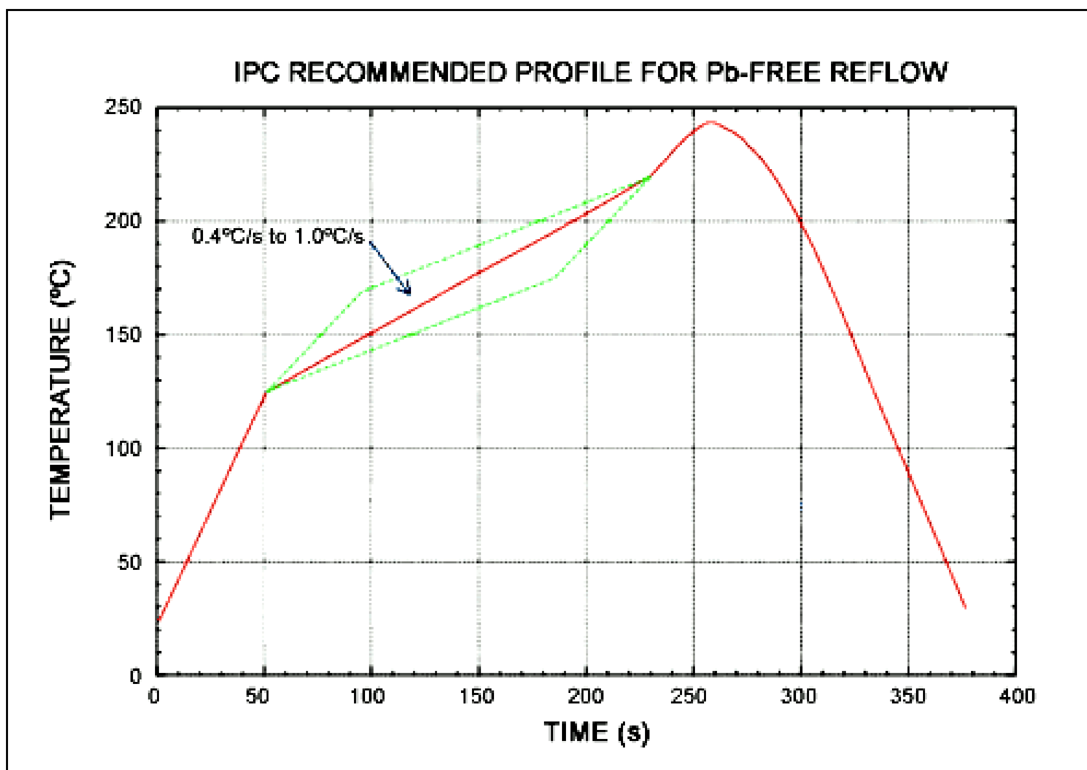

Figure 1-3: Lead-free reflow soldering temperature profile [10]

Therefore, the thermal properties of the laminates are important to manufacturing in that the laminates have to withstand multiple heat cycles. For example, the glass transition temperature (T_g) property, where the polymer changes from rigid to rubbery state, affects the product dimensional stability during soldering. Thermal properties such as coefficient of thermal expansion (CTE) relate to plated thru hole (PTH) and copper pad plastic deformation during reflow soldering. Time to delamination

measures the tendency to delamination, while temperature to decomposition contributes to long-term reliability of the product after assembly and rework. Interconnect stress test (IST) correlates to crack opening in PTH, and copper interlayer induced cracking by thermal cycles during reflow. All of these thermal properties have a significant impact on the manufacturing processes and hence the quality of the final product.

1.5.2 Performance based parameters

Handheld devices frequently experience mechanical stresses from drop and impact. This can lead to device malfunction depending on the stress level and also the mechanical properties of the base materials. Different studies [11, 12] demonstrate that stiff composite materials have low impact strength, which can cause mechanical damage to the PCB during assembly and/or usage, especially for handheld device. The toughness of the laminates relates to the brittleness and susceptibility to laminate cracks such as pad cratering that is shown as Figure 1-4 [13].

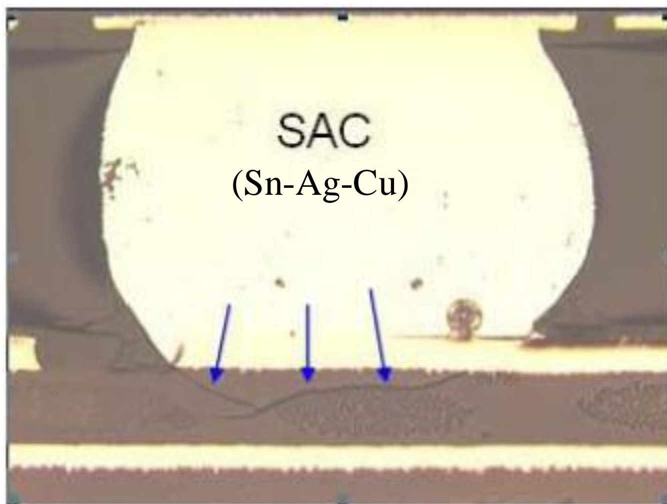

Figure 1-4: Printed circuit board (PCB) laminate crack under ball grid array (BGA) [13]

Other mechanical properties such as flexural strength and Vickers hardness determine the resistance to plastic deformation that can permanently damage the laminates composite. Therefore, the mechanical properties of the laminates correlate to the performance and reliability of the handheld device.

Chapter 2

LITERATURE REVIEW

2.1 Role of each component in laminates

Laminates for printed wiring boards (PWB) are composed of four different components: copper foil, glass fibers reinforcement, resin matrix and filler system. The functions for each component are demonstrated in Figure 2-1.

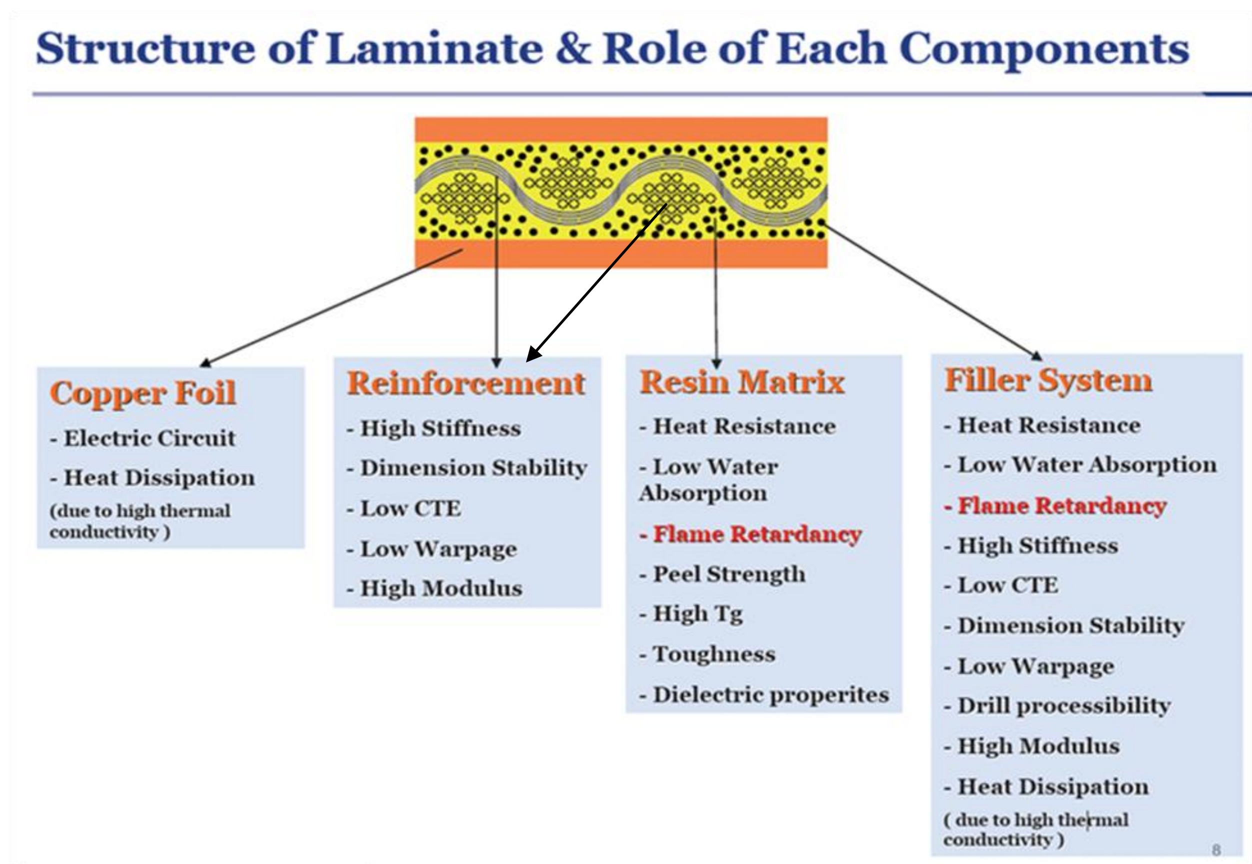

Figure 2-1: Structure of laminate and role of each component [2]

Copper foil is used as the conductive material and is commonly produced by electrodeposition [14]. Copper is first dissolved into a sulfuric acid bath and purified into copper sulfate sulfuric acid solution. The copper sulfate is then electrodeposited onto a stainless steel or titanium drum, which is demonstrated at Figure 2-2.

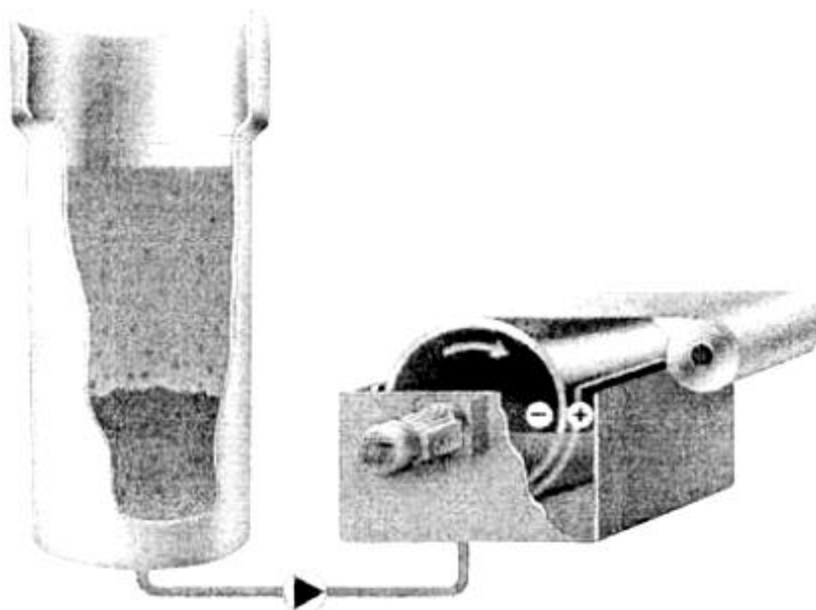

Figure 2-2: Electroplating copper foil [14]

This process creates two different sides of copper foil: smooth and shiny foil on the drum side and coarser matte on the opposite side as shown in Figure 2-3. This indeed has a significant impact on the delamination behavior, which will be further discussed.

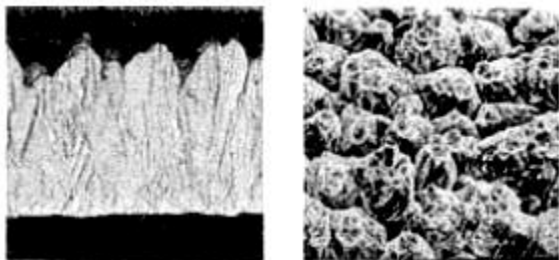

Figure 2-3: Cross-section of electrodeposited copper [14]

Glass fibers are used as reinforcement to provide the required stiffness and dimension stability. Since glass fibers used for PWB application are E-glass, they contain a mixture of different oxides as shown in Table 2-1. E-glass provides the requirement for PWB electrical, mechanical, and chemical properties. The glass fibers have a plain-weave pattern which consists of the warp yarn and fill yarn interlocked in an alternate fashion as demonstrate in Figure 2-4.

Table 2-1: Fiberglass compositions [14]

Component	E-glass	S-glass	D-glass	Quartz
Silicone dioxide	52–56%	64–66%	72–75%	99.97%
Calcium oxide	16–25%	0–0.3%	0–1%	
Aluminum oxide	12–16%	24–26%	0–1%	
Boron oxide	5–10%		21–24%	
Sodium oxide and potassium oxide	0–2%	0–0.3%	0–4%	
Magnesium oxide	0–5%	9–11%		
Iron oxide	0.05–0.4%	0–0.3%	0.3%	
Titanium oxide	0–0.8%			
Fluorides	0–1.0%			

The warp yarn lies in the lengthwise (machine) direction of the fabric while the fill yarn is in the crosswise direction of the fabric.

Figure 2-4: Plain weave [14]

Depending on the glass cloth styles, the diameter and the volume percentage of the glass fibers in the matrix can be varied. As shown in Figure 2-5, 1080 cloth has a lower packing ratio and hence smaller volume percentage in the laminates. The volume percentage of the glass fibers influences both the thermal and mechanical properties.

The traditional epoxy resin is a dielectric material with flame retardancy. The traditional epoxy is manufactured by reaction of epichlorohydrin with bisphenol A forming difunctional epoxy. Bromination of the bisphenol A can provide the flame retardancy which results in a brominated difunctional epoxy resin as shown in Figure 2-6 and Figure 2-7.

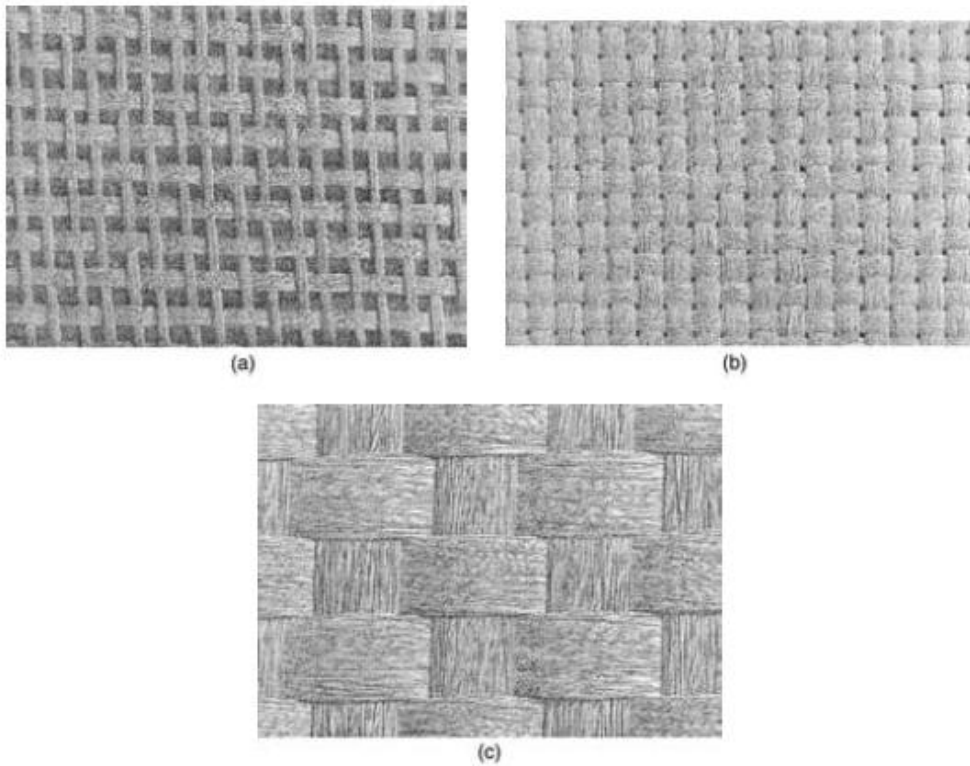

Figure 2-5: (a) 1080 cloth; (b) 2116 cloth; (c) 7628 cloth.

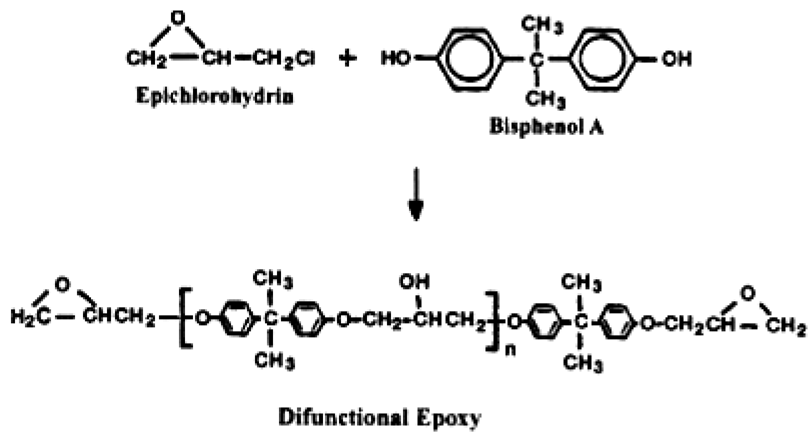

Figure 2-6: Reaction to form difunctional epoxy [14]

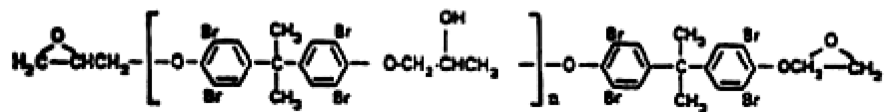

Figure 2-7: Brominated difunctional epoxy resin [14]

Halogen-free epoxy replaces the brominated epoxy with phosphorous doped epoxy. DOPO (Dihydrooxaphosphaphenantrene) is commonly used in halogen-free epoxy for flame retardant replacement [6]. The phosphorus content is around 1.6% in the resin and it satisfies the UL 94 V0 flammability test, which is a requirement for electronic devices. The chemical structure of DOPO is given in Figure 2-8.

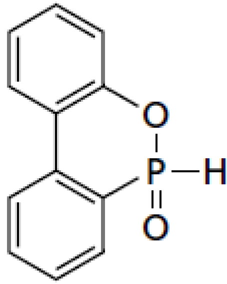

Figure 2-8: DOPO chemical structure [6]

There are different types of fillers embedded in the epoxy and each of them has a different purpose. For example, silica fillers are added to lower CTE while metal hydroxides fillers are flame retardants. This will be further discussed in the results section.

2.2 Effects of fillers and epoxy on thermal properties of composites

The addition of fillers to polymer composites for electronic packaging lowers the CTE based on the simple rule of mixtures. The chemistry of the epoxy affects the delamination as well as the decomposition properties.

2.2.1 Coefficient of Thermal Expansion

Silica is used to lower the CTE because of its ultra low CTE compared to epoxy and other fillers [15]. The CTE for silica is 0.5 ppm/˚C while that of epoxy is 88 ppm/˚C before T_g. Substituting these numbers into the equation given at Equation 2-1 shows that increasing the silica volume fraction further lowers the overall CTE for the composites.

$$\alpha_c = \alpha_f V_f + \alpha_m(1-V_f)$$

Equation 2-1: First-order approximation to composite CTE [15]

α_c is the CTE of the composite, α_m and α_f are the CTE of the matrix and the fillers respectively, and V_f is the volume fraction of the fillers. Therefore, the types of fillers influence the composite CTE.

Fillers such as silica are more effective in lowering CTE compared to alumina and the data is given at Table 2-2. Also, SCAN, silica-coated aluminum nitride filler, is listed in the table.

Table 2-2: Material properties of the resin and fillers [15]

Material	Epoxy	Silica	SCAN	Alumina
Thermal conductivity (W/mK)	0.195	1.5	220	36
CTE (PPM/°C)	88	0.5	4.4	6.6
Young's modulus (GPa)	2.25	73	330	385
Poisson's ratio	0.19	0.19	0.25	0.24
Shear modulus (GPa)	0.8	31	132	155
Bulk modulus (GPa)	3.75	39	220	247
Density (g/cc)	1.1	2.2	3.26	3.98

Results validate the rule-of-mixtures equation that silica-filled epoxy composites always have a lower CTE than other fillers at the same given filler loading. The order of increasing CTEs for each sample is given as the following: silica<SCAN<Alumina and that follows the same trend as the intrinsic fillers CTE, which is shown in Figure 2-9. The CTE trend line exhibits essentially a linear relationship with fillers volume percentage, which further verifies the rule-of-mixtures equation.

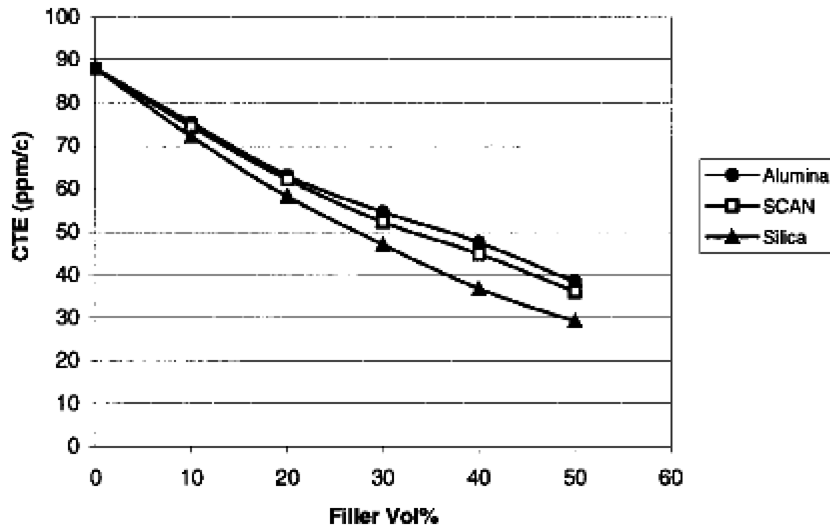

Figure 2-9: CTE as a function of volume loading for different fillers [15]

2.2.2 Delamination

Delamination measures the resistance to thermally induced failure, indicated by the separation of layers. One of the causes for delamination is the decomposition of epoxy and/or fillers into gaseous products, which induces internal pressure that is high enough to crack the matrix [16]. The time to delamination is measured according to IPC standards that indicate testing temperatures at 260, 288 or 300˚C. It defines the time to delaminate for the sample at the test temperature. The T-288 test results show that traditional FR-4 fails earliest compared to other epoxy resins with higher T_g or which are filled (See Figure 2-10). This indicates that the glass transition temperature for the epoxy and/or the addition of fillers affect the time to delamination.

The results also show that the higher the decomposition temperature, the longer the time to delamination at 288˚C. The temperature to decomposition measures the temperature at which the sample has a 1, 2 or 5 weight % loss. If the epoxy resin system has a higher decomposition temperature, it is more resistant to decomposition and hence releases smaller amount of gas. Therefore, the internal pressure exerted on the matrix is not as much as the resin system exhibiting a lower decomposition temperature. The experimental data is given at Figure 2-11.

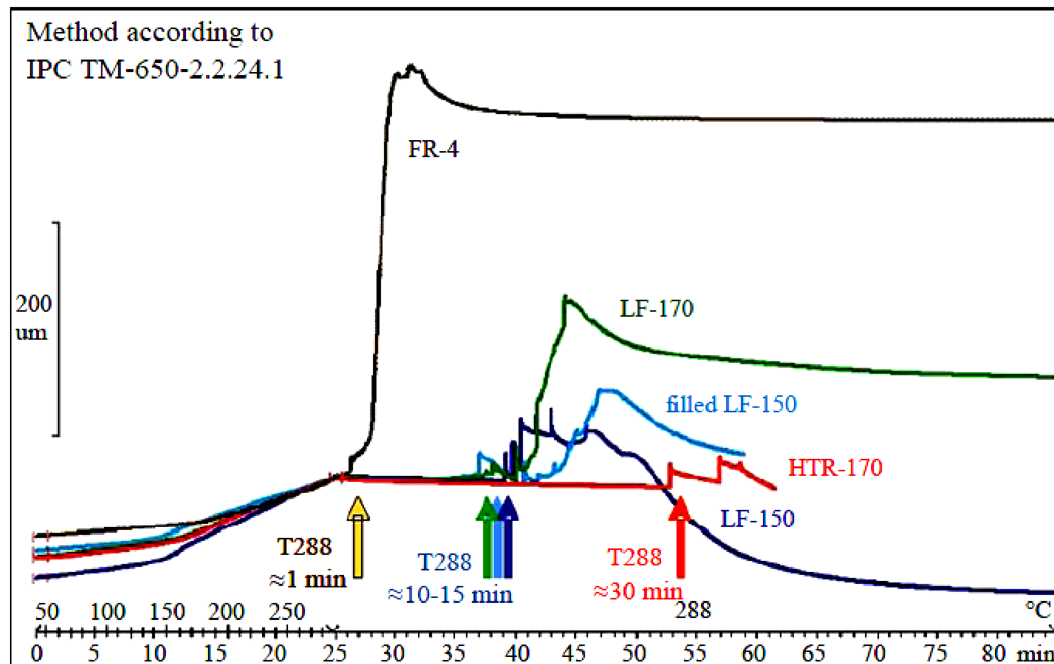

Figure 2-10: T-288 curves for the different laminates [16]

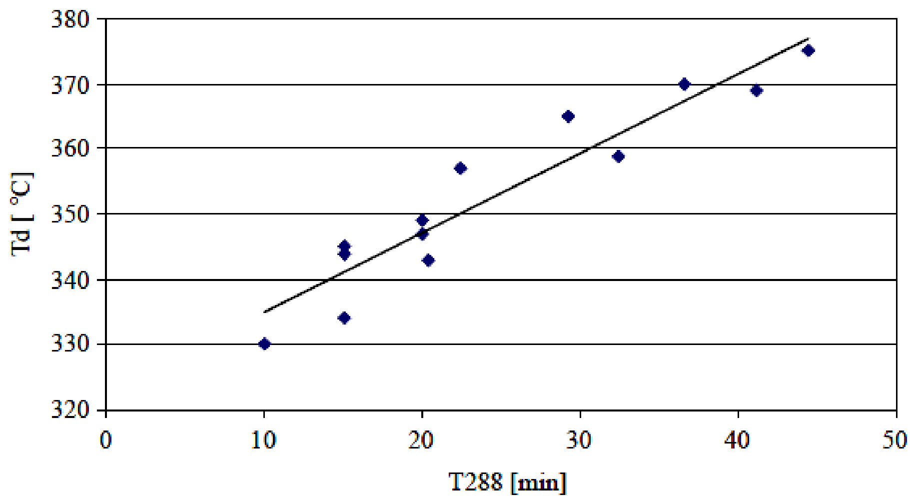

Figure 2-11: Correlation of Td vs T-288 [16]

2.2.3 Decomposition

The temperature to decomposition relates to the thermal degradation resistance of the epoxy system and it is measured by the weight loss percentage at a specified temperature. High thermal stability is important for advanced electronic packaging so that the epoxy is able to survive lead-free soldering temperature. Iji [17] shows that phenol-type epoxy exhibits a higher temperature to decomposition than conventional epoxy as shown in Figure 2-12.

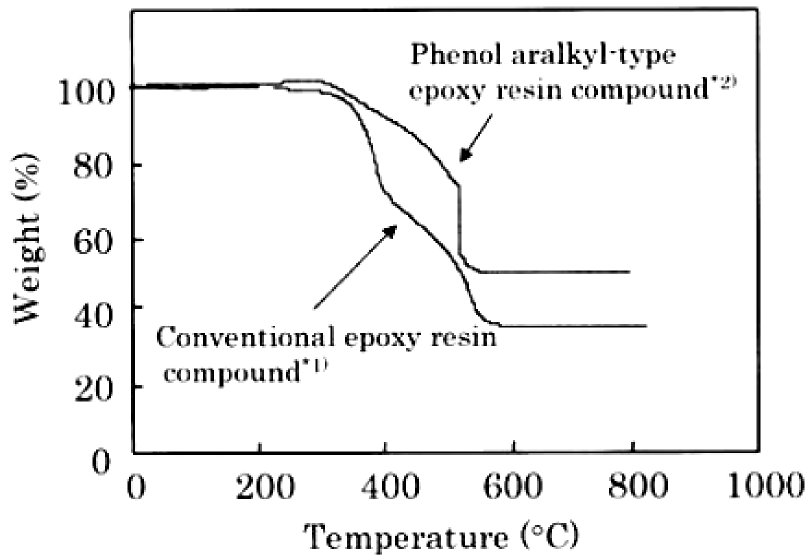

Figure 2-12: Thermogravimetric analysis of different epoxy compounds [17]

During ignition, the phenol-type epoxy containing significant amounts of aromatic groups generate a stable foam layer consisting of resin compound, carbon oxides and hydrocarbons. This layer suppresses the transfer of heat to the bulk resin and enhances the thermal stability [17]. The network of the phenol containing epoxy backbone is shown in Figure 2-13. Liu [18] demonstrates that phosphorus doped epoxy (DOPO) has a slower decomposition rates than phosphorus-free resins above 350ºC. The resistance to degradation for DOPO is because the phosphorus groups decompose to phosphorus-rich residue forming a thermally stable layer upon heating. The result given in Figure 2-14 shows that the higher the phosphorus contents the more resistance to decomposition is observed. The phosphorus content percentage for each epoxy system is given at Table 2-3.

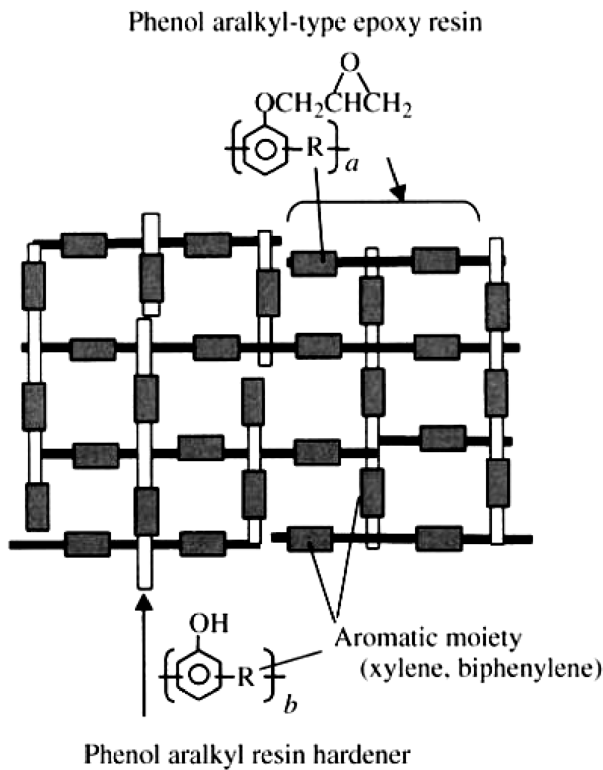

Figure 2-13: Network formed in phenol aralkyl-type epoxy-resin compounds [17]

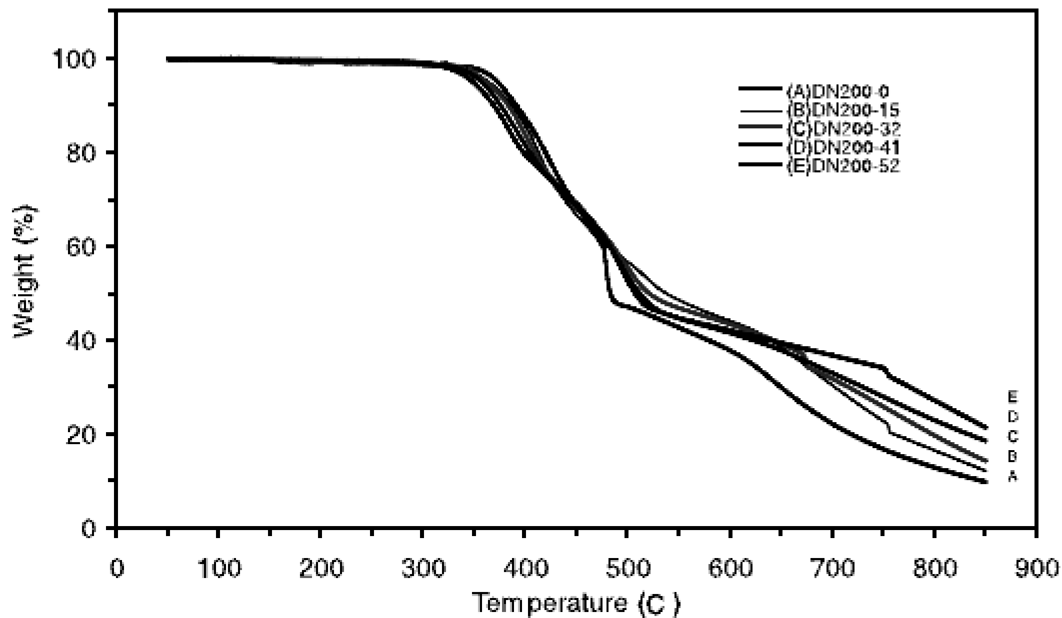

Figure 2-14: The TGA thermograms of CNE200/DOPO-PN-based epoxy resins under air [18]

Table 2-3: Thermal properties of cured epoxy with various phosphorus contents [18]

Epoxy resins	P content (wt%)
DN200-0	0
DN200-15	1.45
DN200-32	3.11
DN200-41	3.99
DN200-52	5.05

2.2.4 Interconnect stress test (IST)

IST measures the high temperature effect on plated through hole (PTH) and inner-layer-bonding integrity during soldering. Lamprecht [19] shows that the major factors in the reliability of the PTH and copper inner-layer are the following: base material CTE, panel thickness, through hole diameter, and electroplated copper thickness. It is found that the CTE effect is significant and causes pad lifting and resin voiding as shown in Figure 2-15. As a result, it can influence the reliability of the copper circuitry within the PWB.

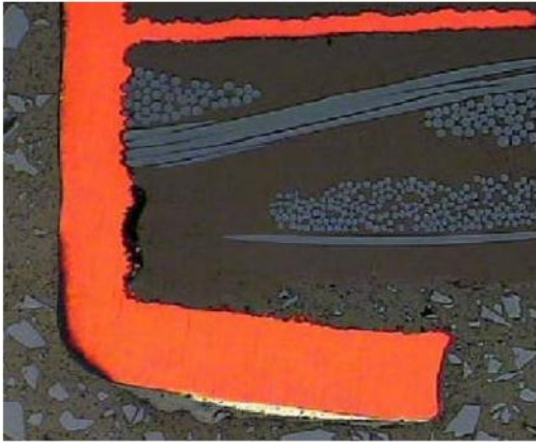

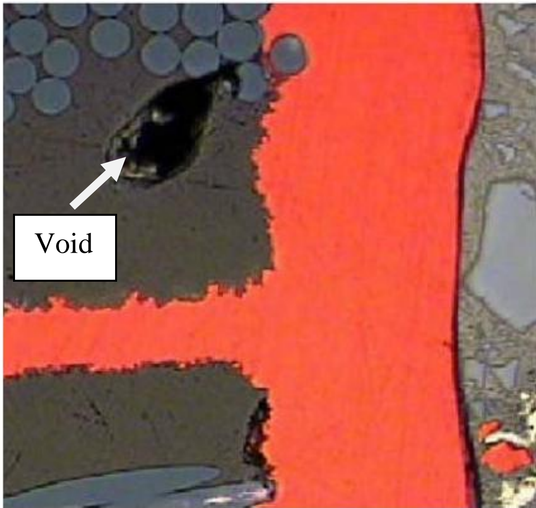

Figure 2-15: The microsections show distortion of the base material and pad lifting with some resin voids [19]

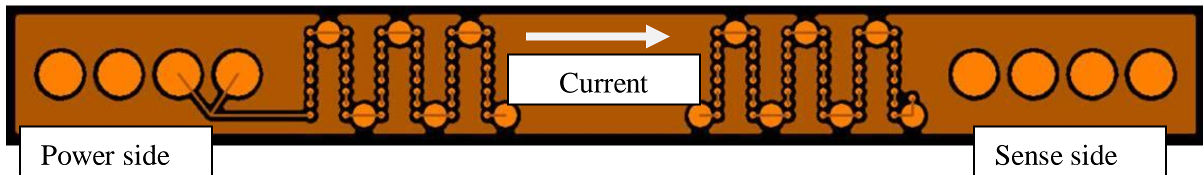

Figure 2-16: IST coupon layout shows the electric current flow

Figure 2-16 demonstrates the current flows from the power side through the copper inner layers and plated through holes, and exits at the sense side of the IST coupon. As the current passes through, the copper barrel holes in the centre of the coupon heats up and the resistance of the copper is monitored.

2.3 Effects of fillers on mechanical properties of composites

Adding fillers into composites increases the modulus of elasticity and hence the stiffness is enhanced. However, depending on the types of fillers and filler loading, the tensile strength can be reduced such that the composites become more susceptible to mechanical damage. Thus, the toughness properties are important to drop test resistance.

2.3.1 Tensile strength

The tensile properties of filled composites correspond to the bonding of the fillers in the polymer matrix. If the fillers are well bonded to the matrix, the tensile strength is effectively unchanged. However, if the fillers are not bonded to the polymer and not able to carry load, the tensile strength will be decreased linearly with fillers loading [11]. This is demonstrated at Figure 2-17.

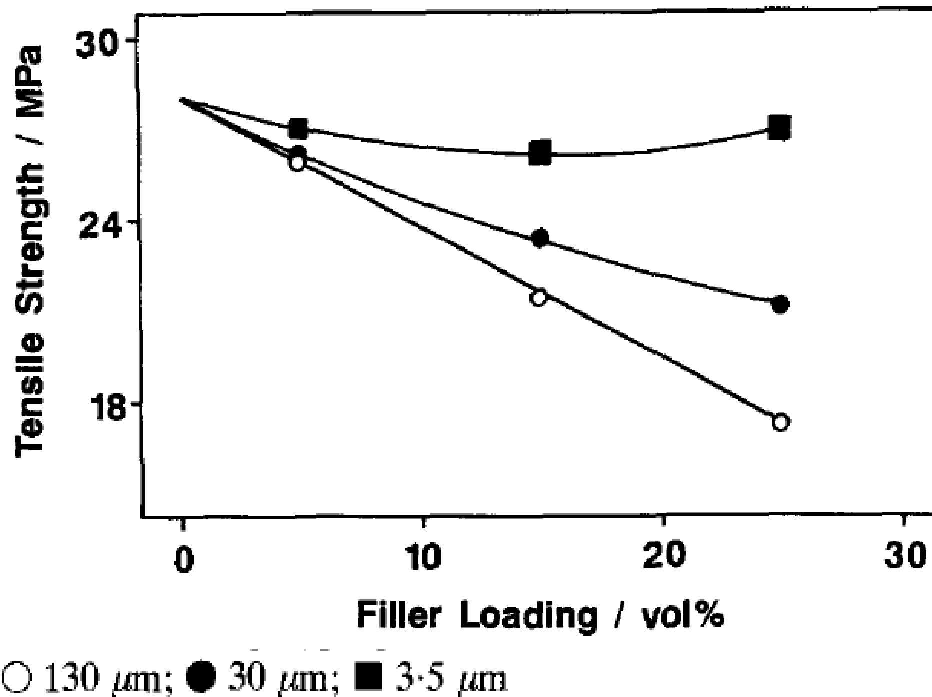

Figure 2-17: Tensile strength of polypropylene as a function of the particle size and loading of fillers [11]

For electronic application, the PWB has fillers in the size of 3-5 μm. As the 3-5 μm fillers loading is at 25 volume %, the tensile strength remains high. Vollenberg [20] explains that smaller fillers act as blocking area and dissipates the stress during deformation. However, larger fillers are not able to carry the load and hence the tensile strength is decreased linearly with the filler loadings. Chen [21]

also demonstrates similar results that the tensile strength is strongly depended on the polymer-fillers interactions and as shown in Figure 2-18.

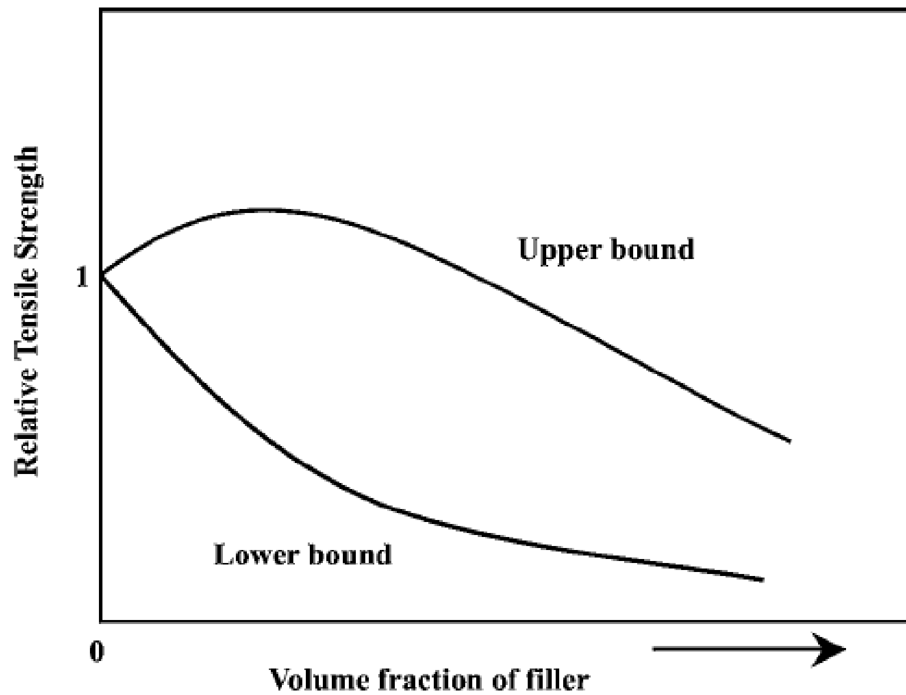

Figure 2-18: Typical tensile strength-concentration curves for filled polymers showing upper and lower bound responses [21]

The upper bound curve corresponds to fillers having a strong adhesion to the polymer matrix while the lower bound is for fillers having weak adhesion. The study also shows that polymer composites filled with silica exhibit the lower bound relationship, which indicates weak interaction between the silica-polymer as shown in Figure 2-19. Also, the tensile strength decreases with increasing silica filler, which is commonly observed in filled composites [22, 23, 24]. The result also reveals that small-size silica filled substrate possesses a lower tensile strength than large-size filler. Since silica filler is highly hygroscopic, small-size silica filler has greater surface area and higher moisture absorption, which leads to a lower tensile strength [21].

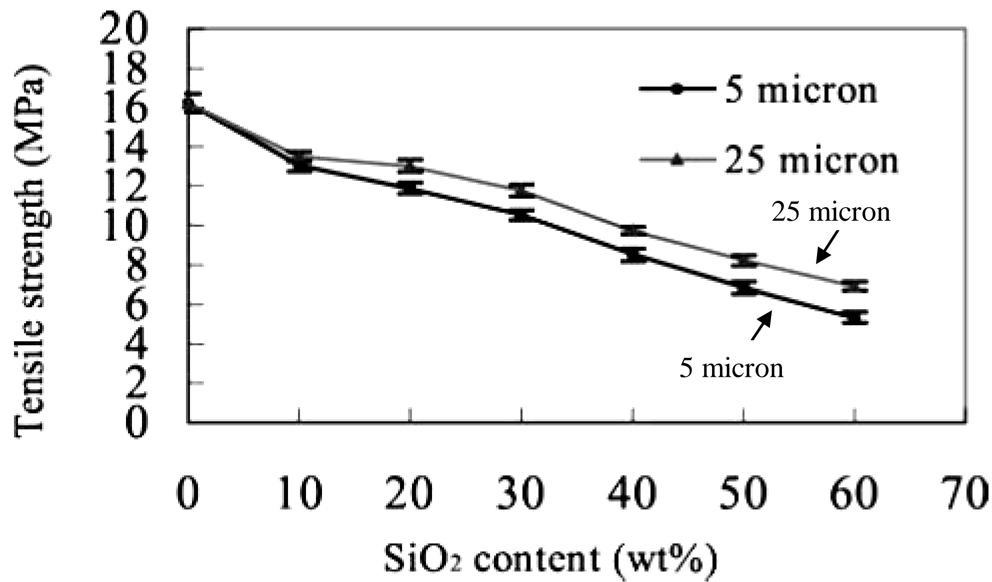

Figure 2-19: Tensile strength vs. various silica filler content [21]

2.3.2 Modulus of elasticity

The elastic modulus of a two-phase composite is often described by the Voight model, which assumes both phases in the composite are subjected to the same strain [15]. The equation is given at Equation 2-1 where E_c, E_p, and E_m are, the Young's modulus of the composite, particle (filler), and the matrix respectively, and Φ is the filler's volume fraction.

$$E_c = E_p\phi + E_m(1 - \phi)$$

Equation 2-2: Voigt model of two-phase composite [15]

The modulus of elasticity in this study is determined using a dynamic mechanical analyzer (DMA) with a 1-Hz frequency strain [15]. The storage modulus is found to be increased with the filler volume percentage in a linear fashion, which is given at Figure 2-20. It is found that the SCAN filled epoxy has the highest modulus, which may be due to better adhesion between the filler and matrix.

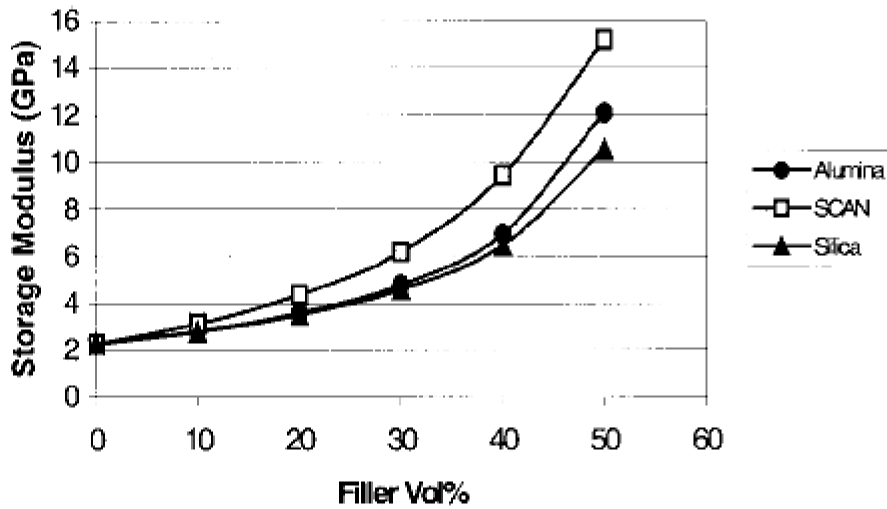

Figure 2-20: Modulus as a function of volume loading for different fillers [15]

2.3.3 Toughness

Toughness is important to the impact resistance of the laminates. Adding fillers increases the stiffness, but the laminates will also become more brittle and hence this lowers toughness. Marcovich [25] measures the change in toughness against filler percentage for filled polyester/styrene thermoset composites. The results show that the toughness is reduced significantly as filler weight percentage increases as shown in Table 2-4.

Table 2-4: Dependence of mechanical properties including toughness for composites with different fillers percentage [25]

Filler wt%	E (Gpa)	σ_Y (MPa)	r_{ul}	Toughness
40	3.3 ± 0.4	128.3 ± 4.8	0.199 ± 0.050	22.0 ± 6.5
50	3.3 ± 0.2	169.7 ± 0.8	0.122 ± 0.018	18.8 ± 1.4
60	3.9 ± 0.4	172.8 ± 8.2	0.137 ± 0.011	14.3 ± 6.7
65	4.5 ± 0.2	156.2 ± 3.0	0.081 ± 0.005	8.9 ± 0.5
70	4.1 ± 0.4	128.1 ± 3.2	0.065 ± 0.007	5.2 ± 0.3
75	3.0 ± 0.7	63.9 ± 12.3	0.035 ± 0.004	1.1 ± 0.1

2.4 Summary

The filler's properties and epoxy chemistry of polymeric composite materials directly affect both the thermal and mechanical properties. Increasing the filler percentage lowers the CTE and results in better IST performance. The epoxy chemistry also plays an important role that thermally stable epoxy system has a higher resistance to decomposition and delamination. However, highly filled composites with increased stiffness have poor tensile strength and toughness properties. As a result, addition of fillers weakens the mechanical performance of the composites.

Chapter 3

Experimental Method

3.1 Fillers and epoxy characterization

A sample with a dimension of 15mm x 15mm x 1.0 mm was cut from each material. It was then mounted with Struers SpeciFix Resin and SpeciFix-40 Curing Agent, which was thermally cured for 2 hours at 40°C. The sample was cross-sectioned using standard metallographic methods for grinding and polishing.

3.1.1 SEM and Mapping Analysis

After the sample was cross-sectioned properly, the surface of the sample was analyzed using a SEM (Scanning Electron Microscopy) model JEOL JSM-6460LV. The features within the PWB materials could be identified and shown in Figure 3-1.

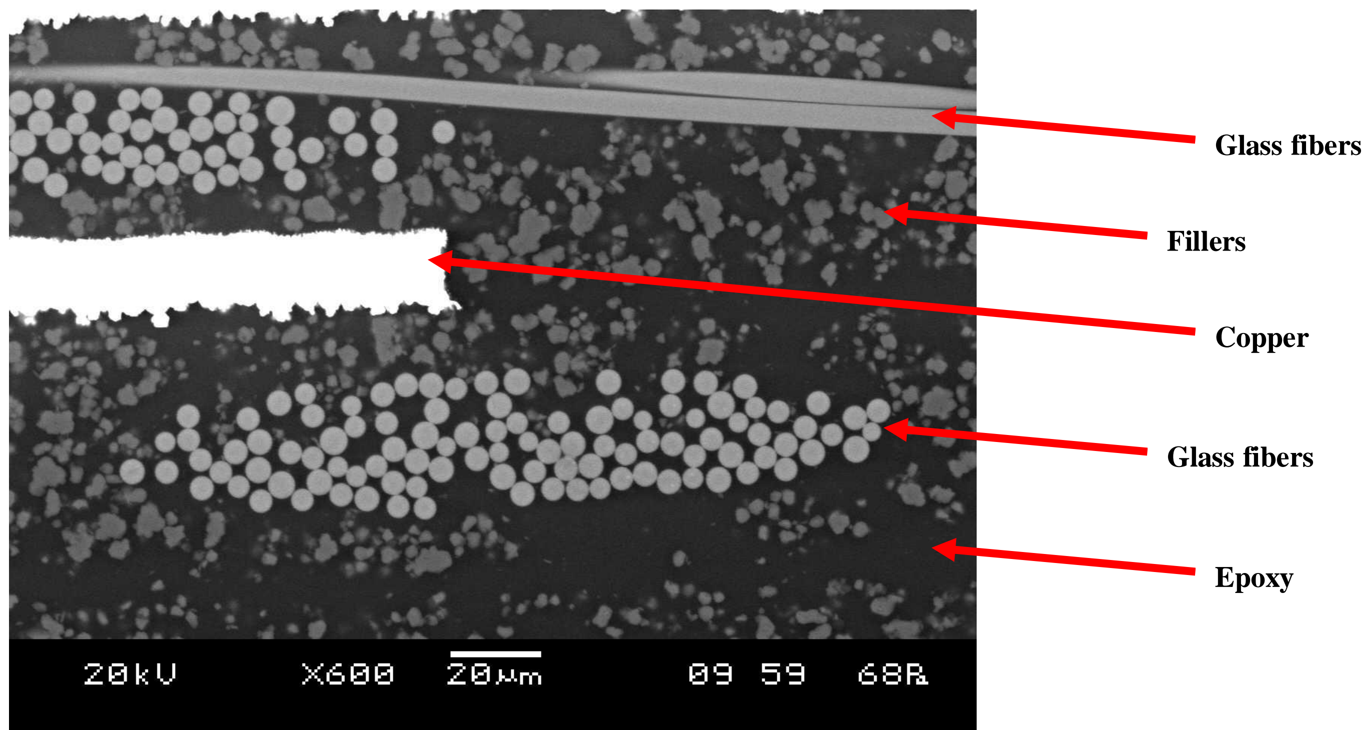

Figure 3-1: Cross-section of a PWB

The warp yarn and the fill yarn of the glass fibers were observed in the SEM as the parallel and perpendicular directions to the page. In order to characterize the chemical composition of each feature, mapping analysis by EDS (Energy Dispersive X-ray Spectroscopy) was performed. A sample of a mapping analysis is given at Figure 3-2.

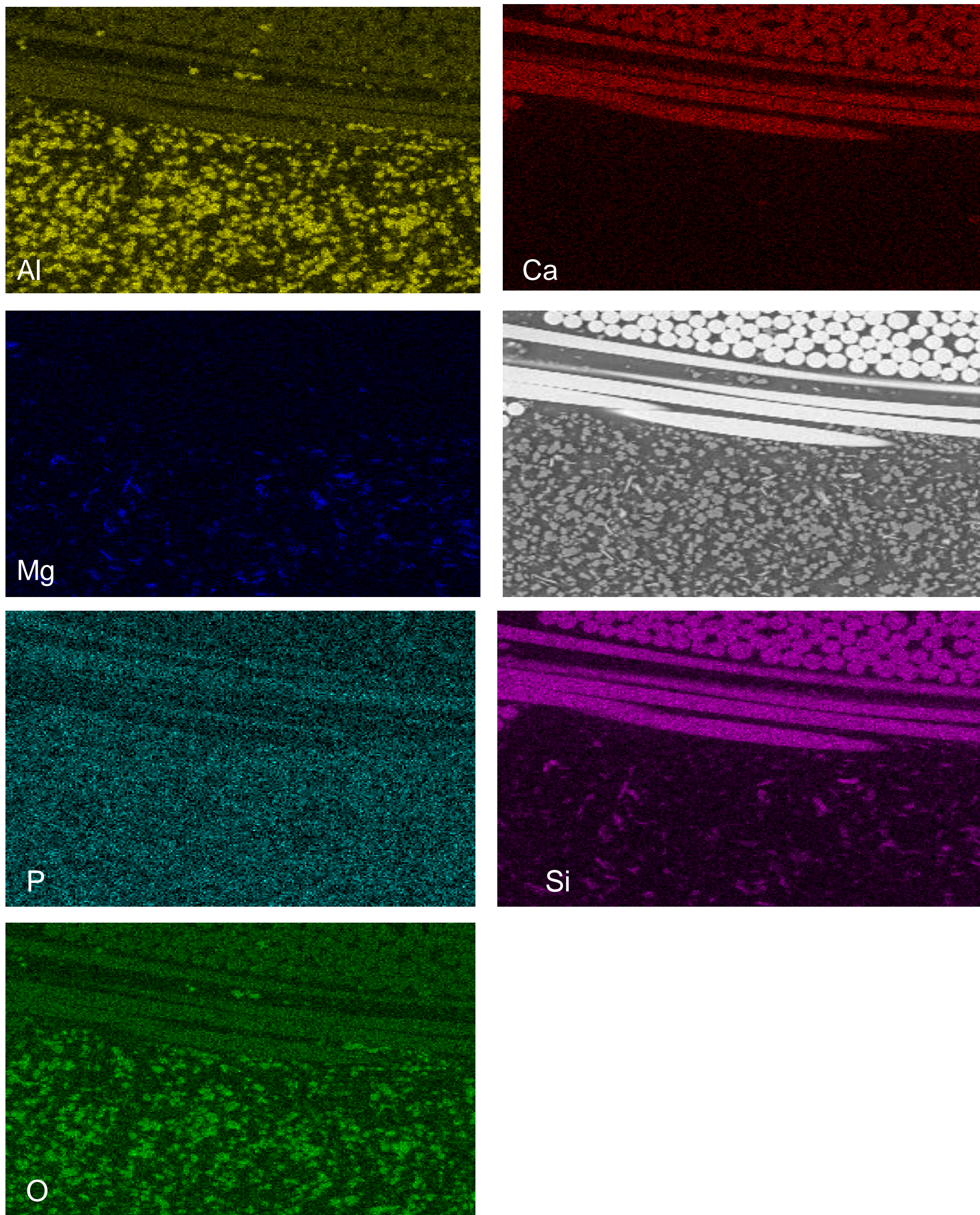

Figure 3-2 Mapping analysis of a cross-sectioned PWB using EDS

From the mapping analysis, the types of epoxy could be identified with the presence of bromine or phosphorous compound in the epoxy backbone, which determined whether the PWB was halogen-free or halogenated. Silicon, aluminum, calcium, oxygen signals were found in the glass fibers, coming from the different oxides of the E-glass fibers. In addition, aluminum and magnesium from the fillers verifies the presence of the metal hydroxides used as flame retardants.

3.1.2 Image Analysis

ImageJ 1.40g software was used to estimate the area percentage of the fillers presented in the epoxy. Also, it was assumed that the fillers were uniformly distributed among the epoxy and hence the area percentage should be equivalent to the volume percentage, which will be used in this study. An example of the ImageJ measurements is given at Figure 3-3. Images from the SEM were imported into the ImageJ and changed into a suitable format. The threshold could be adjusted automatically by the program based on the brightness and contrast of the features presented in the image. The SEM would also pick up signals from the fillers underneath the surface and could lead to an overestimation of the volume percentage of the fillers. In this case, the ImageJ software could adjust the threshold to compensate and only select the fillers on the top surface for volume percentage estimation. The same processes were performed on the images imported from the mapping analysis in order to estimate the volume percentage for specific fillers.

The filler's volume percentage estimation was based on seven different locations on the PWB cross-sections. It was found that most materials exhibit similar fillers percentage at different locations within a range of ±3%. Therefore, it was assumed that the estimation should reflect the overall fillers volume percentage of the PWB.

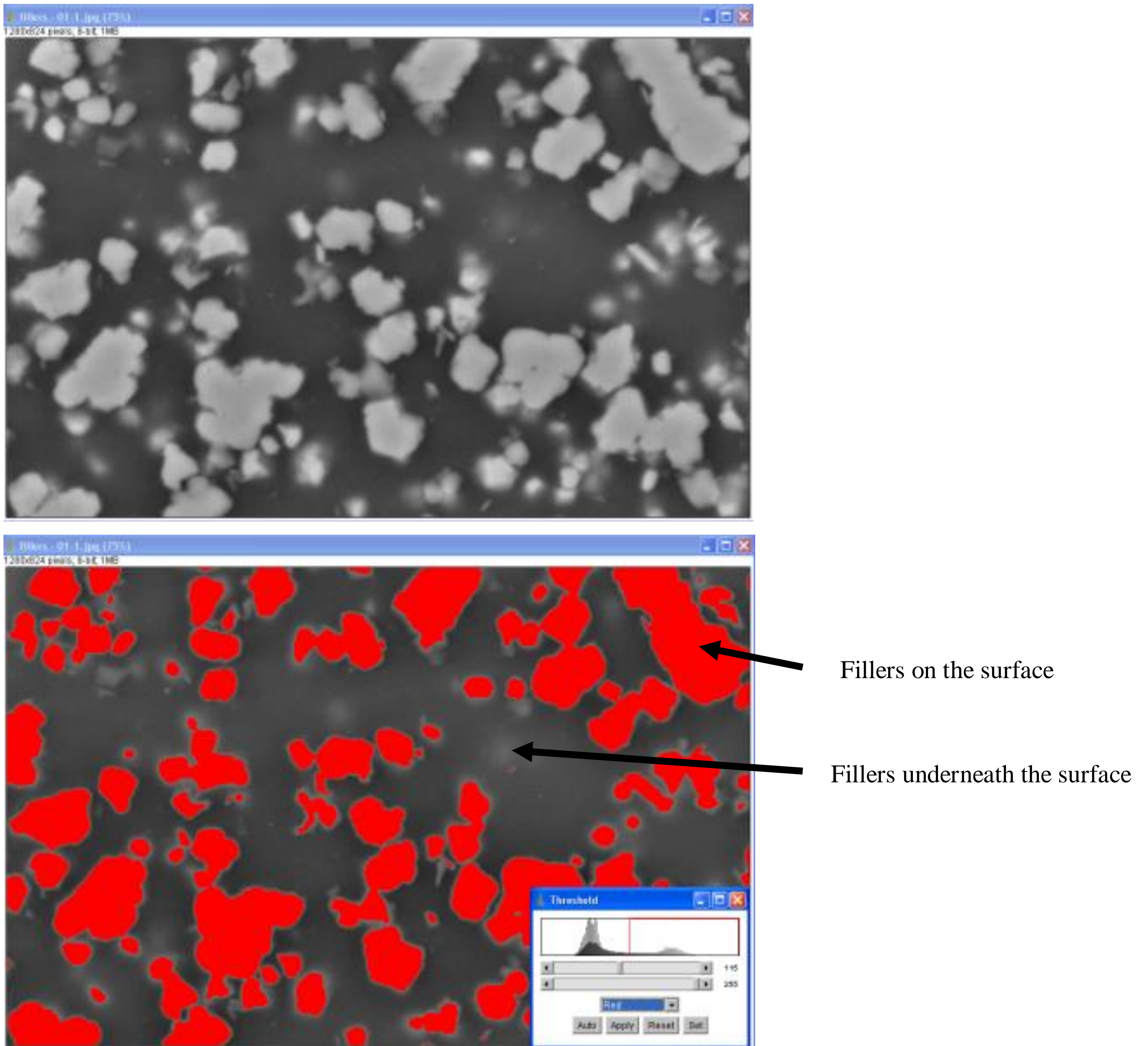

Figure 3-3: ImageJ analysis on fillers area percentage

3.2 Thermal properties analysis

The methods for measuring glass transition temperature, coefficient of thermal expansion in x-y, and z-axis, time to delamination, temperature to decomposition and interconnect stress test are included in this section.

3.2.1 Glass transition temperature (T_g)

The three common methods used to measure glass transition temperature for PWB base materials are differential scanning calorimetry (DSC), thermomechanical analysis (TMA), and dynamic mechanical analysis (DMA) [26]. All samples were tested for their T_g based on the IPC-TM-650 2.4 Test Methods Manual.

3.2.1.1 Differential scanning calorimetry (DSC)

DSC measured the difference in heat absorption or release during the property changes in polymer materials [27]. As the epoxy resin went through the crystalline transition from glassy to rubbery state, the change in heat flow could be detected by the DSC and T_g could be calculated as shown in Figure 3-4.

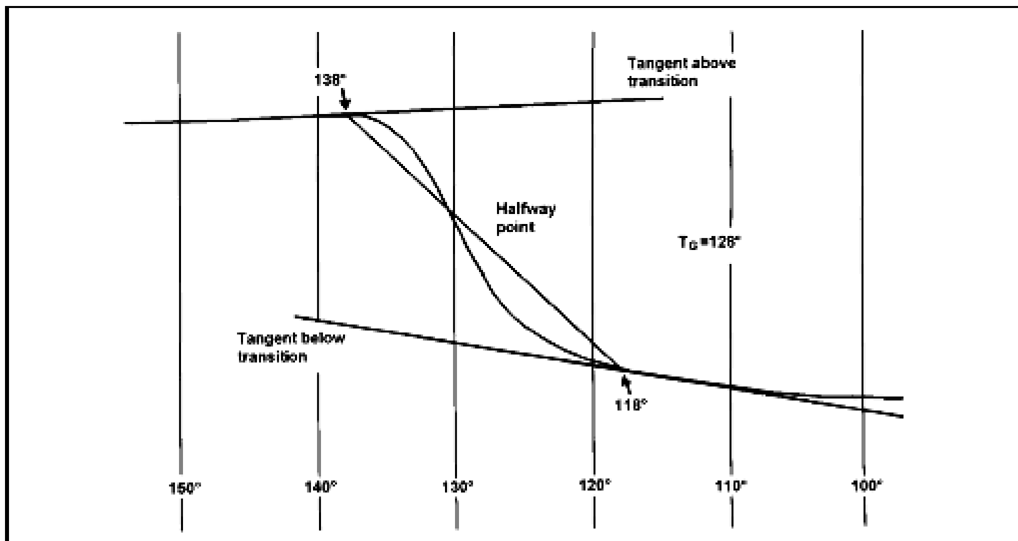

Figure 3-4: Glass transition temperature calculated by DSC midpoint method [28]

All samples were tested based on the IPC-TM-650 2.4.25 Test Method. A TA Instrument – DSC Q100 was used. A sample size of 5 was used with a weight between 15 and 25 mg. All samples were preconditioned at 105±2ºC for 2 hours in an air circulating oven. They were cooled to room temperature in a desiccator for more than 1 hour before testing. The samples were placed in an aluminum sample pan and sealed with an aluminum lid using a DSC sample press. The samples were then transferred into the DSC chamber and heated at a rate of 20ºC/min from room temperature to 190ºC or 210ºC depending on the T_g of the materials. Generally, the peak temperature was 40ºC above the transition region. The samples were held at the peak temperature isothermally for 15

minutes then cooled back to room temperature at a rate of 20ºC/min to eliminate any curing effects. The samples were heated up again from room temperature to the indicated peak temperature at the rate of 20ºC/min to determine the T_g of the materials using the universal V4.5A TA instruments software packages. An example of the DSC curves for a material is given at Figure 3-5.

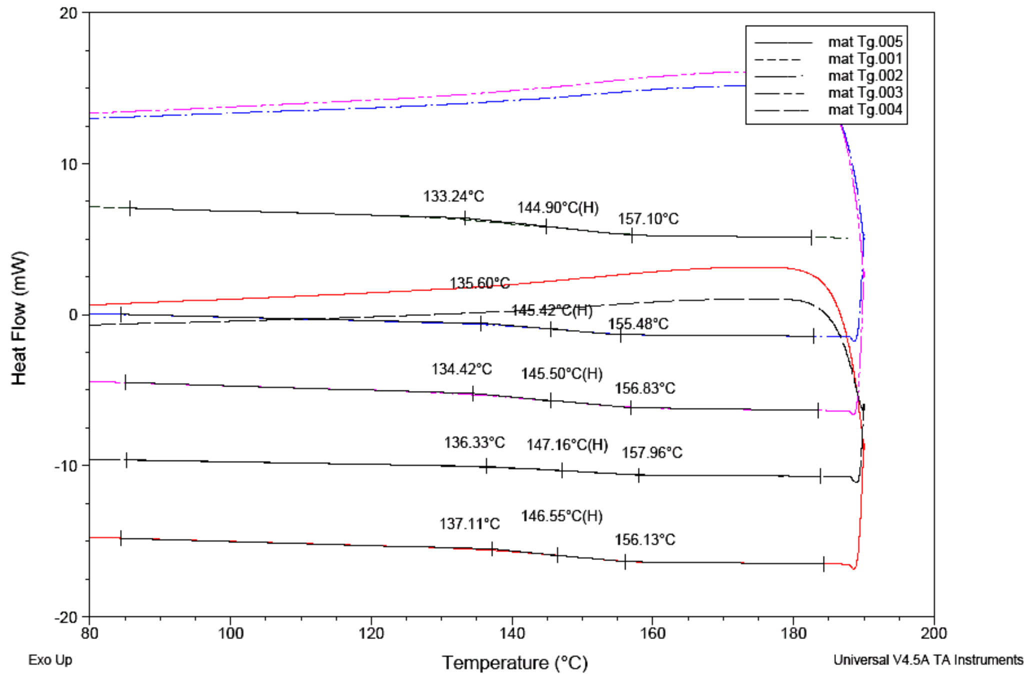

Figure 3-5: Glass transition temperature measured by DSC

3.2.1.2 Thermomechanical analysis (TMA)

As the epoxy resin changed from the glassy to rubbery state, there was a significant change in dimension in the z-axis. The TMA method determined the Tg by the changes in the coefficient of thermal expansion (CTE) of the materials as indicated at Figure 3-6. Point A on the plot was slightly above room temperature where as points B and C were right before the glass transition. Point D is usually the temperature of interest around 250ºC or above. The glass transition temperature was estimated by the intersection between line AB and CD.

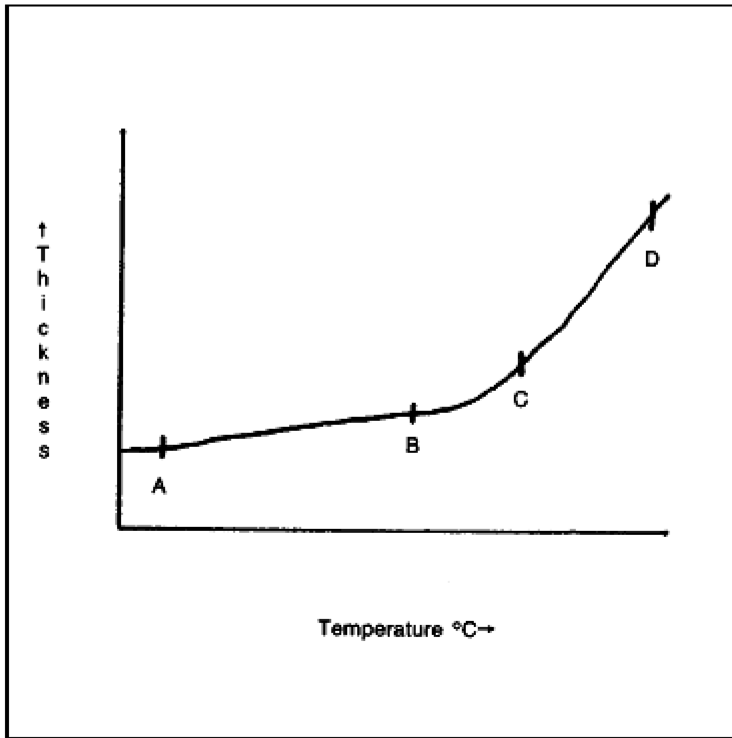

Figure 3-6: Glass transition measured by TMA method [29]

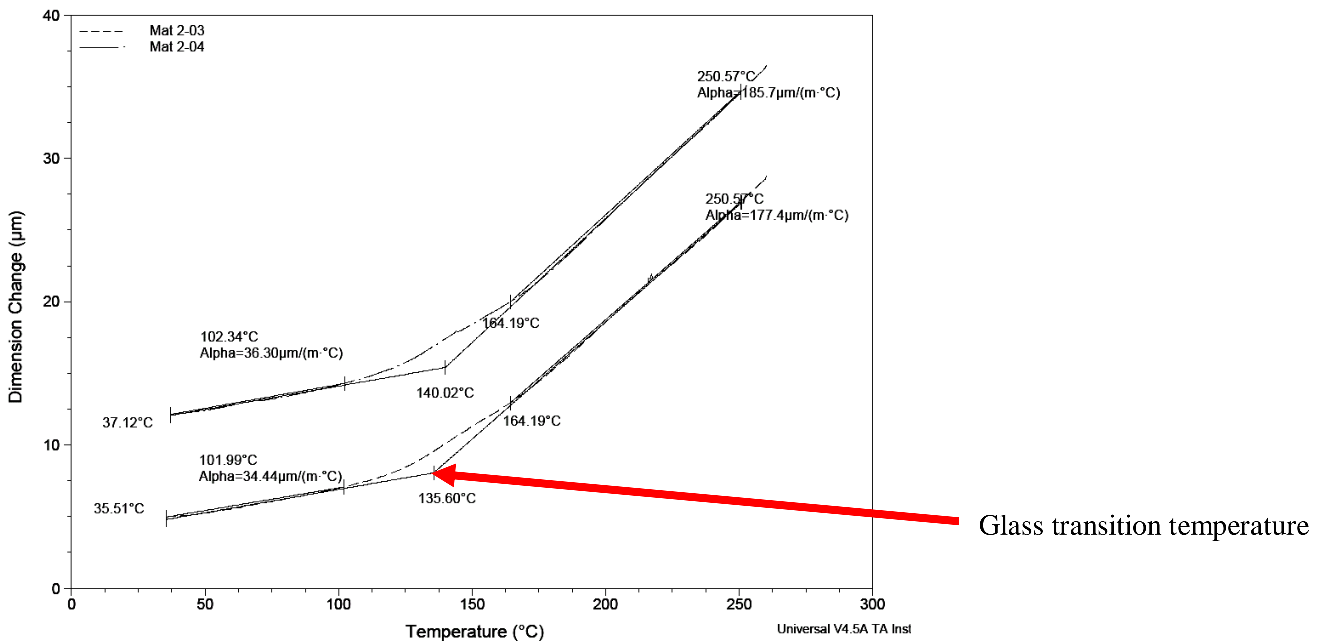

Figure 3-7: TMA curves obtained for measuring glass transition temperature

The IPC-TM-650 Test Method 2.4.24 was followed for this experiment. A TA Instrument – TMA Q400 thermal mechanical analyzer was used. A sample size of 5 was chosen. All samples were preconditioned at 105±2ºC for 2 hours in an air circulating oven. They were cooled to the room temperature in a desiccator before testing for more than 1 hour. The surfaces and edges of the samples were lightly sanded with the 1200 grit fine sand paper to remove any burrs. The thickness of the samples was between 1.2 and 1.4 mm and the dimensions were approximately 6.0mm x 6.0mm. The heating rate was 10˚C/min and the samples were equilibrated at 35 ˚C then heated to 260˚C. The glass transition temperature was calculated using the universal V4.5A TA instruments software packages and shown in Figure 3-7.

3.2.1.3 Dynamic mechanical analysis (DMA)

As the epoxy resin changes its viscoelastic behavior from glassy to rubbery, the elastic modulus (stiffness) also changes and can be detected by the DMA. The DMA monitors the elastic modulus as the sample is subject to increase in temperature. The glass transition temperature is defined at the temperature where tan δ was at its maximum, which was equal to E"/E' where E" is the loss modulus and E' is the storage modulus. This method is demonstrated as Figure 3-8.

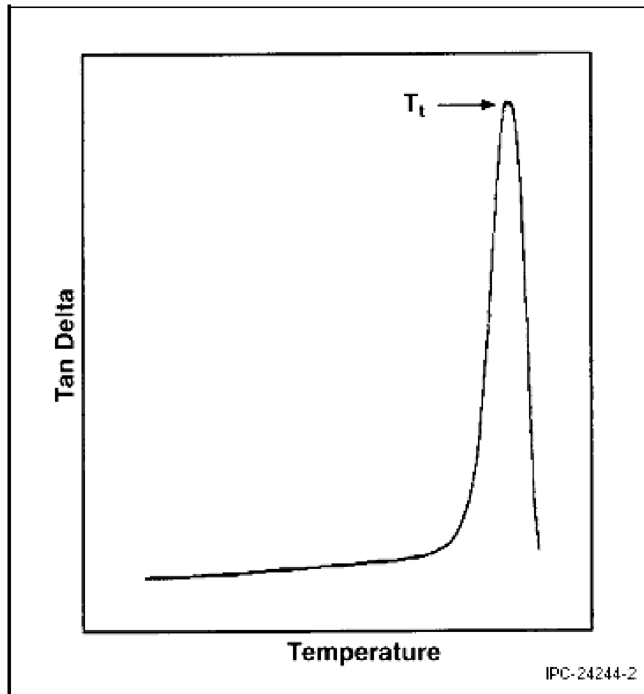

Figure 3-8: Tan delta vs. temperature from DMA curve [30]

The tan δ of the samples was determined by the dynamic mechanical analyzer (TA Instrument – DMA Q800) operated in the dual cantilever mode. The IPC Test Method 2.4.24.4 was used as the reference for the experimental setup. The sample dimension was 55 x 10 mm and the thickness varied from 1.2 to 1.4 mm. A CNC (computer numerical controlled) cutting machine was used to prepare the sample and the width dimension tolerance was within 0.02 mm. All samples were baked at 105℃ for 1 hour and then cooled to room temperature in a desiccator. The applied load was 18 N with an oscillation frequency of 1 Hz. The samples were heated from room temperature to 260℃ with a heating rate of 2℃/min while the tan δ was monitored. A sample size of 5 from each material was used. An example of the DMA curve is given in Figure 3-9 where the peak tan δ is the glass transition temperature.

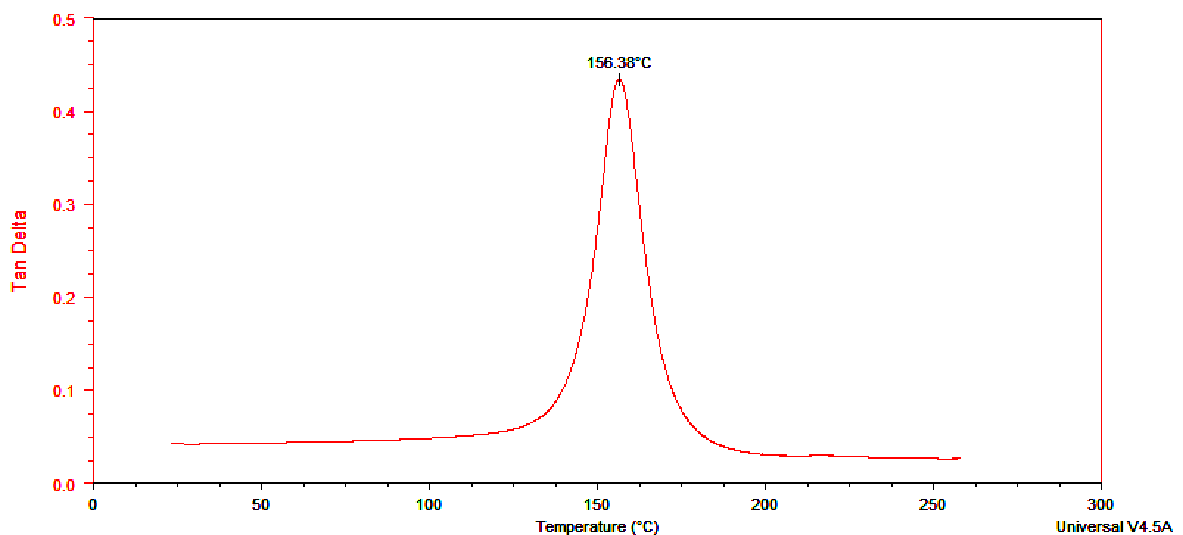

Figure 3-9: Glass transition temperature measured by tan delta peak from DMA

3.2.2 Coefficient of Thermal Expansion (CTE) in x, y, z-axis

The CTE described the expansion of the materials during heating. The glass fibers reinforcement of the PWB were in the x and y directions and they restrain the expansion in the x-y plane, but not in the z-axis. The CTE for the PWB in the z-axis was significantly higher. It was measured in ppm/˚C and the method used was similar to T_g measurement by TMA. The z-CTE was reported before and after T_g, showing that the epoxy resin experienced significant increase in CTE above T_g. The IPC-TM-650 Test Method 2.4.24 was followed for measuring the z-CTE. A TA Instrument – TMA Q400 thermal

mechanical analyzer was used. A sample size of 5 was used. All samples were preconditioned at 105±2ºC for 2 hours in an air circulating oven. They were cooled to room temperature in a desiccator before testing for more than 1 hour. The surfaces and edges of the samples were lightly sanded with the 1200grit fine sand paper to remove any burrs. The thickness of the samples was between 1.2 and 1.4 mm and the dimensions were approximately 6.0mm x 6.0mm. The heating rate was 10˚C/min and the samples were equilibrated at 35 ˚C then heated to 260˚C. The z-CTE before and after T_g was calculated using the universal V4.5A TA Instruments software packages as shown in Figure 3-10.

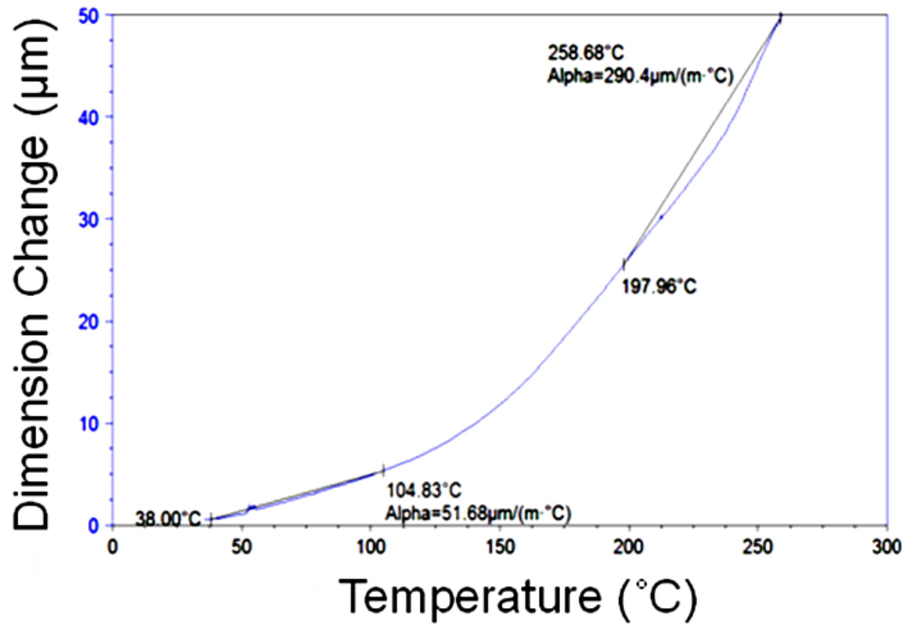

Figure 3-10: CTE in z-axis measured by TMA before and after T_g

The IPC-TM-650 Test Method 2.4.41 was followed for measuring the x and y CTE. The same preparation method, testing conditions, and equipment are the same as were used in the z-CTE test. However, the surface of the samples for measurement has to be perpendicular to the fiber glass. Therefore, an auto grinding machine with 9 µm disk was used to ensure both bottom and top sample surfaces are perpendicular to the fiber glass direction. Also, the TMA probe had to sit on the top of the sample surface properly at the centre to ensure accurate measurement. The TMA measured the height expansion as temperature increases and the CTE was calculated using the software packages as shown in Figure 3-11. A sample size of 3 was used for this test.

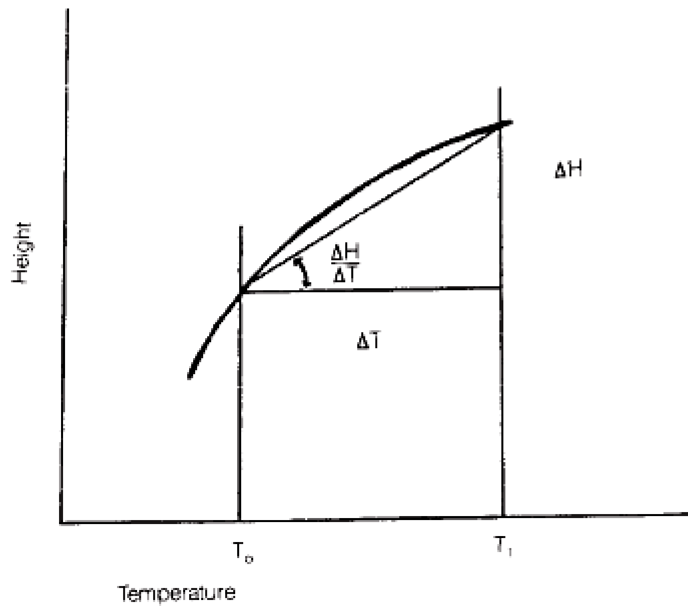

Figure 3-11: CTE in the x and y axis measured by TMA [31]

As the slope between two points of interests was derived, it was divided by the original height of specimen to calculate the average CTE α in x-y axis as shown in the following equation:

$$\alpha = (\Delta H/\Delta T)/H$$

3.2.3 Time to delamination (T260 and T288)

Delamination failure in composite materials was marked by a separation of layers and caused by thermally-induced stress in PWB assembly. The time to delamination at 260˚C and 288˚C tests (T260 and T288) was measured following the IPC Test Method 2.4.24.1. A TA Instrument – TMA Q400 thermal mechanical analyzer was used. A sample size of 5 was used. All samples were preconditioned at 105±2ºC for 2 hours in an air circulating oven. They were cooled to the room temperature in a desiccator before testing for more than 1 hour. The surfaces and edges of the samples were lightly sanded with the 1200 grit fine sand paper to remove any burrs. The thickness of the samples was between 1.2 and 1.4 mm and the dimensions were approximately 6.0mm x 6.0mm. The heating rate was 10˚C/min and the samples were equilibrated at 35 ˚C then heated to 260˚C. The samples were held isothermally at 260˚C for 30 minutes or at 288˚C for 10 minutes. Delamination is marked by the peaks from the TMA curves as shown in Figure 3-12.

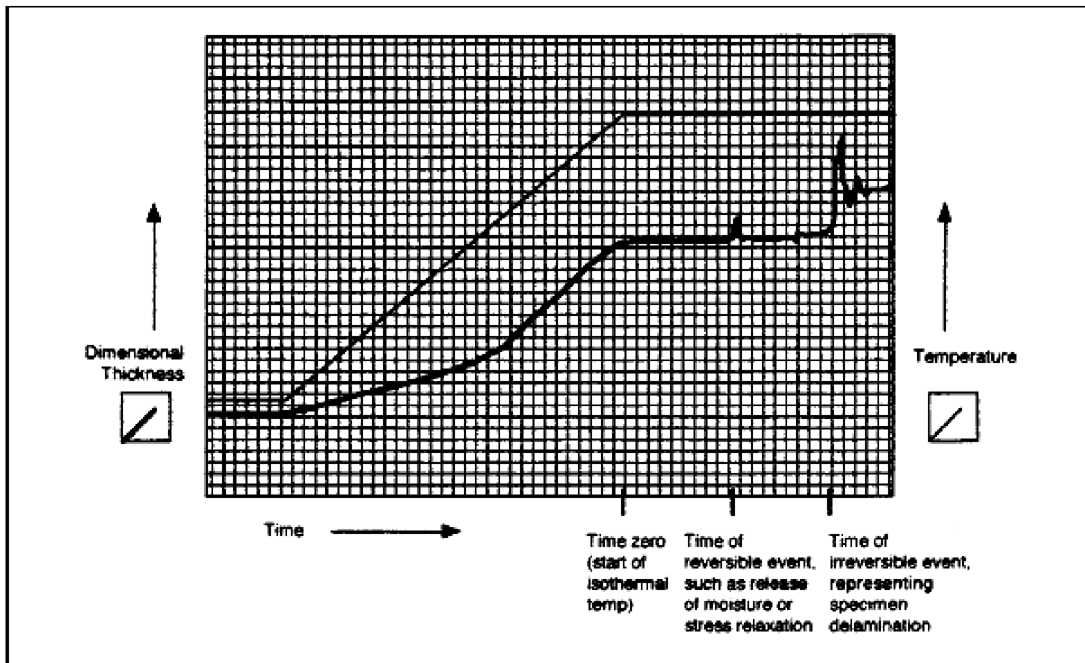

Figure 3-12: TMA curve indicates reversible event and delamination [32]

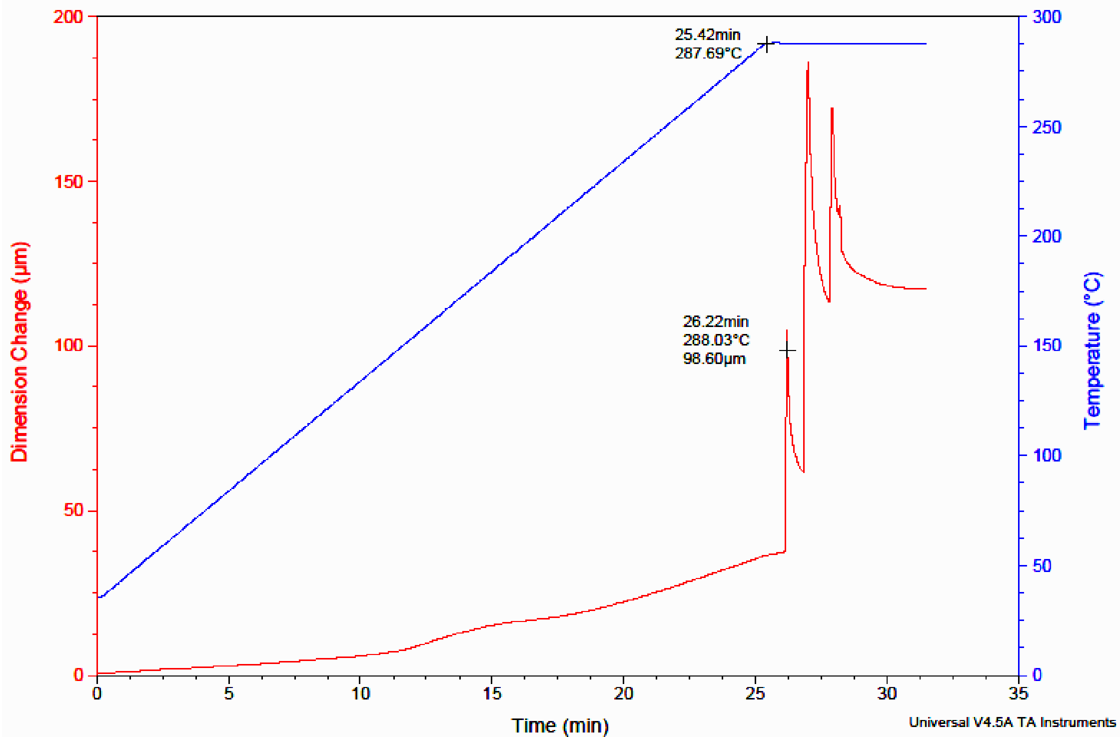

Figure 3-13: TMA curve indicates delamination at 288˚C

A reversible event was the release of moisture or stress relaxation as stated by the IPC where there was no change in dimensional thickness before and after the event. For delamination, it was an irreversible event where there was a permanent change in dimensional thickness after the event. The time to delamination was calculated by the universal V4.5A TA instruments software packages from the time between the start of the isothermal and when the delamination takes place, as shown in Figure 3-13. Also, some materials with weak thermal properties experienced delamination before reaching the isothermal temperature, and their times to delamination were considered to be 0 min.

3.2.4 Temperature to decomposition (T_d)

Decomposition measured the actual physical degradation of the epoxy resin systems. The temperature to decomposition tests followed the IPC-TM-650 Test Method 2.4.24.6. A thermo gravimetric analyzer TA Instrument – TGA Q50 was used for this test. The sample mass was between 10 and 30 mg. A sample size of 5 was used. All samples were preconditioned at 110 ˚C for 24 hours and placed in the desiccator prior to testing for more than one hour. The sample was placed on a copper sample pan since the aluminum pan might experience melting at high temperature. The alumina sample holder from the TGA was used. Since alumina has a porous structure, it was first heated to high temperature to remove any residue before use with samples. The high temperature involves a heating rate of 100˚C/min from room temperature to 800˚C and held isothermally for 3 mins. The TGA nitrogen gas purge had to run for at least 30 minutes before inserting a sample to assure proper gas flow [33]. The sample mass was between 10 and 30 mg. The heating rate was 10˚C/min and the samples were heated from 50˚C to 550˚C. A sample of the TGA curve for temperature to decomposition measurement is given at Figure 3-14. The temperature to decomposition was recorded as 1%, 2%, and 5% weight loss of the sample from the universal V4.5A TA instruments software packages. It indicated the temperature at which there was a 1%, 2%, and 5% weight loss due to physical degradation. The derivative weight change with temperature was also derived from the software. It measured the rate of weight loss due to the physical degradation of the epoxy resin systems. The higher the derivative weight change the faster the decomposition was at that instantaneous temperature. A sample of the derivative curve is shown in Figure 3-15.

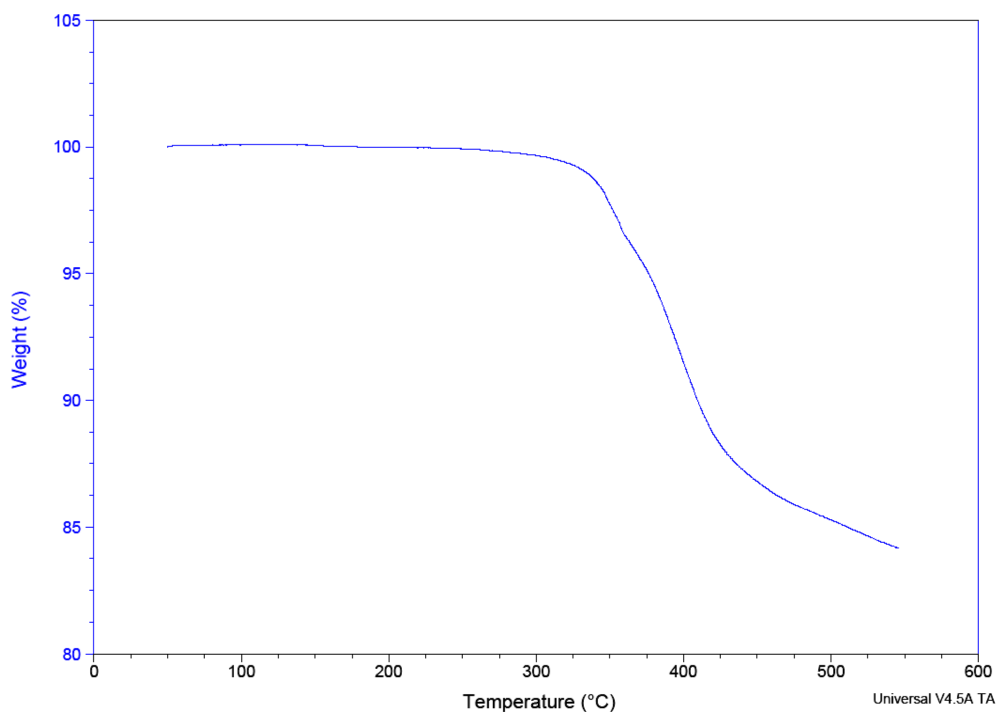

Figure 3-14: TGA curve for temperature to decomposition measurement

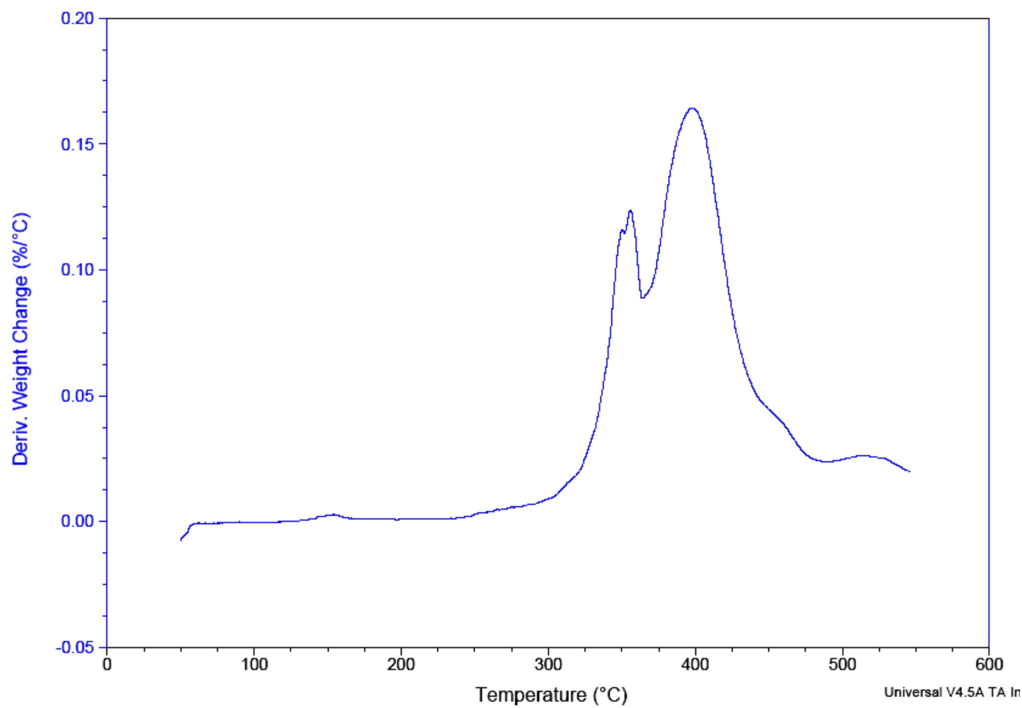

Figure 3-15: The derivative weight change with temperature curve from TGA

3.2.5 Interconnect stress test (IST)

The IST test measured changes in resistance of plated-through hole (PTH) barrels and internal layer connections by applying a DC current to induce thermal cycling. The DC current heated up the IST test coupon to 190˚C for 3 minutes and then applied a forced air cooling to cool the coupon back to room temperature. This thermal cycling induces cyclic fatigue strain in the PTH (Plated Thru Hole) barrel and internal layer connection, where failure is defined to be when the coupon's resistance increases by 25%, which indicates a crack opening up. An image of a typical daisy chain test coupon is given at Figure 3-16.

Figure 3-16: Typical daisy chain test coupon for IST test [34]

The current was applied from the power side and through the PTH and internal layer connections to the sense side. The resistance was monitored for any significant changes in resistance that might indicate crack opening, which is shown as Figure 3-17.

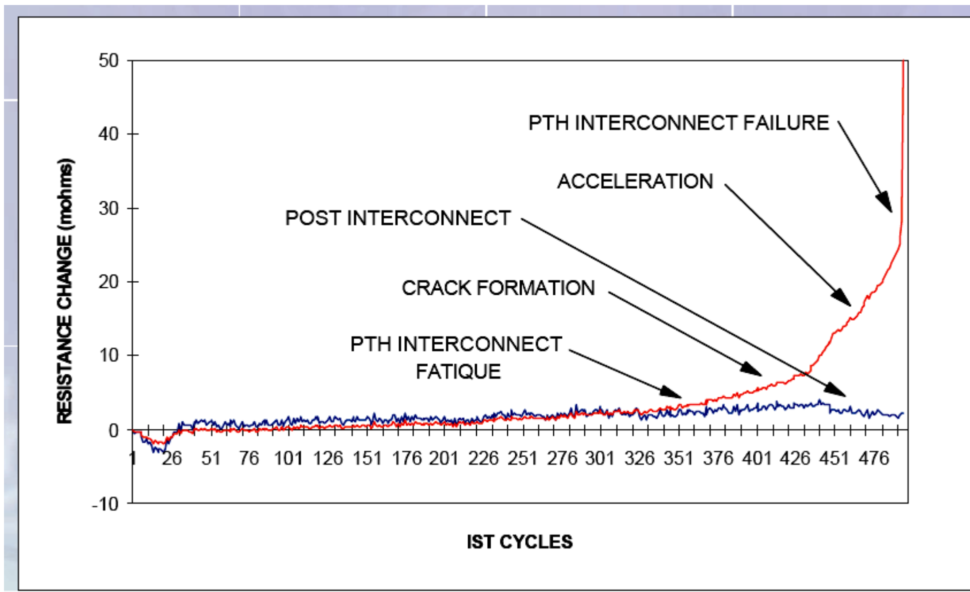

Figure 3-17: Resistance curve indicated a crack opening in the PTH barrel [34]

The failure occurred when there was a significant increase for the PTH barrel resistance indicated by the red line. The cycles to failure were recorded and represent the PWB integrity when subjected to thermal cycling. The maximum cycles were 1000 where the IST tests automatically terminate. The data were recorded every 25 cycles to avoid data overload. Each coupon was placed as close to centre as possible to the forced air fan for proper cooling. A sample size of 5 was used in this test. This test used IPC-TM650 test methods 2.6.26 as a reference.

3.3 Mechanical properties analysis

Different mechanical properties of the PWB samples were analyzed and they included flexural strength, energy to fracture, flexural modulus, Vickers hardness, and copper peel test. The methodology and experimental conditions were given in the following.

3.3.1 Flexural strength

The three-point bending test was performed to determine the flexural strength of the PWB samples. An Instron tensile machine (Instron 5548 MicroTester) was used. The IPC Test Method 2.4.4 was used as the experimental reference. The sample dimension was 132mm x 77mm and the thickness varied from 1.2 to 1.4 mm. The maximum applied load was between 500 and 600 N to achieve fracture of the sample. The speed of testing was 1.27 mm/min and the span was 58.6 mm. The flexural strength was then calculated based on the following formula [35]:

$$S = \frac{3PL}{2bd^2}$$

Where S is the flexural strength, P is the load at breaking, L is the span, b is the width and d is the thickness of the sample. Also, the load from the tensile machine had to be aligned with the surface of the sample before each test and the load had to be placed as close to centre as possible. A schematic drawing of the three-point bending test is given at Figure 3-18. The stress and strain curve was obtained from the Instron tensile machine to determine the flexural strength, which is shown in Figure 3-19.

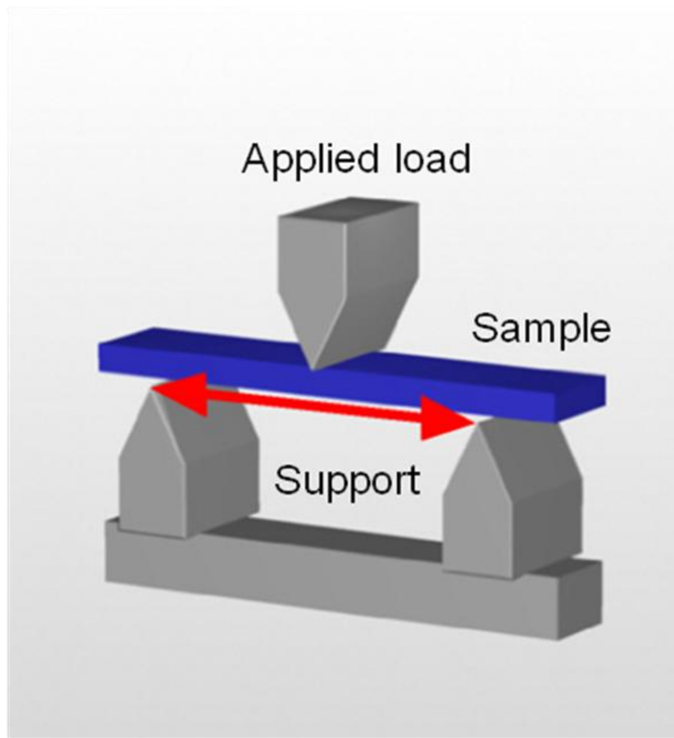

Figure 3-18: Schematic drawing of the three-point bending test [36]

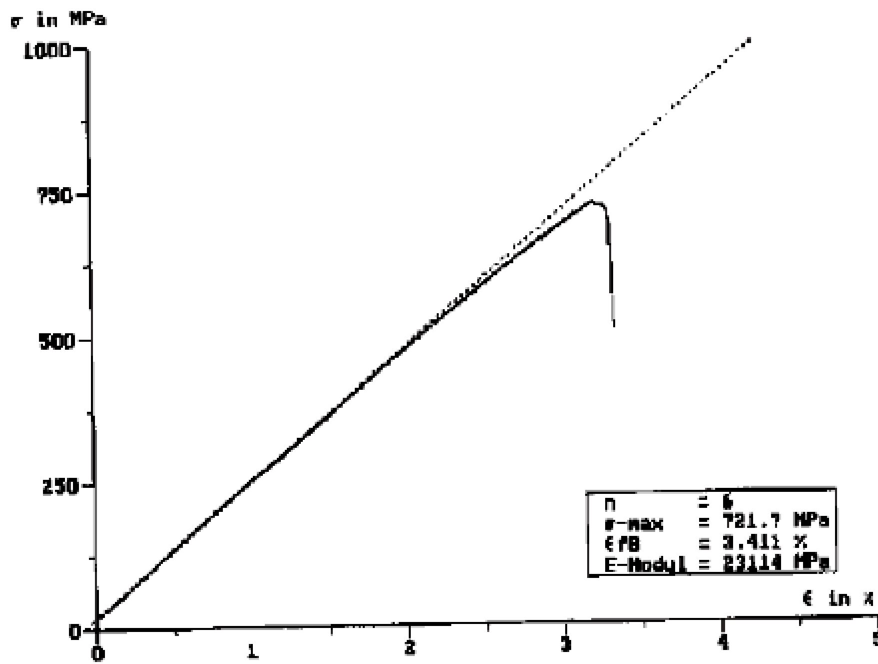

Figure 3-19: Typical flexural strength measurement curve [37]

3.3.2 Energy to fracture

Similar to the flexural strength, the three-point bending test was performed to determine the energy to fracture of the PWB samples. An Instron tensile machine (Instron 5548 MicroTester) was used. The IPC Test Method 2.4.4 was used as the experimental reference. The sample dimension was 132mm x 77mm and the thickness varied from 1.2 to 1.4 mm. The maximum applied load was between 500 and 600 N to achieve fracture of the sample. The speed of testing was 1.27 mm/min and the span was 58.6 mm. After the load-extension curve was obtained from the Instron tensile machine, the Instron software could calculate the energy to fracture based on the area under the curve as shown in Figure 3-20.

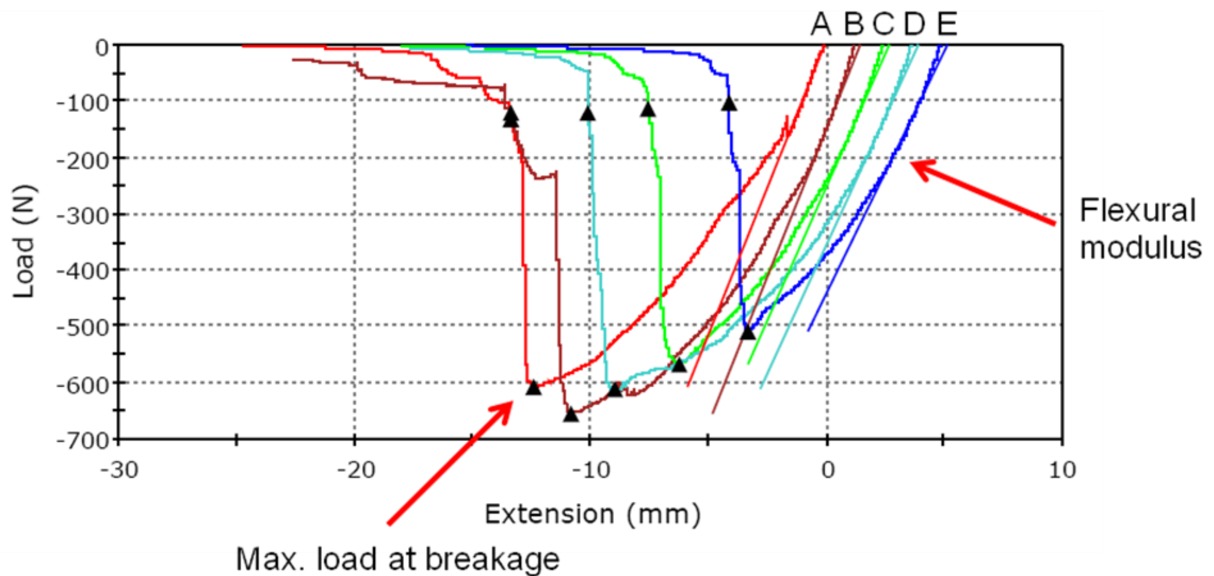

Figure 3-20: Load-extension curve obtained from the Instron tensile machine

3.3.3 Flexural modulus

The flexural modulus of the samples was determined by the dynamic mechanical analyzer (TA Instrument – DMA Q800) operated in the dual cantilever mode. The IPC Test Method 2.4.24.4 was used as the reference for the experimental setup. The sample dimension was 55 x 10 mm and the thickness varied from 1.2 to 1.4 mm. CNC (computer numerical controlled) cutting machine was used to prepare the sample and the width dimension tolerance was within 0.02 mm. The applied load was

18 N with an oscillation frequency of 1 Hz at room temperature. The schematic of the experimental setup is shown in Figure 3-21.

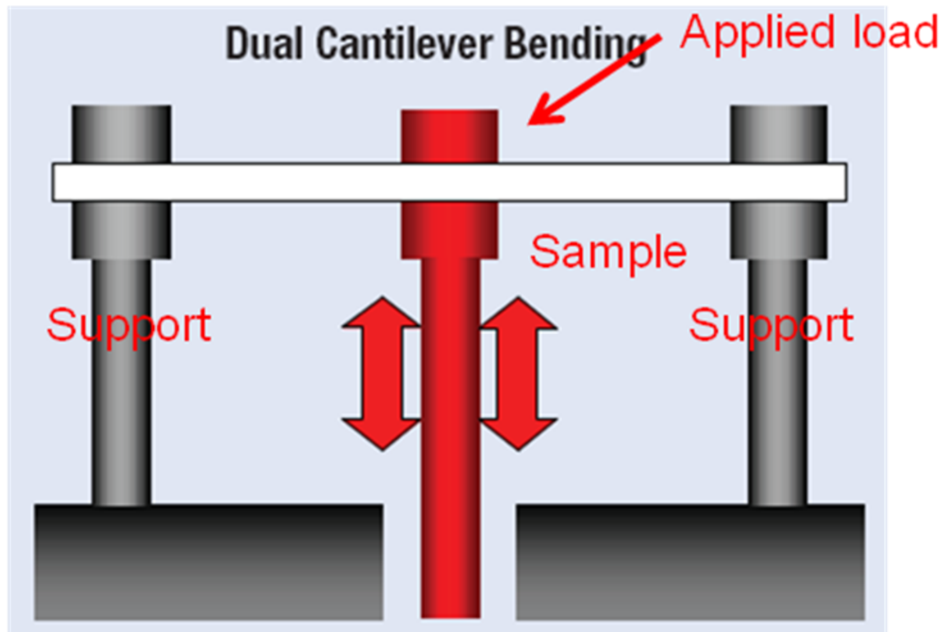

Figure 3-21: Schematic drawing of the dual cantilever bending mode of DMA [38]

Both stationary and load supports were tightened with 10lb force to clamp the samples. The samples were placed as near the centre as possible. The flexural modulus (storage modulus) measurements were received from the DMA and processed by the universal TA software packages. An example of the modulus curve was shown in Figure 3-22. The modulus value was obtained near the 25˚C (room temperature). Since the epoxy resin was sensitive to temperature, it was important to obtain the modulus as near room temperature as possible. The flexural modulus was plotted on a logarithmic scale since the modulus had a significant decrease above the glass transition where the epoxy resin became rubbery and elastic with very low modulus.

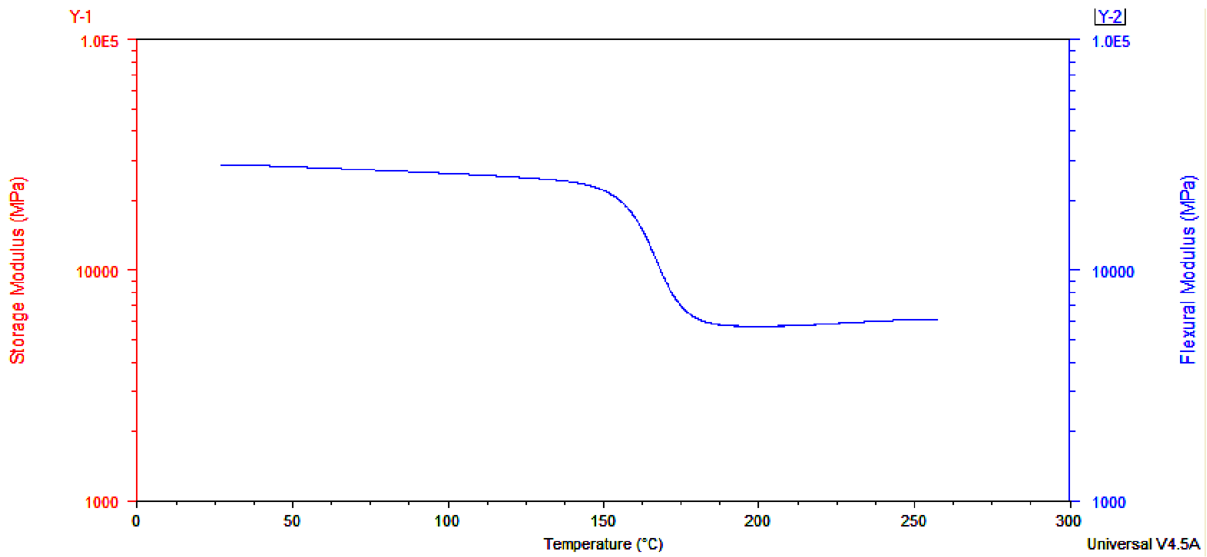

Figure 3-22: Storage modulus curves for different materials from DMA

3.3.4 Vickers hardness

The Vickers hardness was measured using the micro-hardness tester (Matsuzawa MMT-7 Microhardness Tester) at the cross-section of the samples. All samples were cross-sectioned, mounted, sanded, and polished using standard materialographic procedure. The indentation was made on the epoxy with or without fillers as shown Figure 3-23. The applied load was 50g (490.3mN) with a loading time of 10 seconds. The indent had to be located not too close to the glass fibers and copper to avoid inaccurate measurement of the epoxy Vickers hardness. The 50 g load had the optimum indent size for hardness measurement for these materials. The surface of the sample should have minimal scratches. 10 random locations for each material were measured using the same condition.

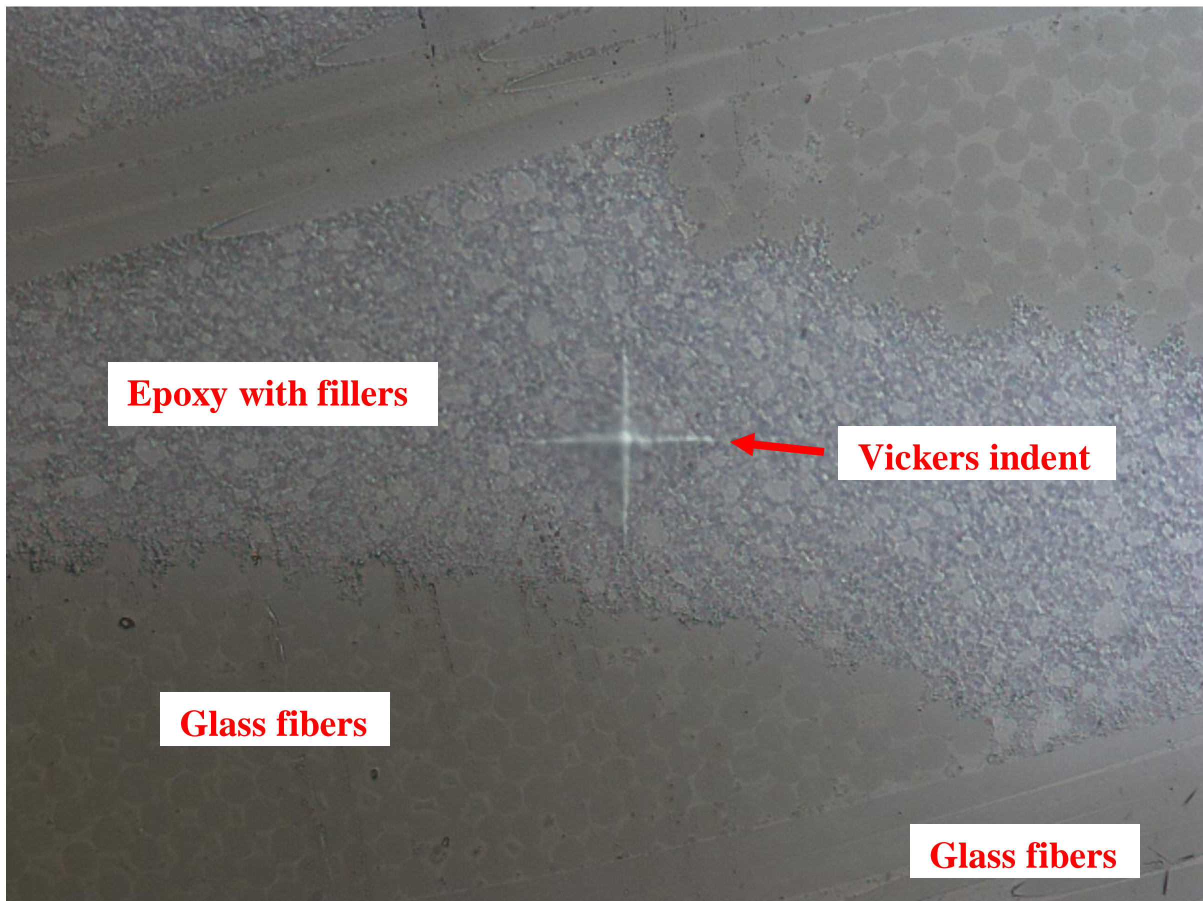

Figure 3-23: Vickers indent on the epoxy

3.3.5 Copper peel strength

The IPC-TM-650 2.4.8 Test Method manual was used as the reference for this test. A DAGE series 4000 shear tester was used with a 5KG load cell equipped. Each test coupon was peeled vertically with an initial distance of more than 25.4 mm. A sample size of 5 was used for each material. The testing speed was 50.8mm/min and the load was 1 kg. The stage of the shear tester was held by vacuum to avoid any movement of the stage during the peel test. Both the load and peel distance were recorded by the shear tester as shown in Figure 3-24. All samples showed high peel strength failure mode and no low peel strength failure mode was observed. Also, the width of the copper had to be measured in order to calculate the peel strength. A HIROX digital microscope KH-7700 was used to

measure the copper width and it had to be calibrated before measurement. The peel strength was averaged for the peel distance in high peel strength failure mode and recorded as N/mm.

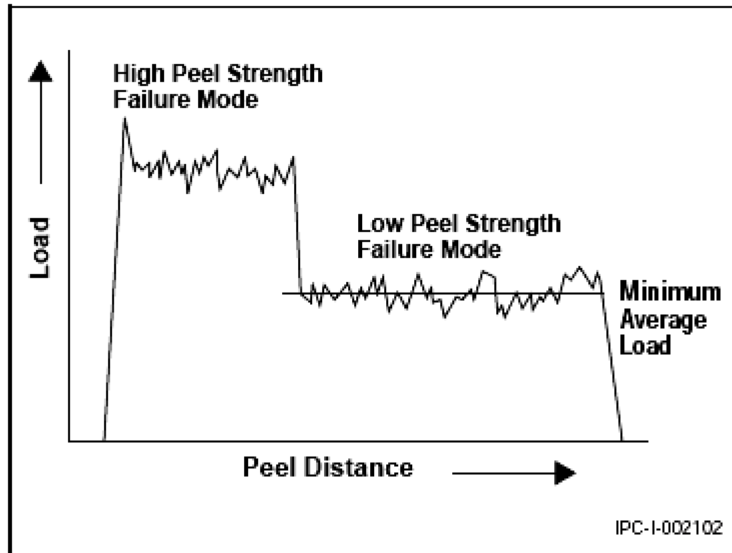

Figure 3-24: Load vs. peel distance obtained from the peel test [39]

3.4 Electrical properties

The IPC-TM-650 Test Method 2.5.51 was used as the reference for this test. All samples were baked at 105ºC for 2 hours and preconditioned at 23ºC and 50% relative humidity for more than 24 hours as recommended [40]. A High Frequency (3.2GHz): Resonance Method Performance Network Analyzer Agilent E 8362B (equipped with Split Post Dielectric Resonator cell) was used. Both the dielectric constant and dissipation factor were measured at 3.2GHz.

Chapter 4

RESULTS

This section includes all experimental results from chemical and physical analysis on epoxy and fillers, thermal properties, mechanical properties, and electrical properties analysis. Tables and graphs are given to display the average values.

4.1 Chemical and physical analysis on epoxy and fillers

4.1.1 Epoxy characterization

Bromine is found in halogenated laminates from the EDS Mapping analysis. However, it is also known that the aluminum and bromine have a similar x-ray emission line, where the Lα of bromine is 1.480keV and the Kα of aluminum is 1.486keV [43]. Therefore, it is hard to distinguish the difference at this range when both brominated epoxy and aluminum hydroxides fillers are present. One solution is to use the Kα peak of bromine to confirm the presence of the brominated compound. The Kα peak of Bromine is 11.90keV, which is shown in Figure 4-1. Materials without brominated epoxy and with Aluminum hydroxides fillers only show Aluminum peak at 1.486 keV and no peak is found at the 11.90 keV, which is shown in Figure 4-2. This is a useful way to distinguish the difference between bromine and aluminum. After the EDS peaks have been defined for the corresponding elements, the mapping analysis is performed to distinguish the epoxy chemistry. Figure 4-3 shows an example from the mapping analysis for halogenated and halogen-free materials. Material A is a traditional FR-4 material with brominated epoxy while Material F is a halogen-free material with phosphorus compound in its epoxy backbone. One of the main differences between traditional FR-4 and halogen-free laminates is the flame retardants used in the epoxy. Traditional FR-4 and other halogenated laminates insert brominated compound to the epoxy backbone, which can retard combustion by forming insulation gas against oxygen intrusion and capturing radicals from the epoxy [17]. Halogen-free laminates contain phosphorus compounds in the epoxy backbone as the flame retardant substitutes, which induce char formation upon combustion and suppress the flame.

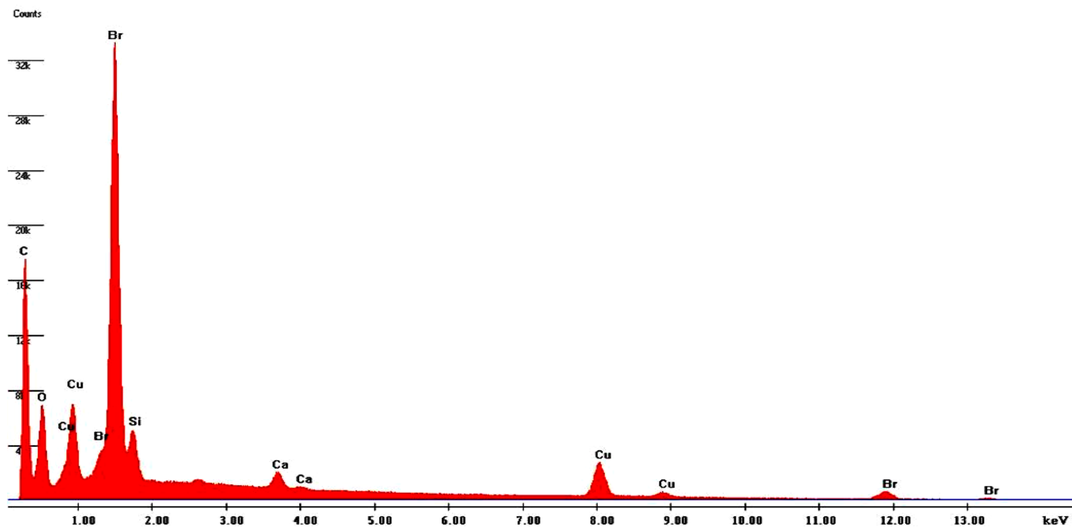

Figure 4-1: Detection of bromine Lα and Kα peaks from the EDS analysis

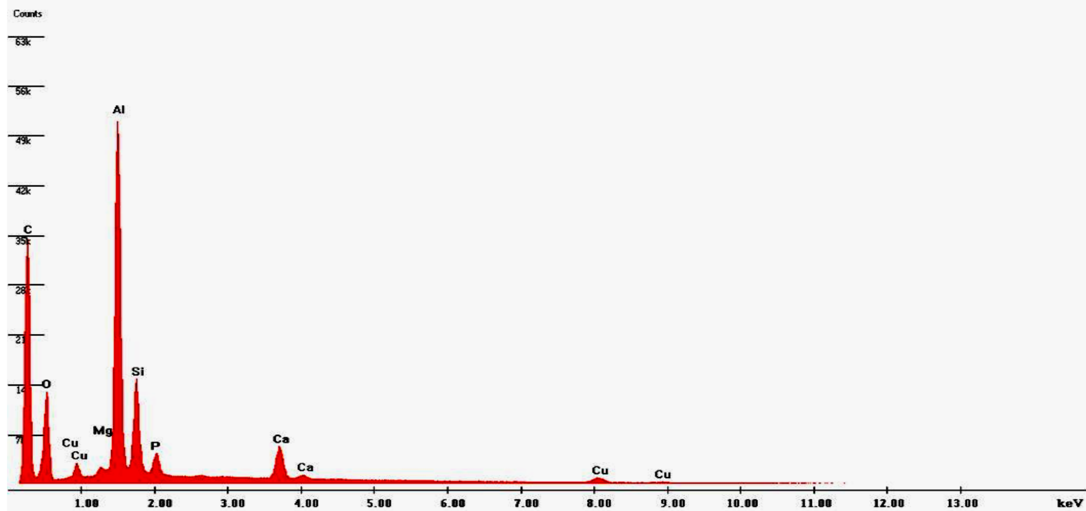

Figure 4-2: Detection of aluminum from the aluminum hydroxide fillers from EDS

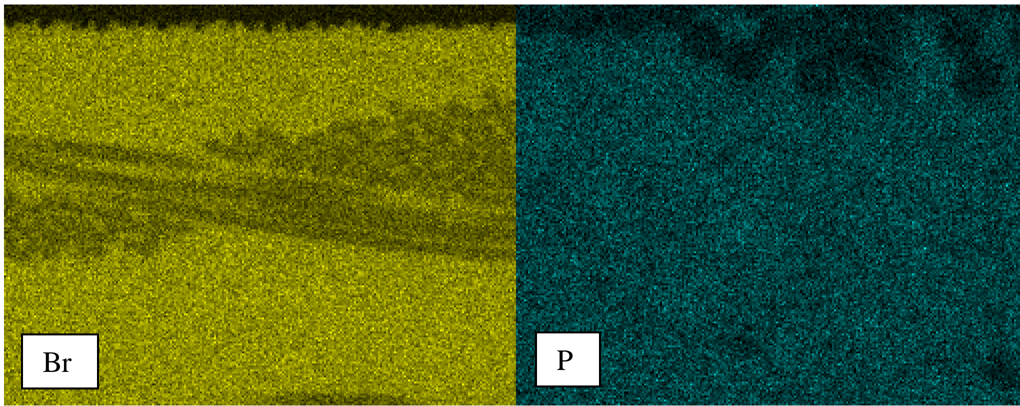

a) Material A b) Material F

Figure 4-3: EDS mapping analysis for material A and material F

4.1.2 Fillers characterization

Different fillers are found for different PWB materials and their chemical composition, shape and volume percentage are analyzed.

4.1.2.1 Chemical composition

Three different types of fillers are found in the PWB materials: SiO_2, $Al(OH)_3$, and $Mg(OH)_2$. The SiO_2 is used to reduce the CTE of the PWB materials while both $Al(OH)_3$, and $Mg(OH)_2$ are the flame retardant replacements for halogen-free materials. The elemental mapping analysis in Figure 4-4 shows the presence of these fillers.

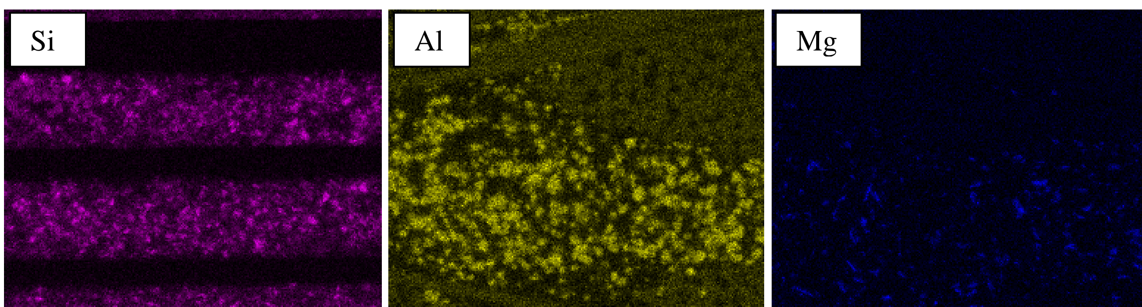

Figure 4-4: EDS mapping analysis for different types of fillers

Silicon, aluminum and magnesium not only can be detected from the fillers, but also can be found in the E-glass fibers due to the presence of their oxides.

4.1.2.2 Shape

The shapes of different types of fillers are studied using the SEM. Silica particles are found to be varied in sizes and have an angular shape. Aluminum hydroxide has globular shape while magnesium hydroxide is lath-like. Figure 4-5 demonstrates the difference in shapes for these fillers.

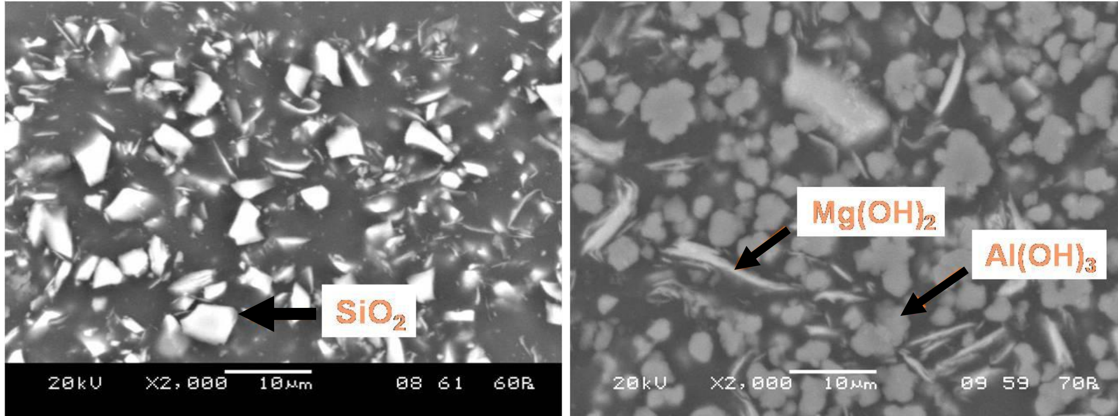

Figure 4-5: SEM analysis demonstrates the different in shapes for different fillers

4.1.2.3 Volume percentage

In order to further increase the flame retardancy, metal hydroxides are added into the epoxy for halogen-free laminates. The filler volume percentages for all studied materials are given at Table 4-1. Also, Table 4-2 gives the summary for the types of fillers and epoxy used for all materials. Materials A-C have halogenated epoxy while D-G are the halogen-free materials. Silica fillers are also found in some of the halogenated and halogen-free laminates. Aluminum hydroxides have a much higher volume percentage than magnesium hydroxides. The types of fillers and their volume percentage have a significant effect on both thermal and mechanical properties and will be shown in this study.

Table 4-1: Fillers volume percentage for different materials

Material	SiO_2 %	$Al(OH)_3$ %	$Mg(OH)_2$ %
A	0	0	0
B	19.1	0	2.0
C	37.1	17.5	0
D	0	29.8	0
E	0	32.0	3.5
F	19.4	0.8	0
G	11.65	8.54	0

Table 4-2: Summary of different types of fillers and epoxy found in all materials

Material	Fillers	Epoxy	Curing agent
A	No Fillers	Brominated	Dicyandiamide
B	SiO_2, $Mg(OH)_2$	Brominated	Dicyandiamide
C	$Al(OH)_3$, SiO_2	Brominated	Dicyandiamide
D	$Al(OH)_3$	Phosphorus doped	Phenolic
E	$Al(OH)_3$, $Mg(OH)_2$	Phosphorus doped	Dicyandiamide
F	$Al(OH)_3$, SiO_2	Phosphorus doped	Dicyandiamide
G	$Al(OH)_3$, SiO_2	Phosphorus doped	Phenolic

4.2 Thermal properties analysis

The experimental data for glass transition temperature (T_g), coefficient of thermal expansion (CTE), time to delamination (T260 and T288), temperature to decomposition (T_d) and interconnect stress test (IST) are given in this section.

4.2.1 Glass transition temperature (T_g)

Three different glass transition temperatures are given for each material from the DSC, TMA, and DMA measurements as listed at Table 4-3.

Table 4-3: Summary of glass transition temperatures measuring by different methods

Material	T_g (°C) DSC	T_g (°C) TMA	T_g (°C) DMA
A	141.7±0.4	137.4±3.4	155.5±0.6
B	154.2±0.4	143.5±2.5	168.3±0.9
C	170.5±0.8	151.3±2.1	182.4±1.0
D	149.8±2.9	146.2±3.5	183.5±0.5
E	153.0±0.7	152.6±2.6	171.9±0.6
F	153.1±0.7	143.6±2.6	170.9±0.3
G	149.2±2.2	144.0±4.5	174.8±0.6

4.2.2 Coefficient of Thermal Expansion (CTE)

Both the out-of-plane (z-axis) CTE and in-plane (x-y-axis) CTE data are given in this section. For the z-axis CTE, the data is separated into before and after T_g. Also, the z-axis CTE changes are provided.

4.2.2.1 Z-axis CTE

The z-axis CTE before T_g is measured from 35°C to 105° while the after T_g is for 190°C to 250°C. The z-axis CTE changes are calculated from the z-axis CTE after T_g minus the before T_g values. The summary of the data is shown in Table 4-4.

Table 4-4: Z-axis CTE data for different materials

Material	Z-CTE before T_g (ppm/°C)	Z-CTE after T_g (ppm/°C)	Z-CTE changes (ppm/°C)
A	49.25±1.80	263.94 ±4.93	214.69±4.69
B	40.17±1.48	226.94±5.41	186.77±4.98
C	24.52±1.82	153.46±14.84	128.94±13.39
D	53.06±1.25	253.28±17.62	200.22±16.65
E	29.34±1.66	213.10±5.85	183.76±7.32
F	38.46±0.99	219.36±3.75	180.90±3.90
G	41.95±4.00	221.56±15.87	179.61±13.24

4.2.2.2 X-Y-axis CTE

The x-y-axis CTE before T_g is measured from 35°C to 105° while the after T_g is from 190°C to 250°C. Due to the difficulty of sample preparation and test conditions, the sample size used for this test is three instead of five, which is also the sample size suggested by the IPC standard. The data is listed at Table 4-5.

Table 4-5: X-Y-axis CTE data for different materials

Material	X-CTE before T_g (ppm/°C)	X-CTE after T_g (ppm/°C)	Y-CTE before T_g (ppm/°C)	Y-CTE after T_g (ppm/°C)
A	14.88±0.63	11.69±1.11	14.70±0.16	14.00±1.33
B	14.63±0.52	12.77±1.57	14.45±0.36	14.19±0.68
C	13.81±0.37	11.37±0.55	14.62±0.53	14.71±1.22
D	14.84±1.05	14.33±1.14	16.51±0.54	16.31±0.78
E	14.73±0.46	14.76 ±0.57	14.71±0.38	13.53±0.42
F	14.63±0.56	14.45±0.64	14.79±0.36	14.35±0.41
G	15.53±0.96	14.56±1.98	14.94±0.85	17.23±0.65

4.2.3 Time to delamination

4.2.3.1 T260 and T288

The test results for time to delamination at 260˚C and 288˚C are provided in this section. Some materials have the values of 0 for T288, which indicates delamination occurred before the temperature reaches 288˚C. The data is given in Table 4-6.

4.2.3.2 SEM analysis

The SEM cross-section failure analysis is performed to observe the delamination modes for each material after the delamination occurred, which is given in Figure 4-6. The arrows show the majority of delamination modes within the cross-section for the material. Also, the majority of the delamination takes place at the HDI layers. The delamination between copper and epoxy always occurs at the smooth side of the copper.

Table 4-6: Time to delamination at 260˚C and 288˚C

Material	T260 (mins)	T288 (mins)
A	2.15±0.41	0
B	8.52±0.78	0.60±0.52
C	23.49±2.69	1.42±0.49
D	4.25±0.67	0
E	4.86±1.24	0
F	39.76±3.95	2.76±0.30
G	6.88±0.89	0.29±0.31

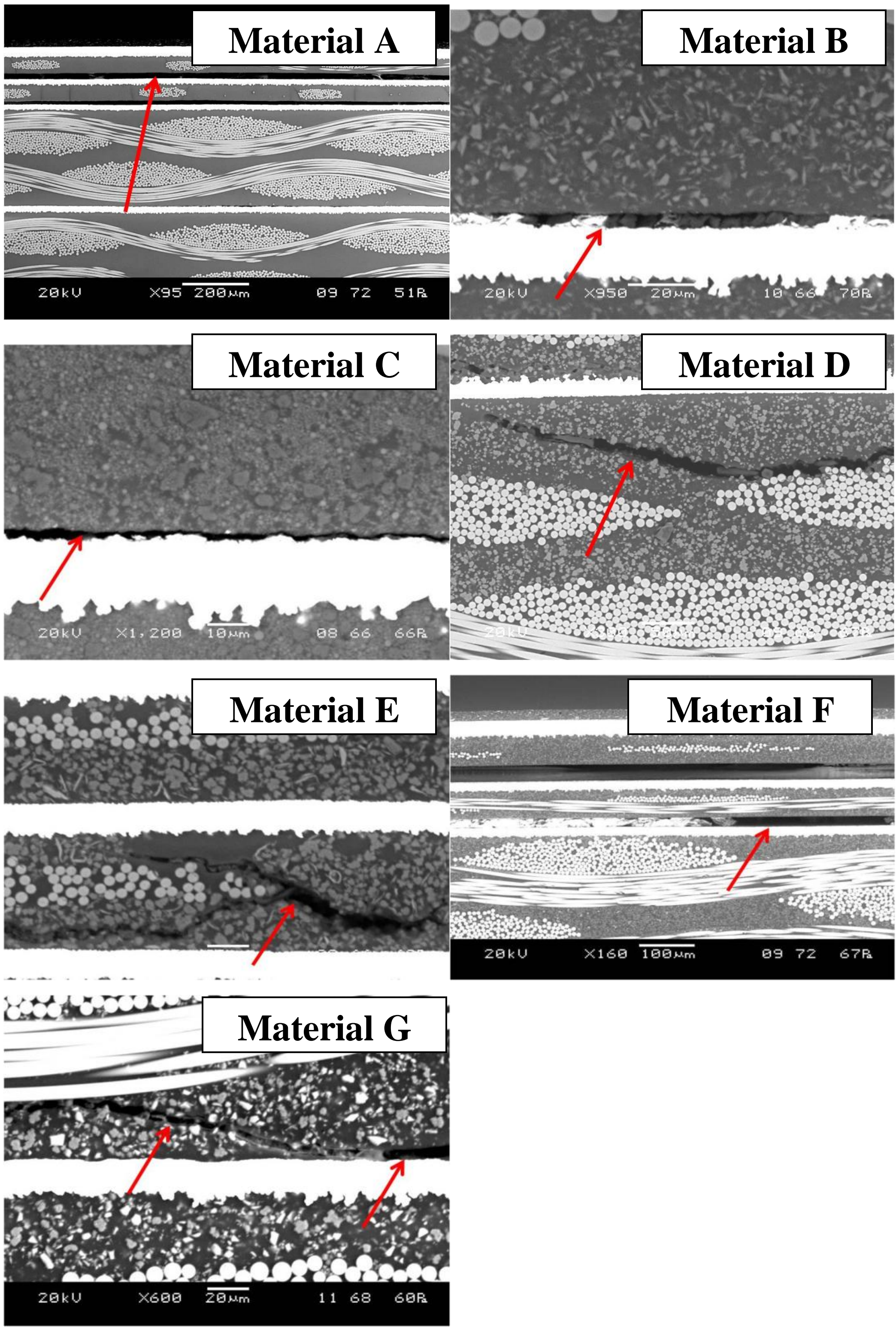

Figure 4-6: SEM cross-section failure analysis on delamination for each material

4.2.4 Temperature to decomposition (T_d)

4.2.4.1 T_d at 1, 2, and 5 weight % loss

The temperature at which decomposition of the epoxy system leads to a 1, 2 and 5 weight % loss for each material is given at Table 4-7.

Table 4-7: Temperature to decomposition in ˚C at different weight loss for each material

Material	Td (1%)	Td (2%)	Td (5%)
A	313.46±0.94	318.38±1.91	323.19±1.17
B	332.90±0.71	334.77±1.57	340.43±1.30
C	343.75±1.51	353.40±1.02	362.68±5.47
D	320.47±2.74	335.96±1.75	366.53±1.05
E	333.00±0.79	346.89±0.75	375.57±0.65
F	343.20±2.20	358.39±1.59	379.85±1.45
G	339.46±0.57	358.53±0.76	393.86±0.40

4.2.4.2 Derivative weight changes

The derivative weight changes at 260˚C for each material are given in Table 4-8. It indicates the rate of weight loss at the instantaneous temperature, which is related to the decomposition of both the epoxy and aluminum hydroxides filler if it is present in the material.

Table 4-8: Derivative weight changes at 260˚C for each material

Material	Derivative Weight Change at 260˚C (%/˚C)
A	0.0014±0.0003
B	0.0014±0.0005
C	0.0030±0.0004
D	0.0063±0.0004
E	0.0045±0.0004
F	0.0018±0.0005
G	0.0033±0.0002

4.2.5 Interconnect stress test (IST)

4.2.5.1 Cycles to failure

The IST cycles to failure results from each material are listed at Table 4-9. The longer the cycles to failure, the more resistance the copper plated through hole has to fail by thermal stress. Some materials are missing in the IST test due to the fact that their test coupons are not available.

Table 4-9: IST cycles to failure for each material

Material	IST cycles to failure
A	78±17
D	88±7
E	202±69
G	893±76

4.2.5.2 SEM analysis

After the test coupon failed, it was cross-sectioned and analyzed with SEM for cracks. Two different cracks are found from the SEM analysis: barrel and knee crack. The barrel crack is found inside the copper plated through hole while the knee crack is located at the corner of the through hole and they are shown in Figure 4-7.

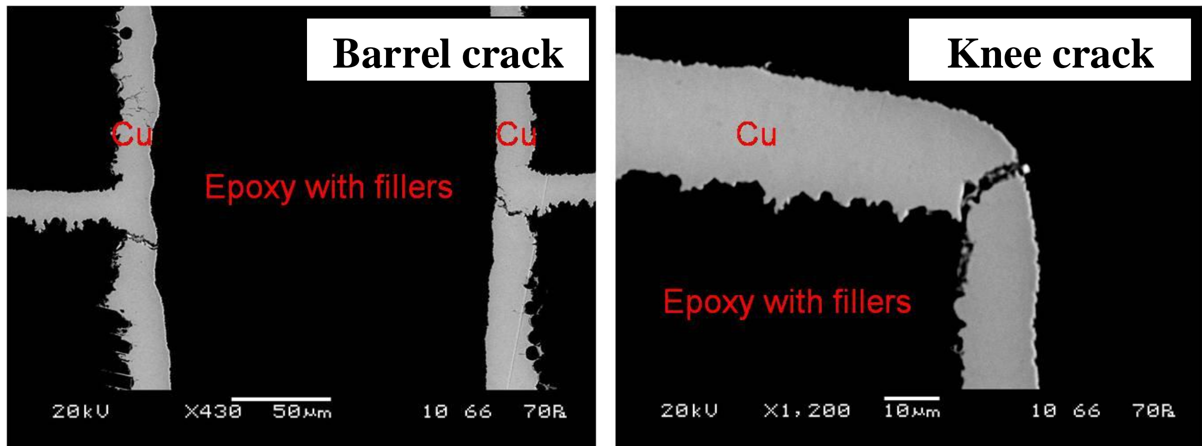

Figure 4-7: SEM analysis on crack opens in the copper barrel hole from Material D

The test coupon has also been etched to observe the microstructures of the copper in the barrel hole. The SEM images are given at Figure 4-8.

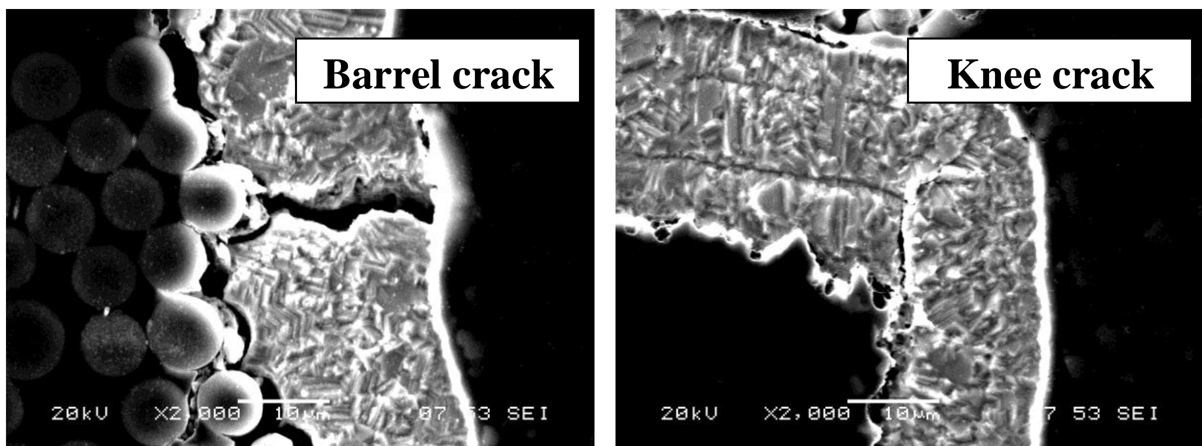

Figure 4-8: SEM analysis on etched copper barrel hole with crack opens from Material D

4.3 Mechanical properties analysis

This section includes experimental data for flexural strength, energy to fracture, flexural modulus, Vickers hardness and copper peel strength. Cross-sectional analysis is also included for fracture surface and indentation from the samples.

4.3.1 Flexural strength

The flexural strength is calculated based on the load to fracture from the three point bend test and also the dimension of the sample. Material G had only one sample available and it was used as reference. The flexural strength data is provided in Table 4-10.

Table 4-10: Flexural strength data for each material

Material	Flexural Strength (MPa)
A	384.2±5.1
B	322.8±6.4
C	396.1±3.4
D	382.5±8.3
E	389.8±11.9
F	353.4±4.1
G	343.5

4.3.2 Energy to fracture

The energy to fracture is dependent on the load to fracture and also the extension of the sample upon fracture. The energy to fracture is calculated using the area under the load-extension curve from the three point bend test. The result data is given in Table 4-11. The fracture surfaces for materials with and without fillers are also examined using the SEM, which is provided in Figure 4-9.

Table 4-11: Energy to fracture data for each material

Material	Energy to Fracture (J)
A	5.6±0.3
B	2.6±0.2
C	3.5±0.1
D	4.6±0.3
E	4.4±0.3
F	3.6±0.2
G	3.5

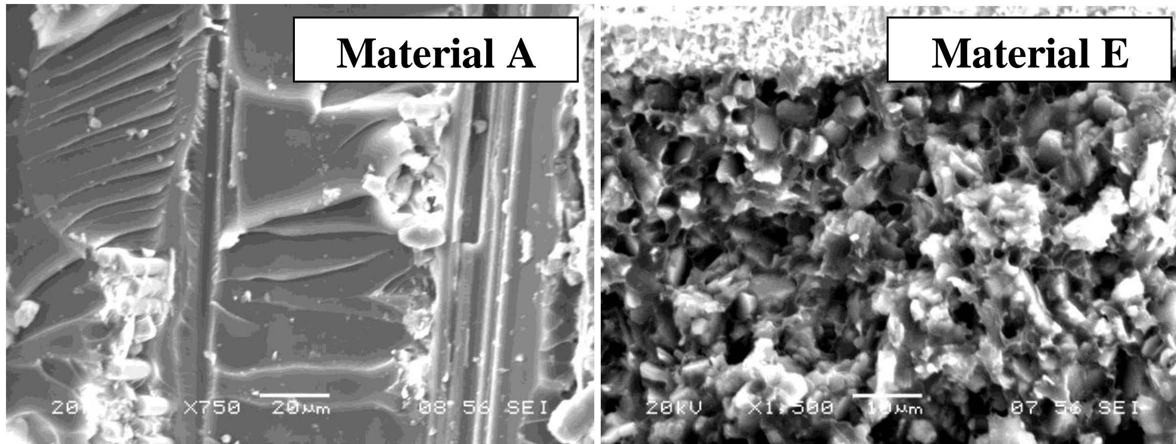

Figure 4-9: Fracture surface for material A (without filler) and material E (with fillers)

4.3.3 Flexural modulus

The flexural modulus is measured using the DMA in dual cantilever mode. The flexural modulus is equivalent to the storage modulus of the composite material, which is also related to the elastic modulus of the epoxy. The result data is provided in Table 4-12.

Table 4-12: Flexural modulus measurements of each material from the DMA

Material	Flexural Modulus (GPa)
A	24.06±0.39
B	27.62±0.93
C	32.01±0.66
D	28.05±1.21
E	29.90±1.77
F	27.19±1.17
G	30.21±0.83

4.3.4 Vickers hardness

The Vickers hardness is measured for each material using the Vickers indenter. It measures the resistance to penetration for the epoxy composite. The indent is on the cross-sectioned epoxy with or without fillers. The result data is listed in Table 4-13.

Table 4-13: Vickers hardness for each material

Material	Vickers Hardness (HV)
A	17.99±0.89
B	22.40±1.35
C	49.76±5.54
D	32.23±1.31
E	28.97±1.31
F	28.06±0.86
G	35.65±2.24

The optical cross-section images of the indents for all materials do not show any indentation cracks. Some sample images are shown as Figure 4-10.

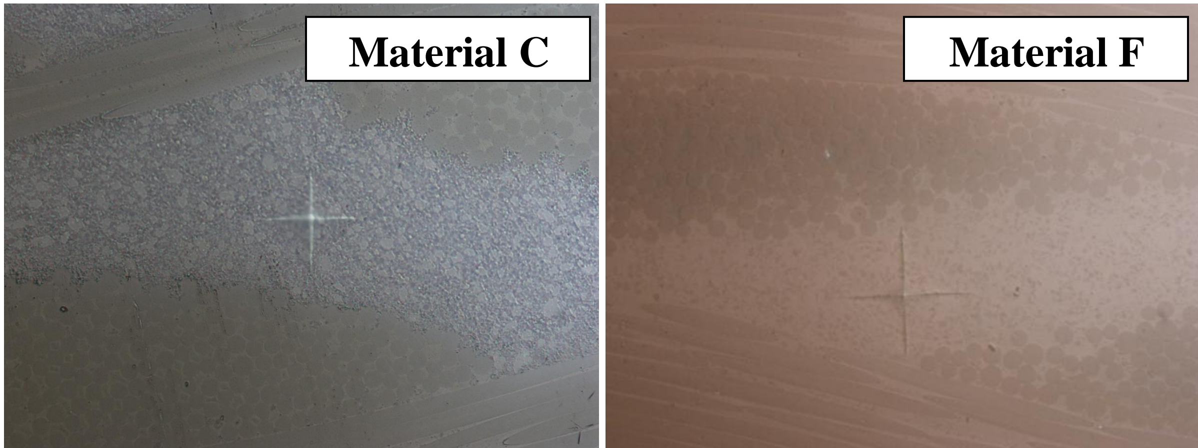

Figure 4-10: Vickers indentation marks on different materials

4.3.5 Copper peel strength

The copper peel strength represents the adhesive strength of the copper onto the epoxy composite substrate. The higher the peel strength, the less susceptible the material is to delamination. The results are listed as Table 4-14.

Table 4-14: Copper peel strength for materials examined

Material	Cu peel strength (N/mm)
A	1.277±0.049
D	0.866±0.189
E	1.114±0.166
G	1.183±0.082

4.4 Electrical properties

The dielectric constant (D_k) and dissipation factor (D_f) at 3.2 GHz were measured instead of at 1MHz as suggested by the IPC methods, because the higher frequency is often that used in handheld devices. Only some of the materials studied have data available for the electrical properties measurements due

to the fact that there are no test coupons for other unlisted materials. The results are listed in Table 4-15.

Table 4-15: Dielectric constant and dissipation factors for each material

Material	D_k (3.2 GHz)	D_f (3.2 GHz)
A	4.06±0.10	10.38±0.52
D	4.63±0.06	10.48±2.96
E	4.44±0.07	8.55±1.67
G	4.51±0.01	11.75±0.02

Chapter 5

Discussion

This section discussed the importance of both the thermal and mechanical properties to manufacturing process, performance and reliability. The correlation between these properties to the fillers and epoxy characteristics are also given.

5.1 Thermal analysis and correlation with fillers and epoxy properties

Thermal properties include glass transition temperature, coefficient of thermal expansion, time to delamination, temperature to decomposition, interconnect stress test results and their correlations to chemical properties are discussed.

5.1.1 Glass transition temperature (T_g)

Glass transition temperature is an important parameter during lead-free soldering. Materials with higher T_g values delay the onset of the increase in expansion after glass transition [44]. This is advantageous to prevent reliability issues such as delamination. However, Cry [45] also show that temperature to decomposition is more important in these issues, which will be discussed in a later section.

5.1.1.1 Comparison between different measuring methods

The T_g values measured by the DSC, TMA and DMA methods for each material are compared and they are given at Figure 5-1. The T_g values for all materials follow this trend: T_g (DMA) > T_g (DSC) > T_g (TMA). This agrees with the simple rule of thumb for laminate qualification and testing for glass transition temperature [27]. The difference in T_g values is due to the fact that they measure different physical changes as the epoxy resin changes from a glassy to a rubbery state.

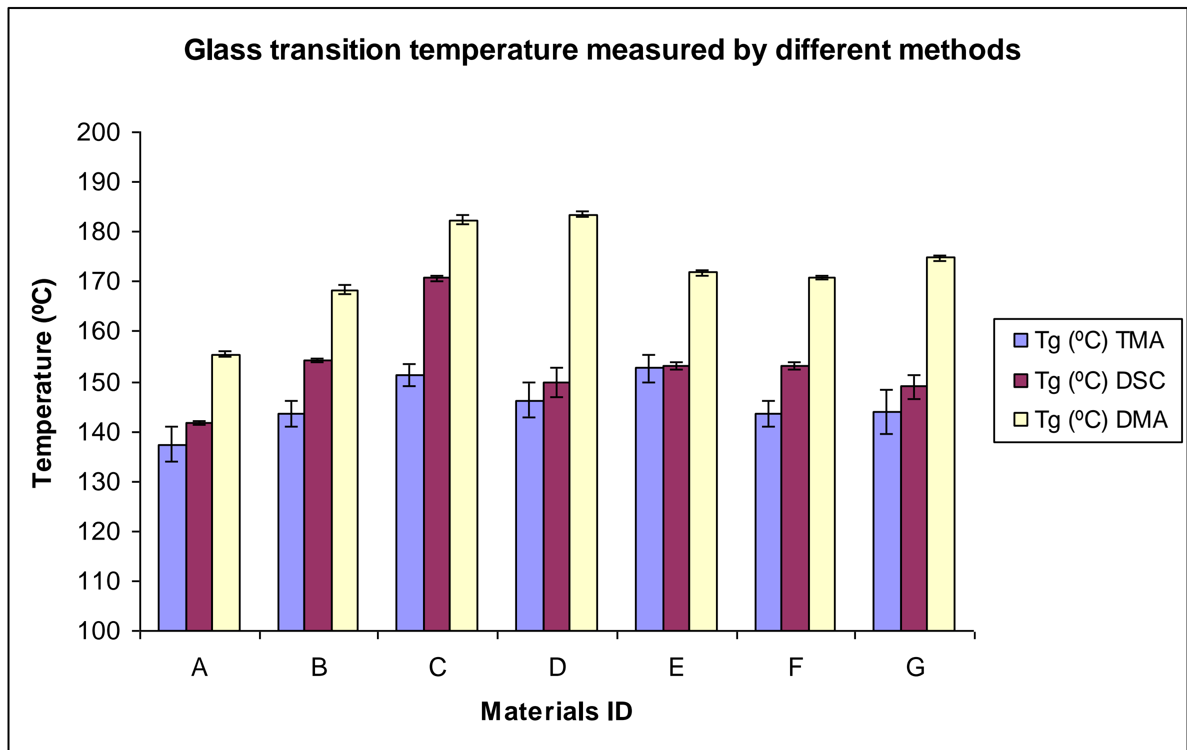

Figure 5-1: Glass transition temperatures for each material

5.1.2 Coefficient of thermal expansion (CTE)

The CTE in the z-axis has a significant impact on the reliability of the printed circuits. The expansion and contraction in the z-axis upon temperature increases and decreases results in applied thermal stress on the plated through hole run through the z-axis [26]. Large z-axis CTE values imply excessive thermal stress and results in plastic deformation not only to the through hole, but also copper pads on the surface. During rework soldering in the assembly process, the thermal cycling can cause copper fatigue which leads to crack initiation and propagation in the copper plated through hole and separation between conductor and barrel hole wall causing electrical failure.

The CTE in the x/y axis is also important as it affects the components attached to the surface of the PWB. The CTE mismatch in the x and y axis for the PWB substrate and components can lead to thermally induced stress and cause separation of the components attached during assembly and rework. It can also impact the interlaminar adhesion and delamination resistance of the PWB [26].

5.1.2.1 Z-axis CTE before T_g and correlation with total filler volume %

The z-axis CTE for the different materials and the correlation to fillers percentage are given in Figure 5-2. As the volume percetange of filler increases, the z-axis CTE (before T_g) decreases linearly except for Material D. This result agrees with the study by Chen [21] that the CTE of a two-phase polymeric composite material exhibits a linear relationship with the filler volume percentage in the matrix according to the simple rule-of-mixture.

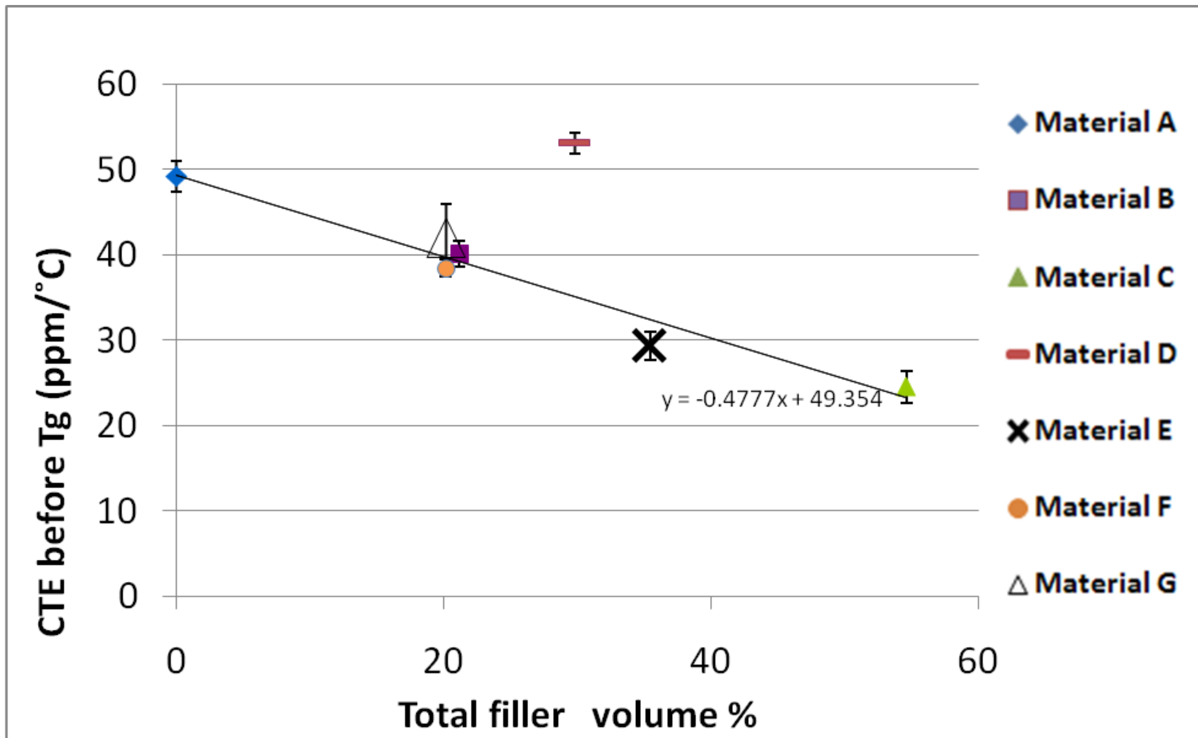

Figure 5-2: Correlation between z-axis CTE before T_g and total filler volume %

5.1.2.2 Z-axis CTE after T_g and correlation with total filler volume%

The same correlation is observed for the z-axis CTE after T_g. It decreases with increasing fillers volume %. The correlation curve for z-axis CTE after T_g has a steeper slope (-1.892) than the curve before T_g (-0.478). The CTE for the epoxy matrix increases more above the glass transition while the silica does not exhibit significant transition at this temperature range (190-250˚C). Thus, the slope increases significantly. The correlation graph is shown in Figure 5-3.

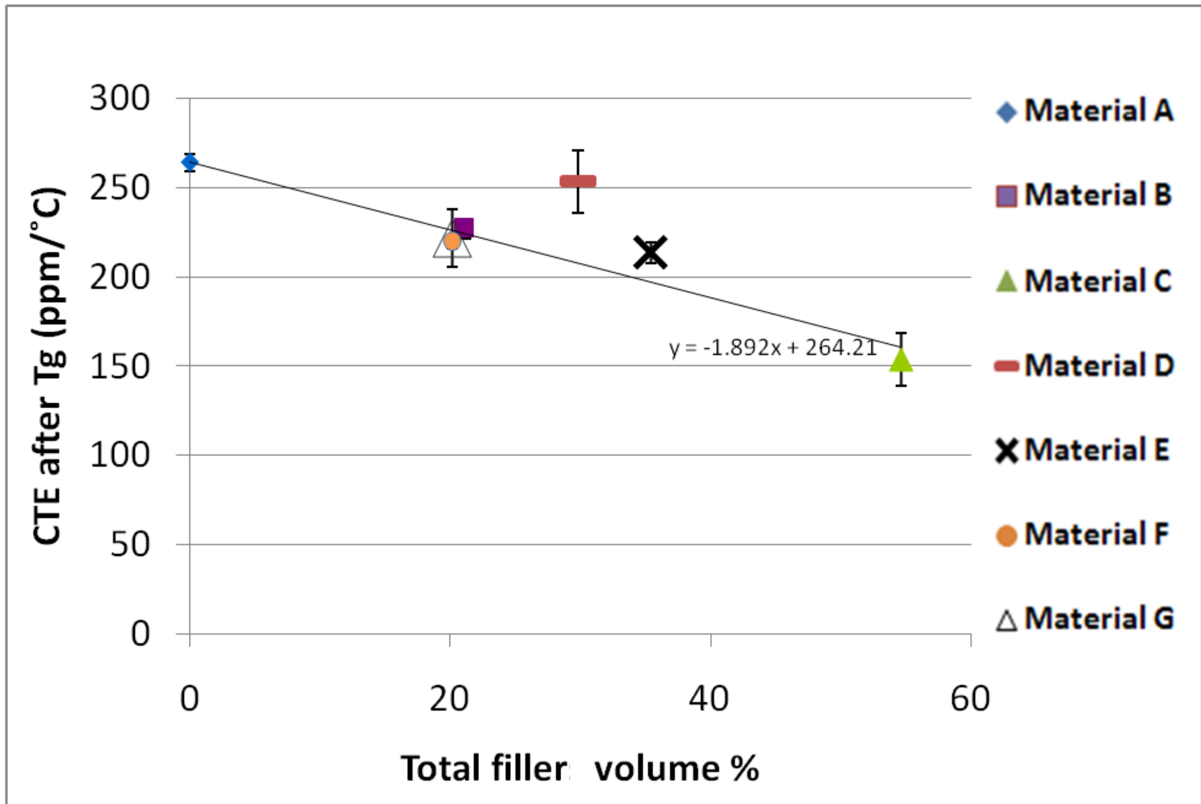

Figure 5-3: Correlation between z-axis CTE after T_g and total filler volume %

5.1.2.3 Z-axis CTE changes and correlation with silica filler volume %

Since silica fillers are thermally stable compared to other fillers, increasing the silica filler loading retards the ΔCTE from the glassy to rubbery state. This can be shown in the correlation between z-axis CTE changes after T_g and the silica fillers volume % in Figure 5-4.

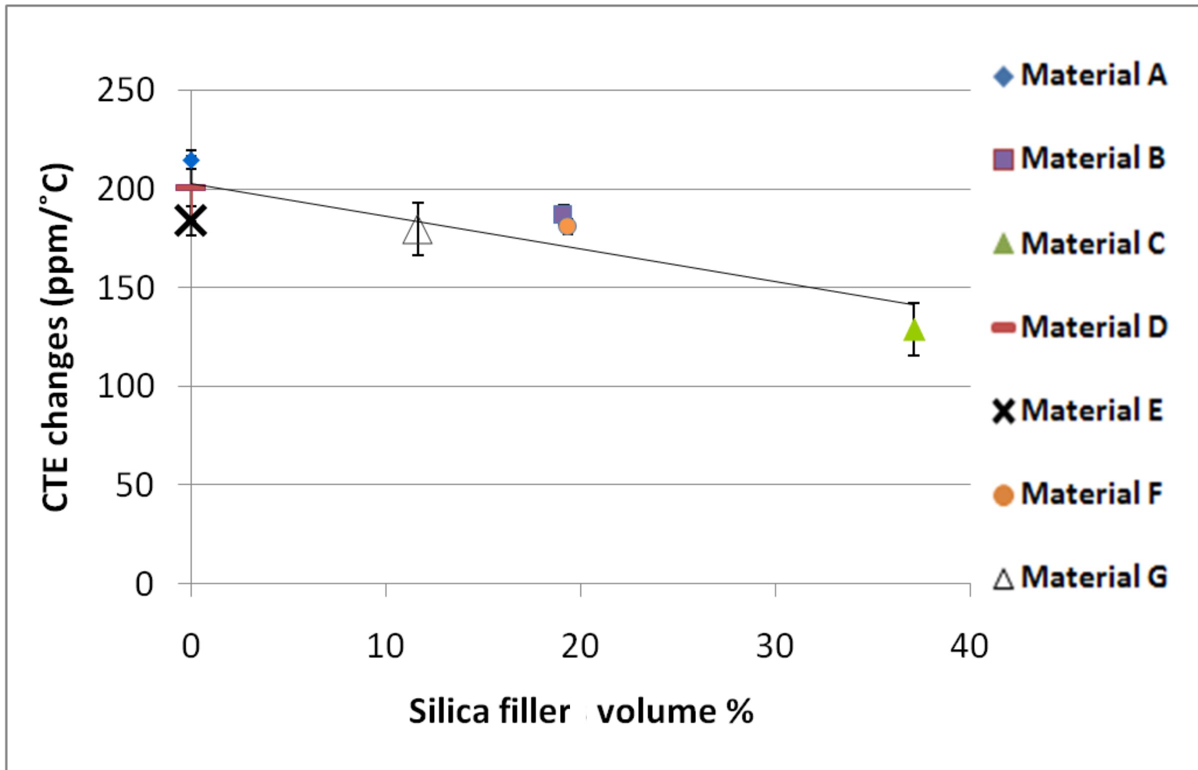

Figure 5-4: Correlation between z-axis CTE change and silica filler volume percentage.

5.1.2.4 Decomposition of $Al(OH)_3$ effects on z-axis CTE

Other fillers such as aluminum hydroxide do not reduce the CTE after the T_g as effectively as silica since it starts to decompose above 200˚C [6], which leads to an increase in CTE for Material D from 228.5 ppm/°C to 397.6 ppm/°C as shown in Figure 5-5.

5.1.2.5 Thermal stability of epoxy effects on z-axis CTE

The short red bars on Figures 5.2 and 5.3 represent Material D which does not follow the CTE trend as the other materials do. It is also found that Material D experiences a significant decrease in storage modulus from room temperature to 150˚C compared to other materials. It is possible that the epoxy is less thermally stable in this low temperature region, which results in a lower storage modulus and higher z-axis CTE as demonstrated in Figure 5-6.

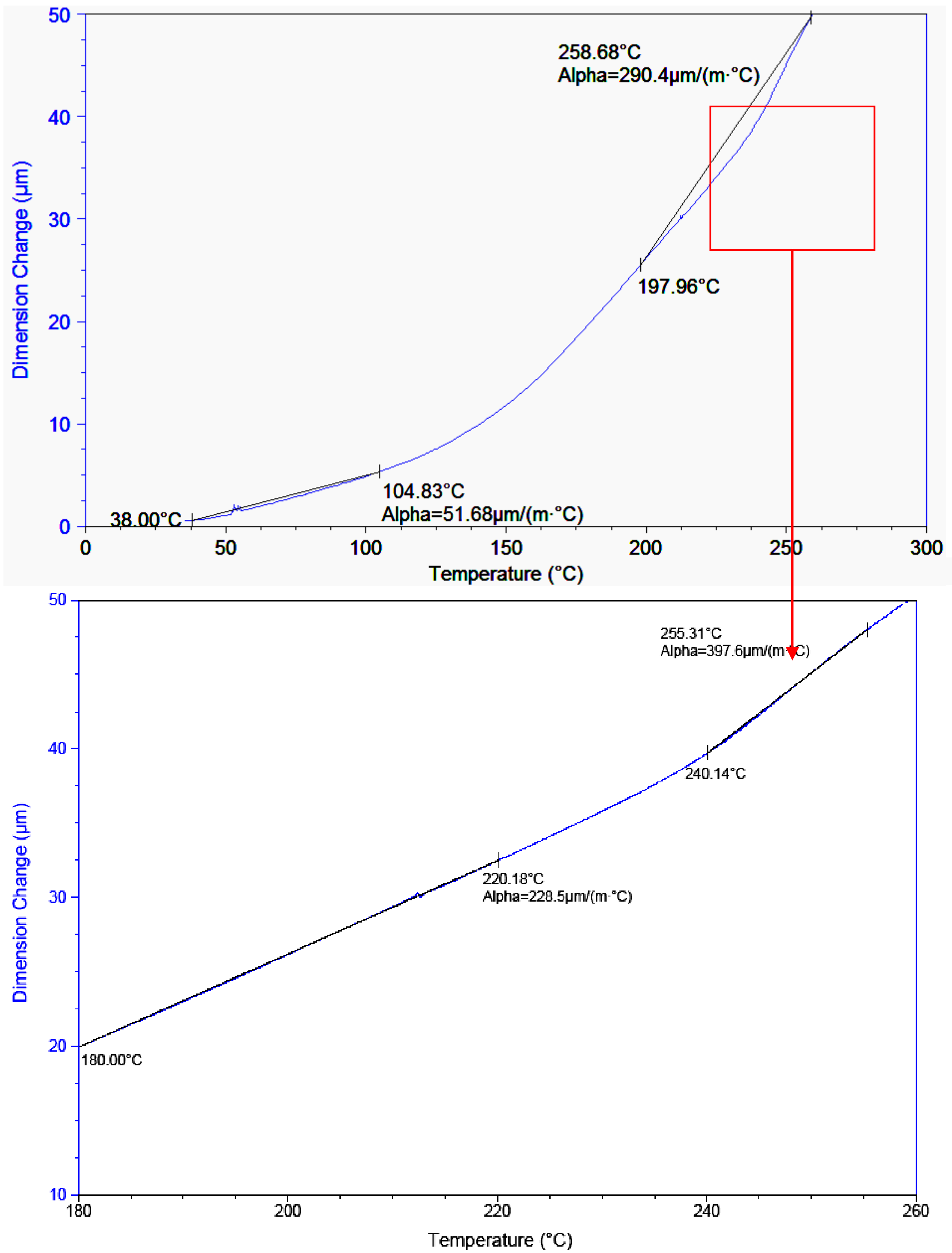

Figure 5-5: Decomposition of alumnium hydroxide in Material D leads to an increase in CTE above 240˚C

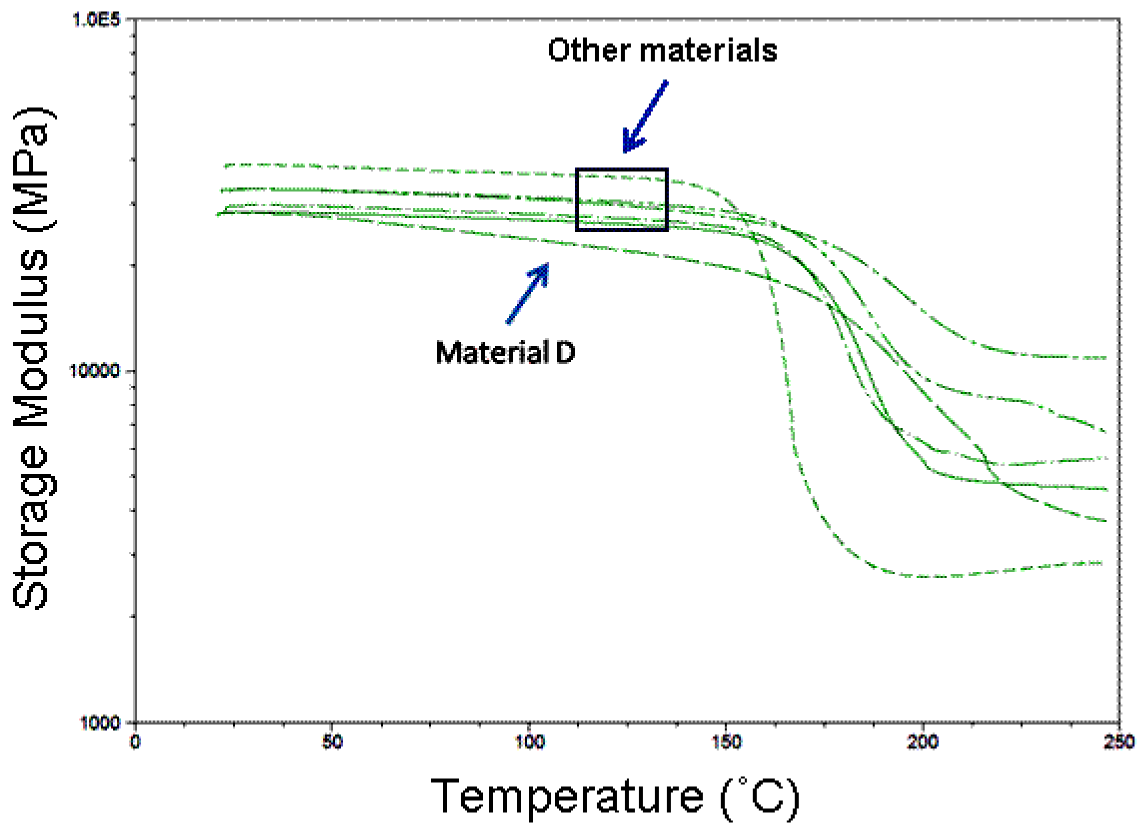

Figure 5-6: Storage modulus cruves for different materials

5.1.2.6 Comparison between Z and X-Y axis CTE

The z-axis CTE is greater than the x-y axis CTE both before and after the glass transition. This is because the glass fiber reinforcements are present in the x-y, but not the z-axis direction. It is observed that the glass fibers significantly reduce the CTE in x and y compared to the z-axis. The comparison between the two different CTEs is given at Figure 5-7 and Figure 5-8. It is known that glass fiber reinforcements have low coefficient of thermal linear expansion [46] and results in significant reduction in linear (x-y) CTE. Also, the z-CTE is significantly higher than the x and y CTE after the glass transition. Therefore, the z-axis CTE should play a more important role in failures due to thermal stress such as delamination and cracks in copper plated through holes.

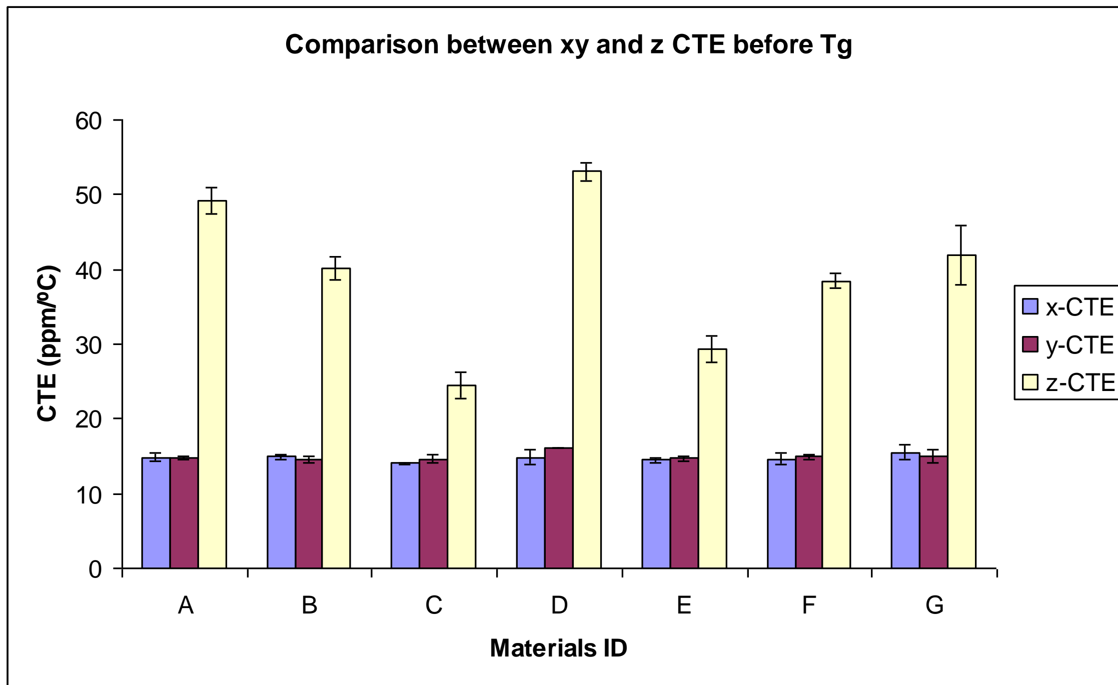

Figure 5-7: Comparing between XY and Z axis CTE before T_g

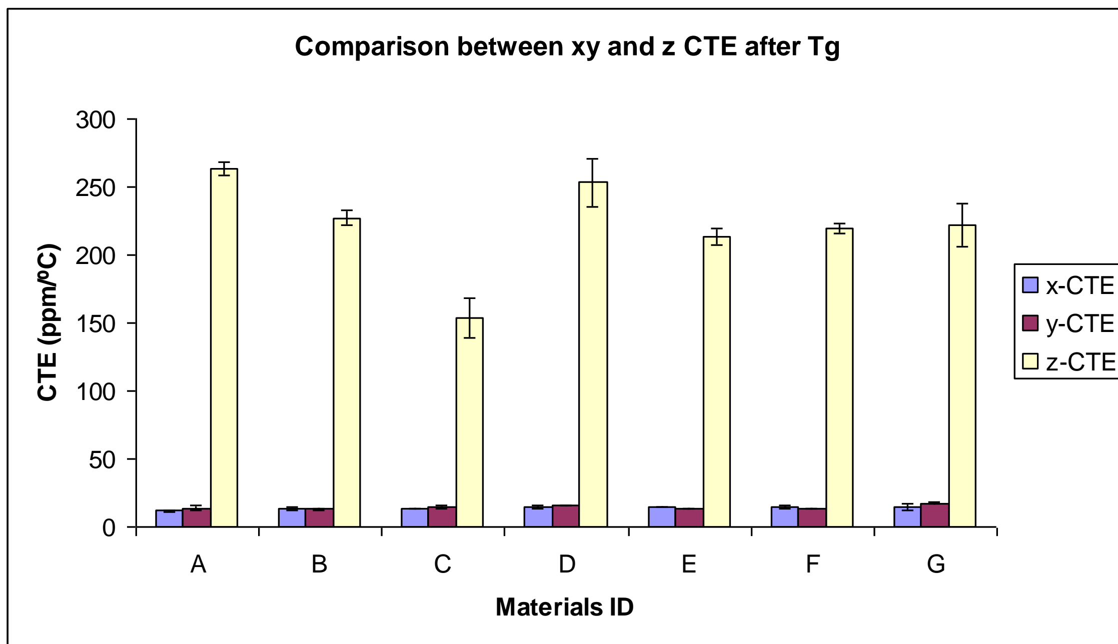

Figure 5-8: Comparing between XY and Z axis CTE after T_g

5.1.3 Time to delamination

Delamination is a failure in composite materials marked by a separation of layers, which is caused by either thermally or mechanically induced stress. Lead-free soldering assembly and rework processes are associated with high temperatures (e.g. T_{max} ~245°C) which can induce thermal stress in the PCB and lead to delamination. The most common test temperatures for delamination are 260ºC (T260) and 288ºC (T288) [44].

5.1.3.1 Correlation between T260 and silica filler %

The addition of fillers prolongs the time to delamination at T260, especially silica, as shown in Figure 5-9 where the time to delamination increases as the silica filler volume increases. Materials without any silica fillers all exhibit short time to delamination. Material F does not follow the correlation curve because it has a significantly long time to delamination, which is due to the high thermal stability of the epoxy and will be discussed.

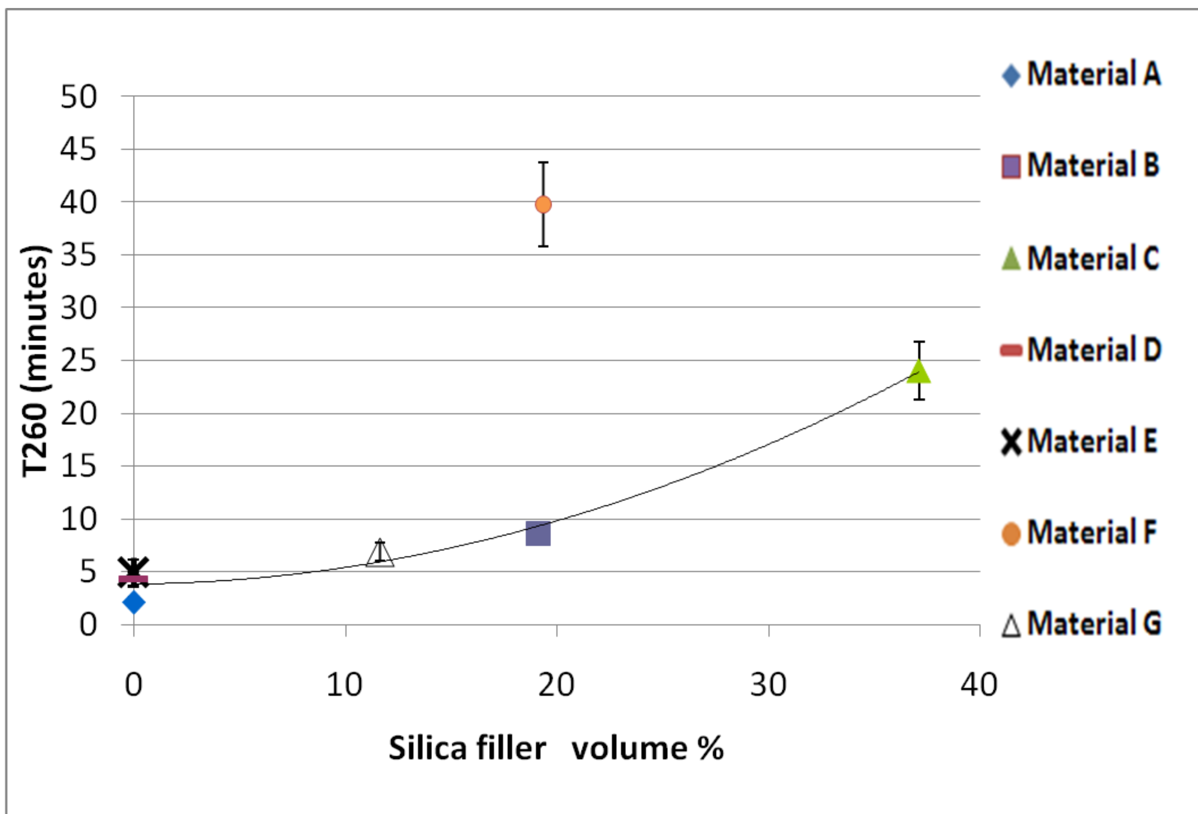

Figure 5-9: Correlation between T_{260} and silica fillers volume %

5.1.3.2 Correlation between T288 and silica filler %

A similar trend is found in the correlation between T288 and silica fillers where the presence of silica prolongs the time to delamination as shown in Figure 5-10. It is also noticed that the time to delamination at 288ºC is much shorter than 260ºC due to the increase in temperature. Materials without silica fillers show poor delamination resistance in that they delaminate before 288ºC. Similarly, Material F exhibits outstanding time to delamination at 288ºC.

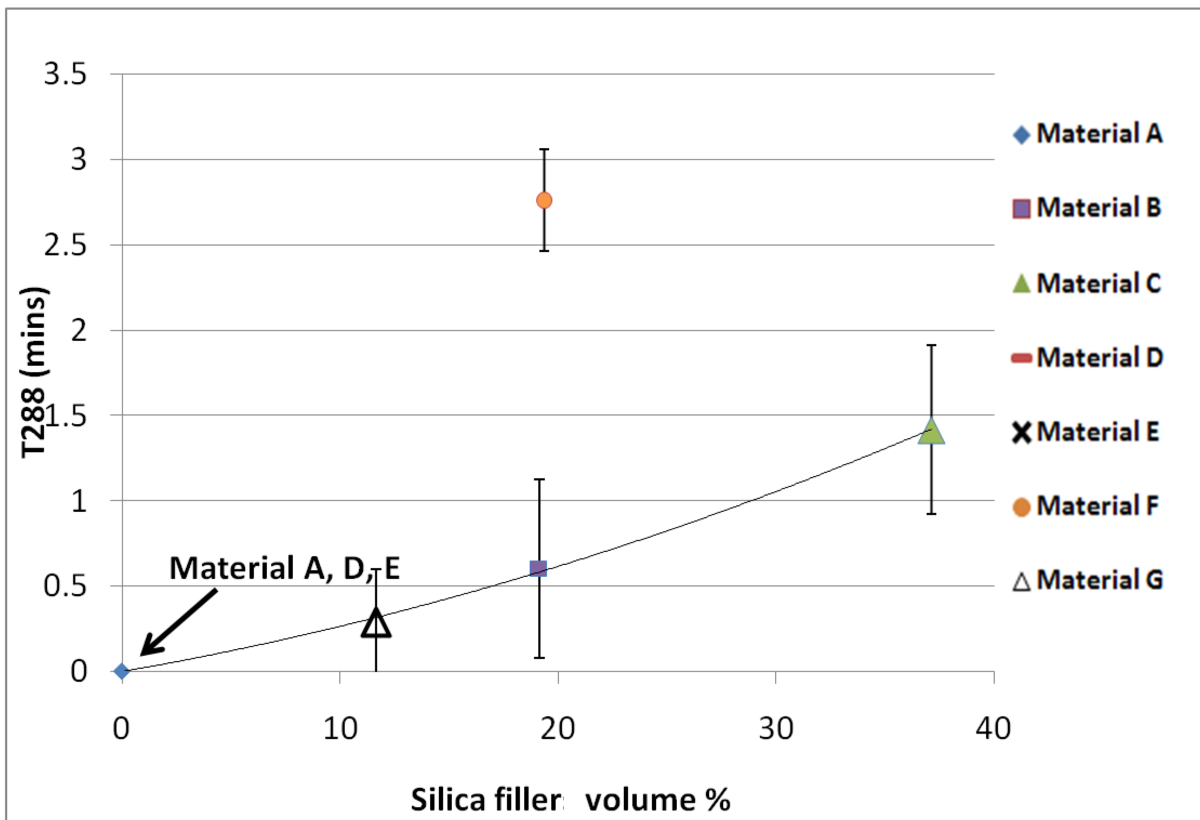

Figure 5-10: Correlation between T288 and silica fillers volume %

5.1.3.3 Relationship between delamination modes and fillers

SEM cross-sectional images of delaminated samples (Figure 4-6) reveal that there are three different failure mechanisms: delamination at the interface between a) copper/epoxy, b) glass fibres/epoxy and c) epoxy/epoxy, which has also been shown by Zequn [47]. Laminates with silica as the major filler experience predominantly the copper/epoxy delamination mode, while others with aluminum

hydroxide fillers delaminate at both the glass/epoxy and epoxy/epoxy interfaces. The summary of the delamination modes and fillers for each material is given at Table 5-1.

Table 5-1: Relationship between delamination modes and majority fillers

Materials	Majority Fillers		Delamination modes		
	SiO_2	$Al(OH)_3$	Copper/Epoxy	Epoxy/Epoxy	Epoxy/Glass
A			X		
B	X		X		
C	X		X		
D		X		X	X
E		X		X	X
F	X		X		
G	X	X	X	X	X

Studies by Wong [15] show that silica has the lowest CTE (0.5 ppm/˚C) of all fillers and is the most effective in reducing the CTE of the composite. Figure 5-3 also demonstrates that silica reduces ΔCTE after T_g. In comparison, the materials with aluminum hydroxide start decomposing by releasing water above 200˚C. The creation and expansion of the water vapour within the epoxy degrades the cohesive strength and promote epoxy/epoxy delamination. Also, the CTE mismatch between the epoxy and the glass fibres lead to interfacial separation [15]. As a result, materials with predominantly silica fillers exhibit a longer time to delamination than aluminum hydroxide fillers, as demonstrated in Figure 5-9 and Figure 5-10.

5.1.3.4 Thermal stability of epoxy effects on delamination

The orange circles on Figure 5-9 and Figure 5-10 represent Material F which does not follow the correlation. It is possible that the epoxy of this material is more thermally stable than the other materials tested resulting in a longer time to delamination. It is also realized that Material F has higher resistance to decomposition compared to other materials, which will be discussed.

5.1.4 Temperature to decomposition (T_d)

The temperature to decomposition is related to the physical degradation of the resin system (with or without fillers) during high temperature reflow. It can affect the long-term reliability for PCBs if delamination occurs during assembly and rework [44].

5.1.4.1 Derivative weight changes vs. Aluminum hydroxides filler volume %

The derivative of the weight change during decomposition (Figure 5-11) reveals that there is a noticeable weight loss for materials with the presence of aluminum hydroxide since its decomposition range is between 200˚C and 350˚C [3]. As the aluminum hydroxide fillers percentage increases, the materials decomposition at 260˚C becomes more rapid. The decomposition of the aluminum hydroxide into water vapour and aluminum oxide lead to the decreases in weight by the vaporization of the water.

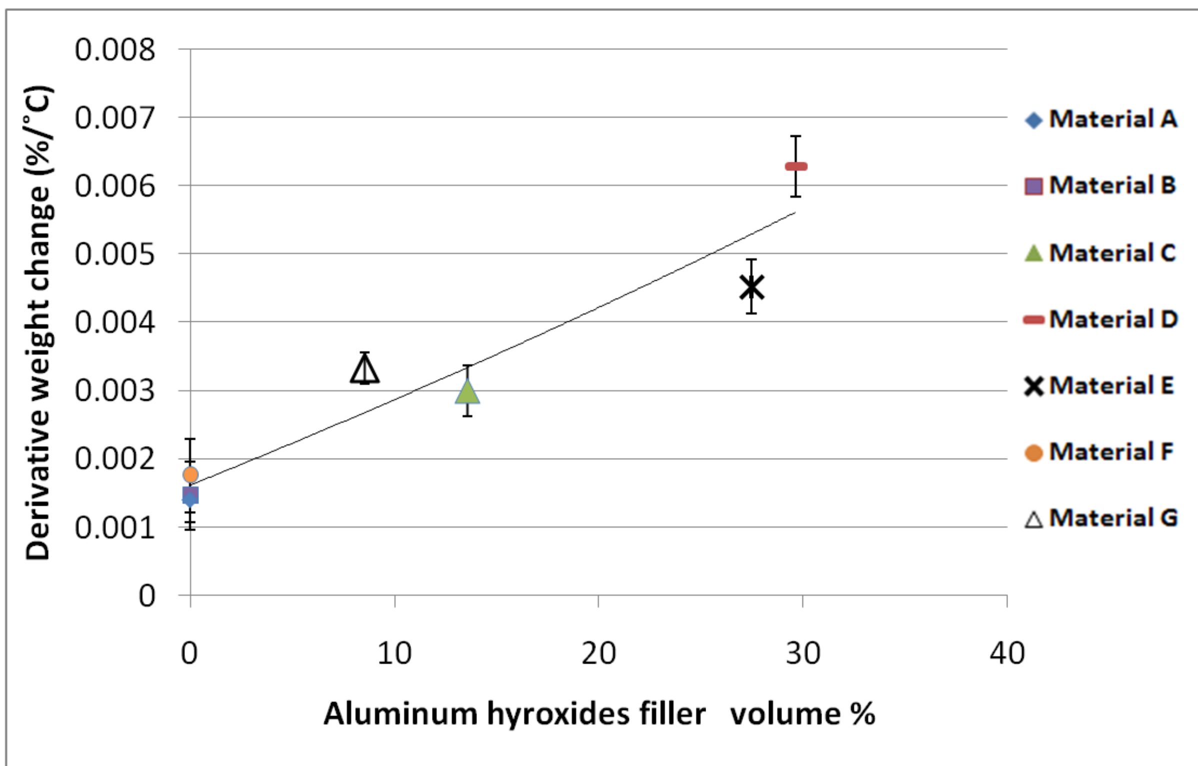

Figure 5-11: Correlation between aluminum hydroxide and derivative weight change at 260˚C

5.1.4.2 Temperature to decomposition at 1, 2 and 5 weight loss%

Above 300°C, the decomposition of the epoxy becomes more significant. At the 5 % weight loss, halogen-free materials (Materials D-G) exhibit higher temperatures to decomposition than the

halogenated materials (Materials A-C) as shown in Figure 5-12. It is possible that the epoxy backbone in the halogen-free materials have higher thermal stability at high temperature. Even though Jeng and Wang [7, 48] show that phosphorus-containing backbones would reduce thermal stability of the resulted epoxy polymers, Liu [18] explains that the degradation rates of the phosphorus-containing resin is slower than the phosphorus-free resin at high temperature region. This is because the phosphorus groups decompose to phosphorus-rich residue forming a thermally stable layer upon heating. Also, aromatic compounds such as DOPO are commonly used in halogen-free materials [6] to increase flame retardancy and they are beneficial to the thermal stability [49].

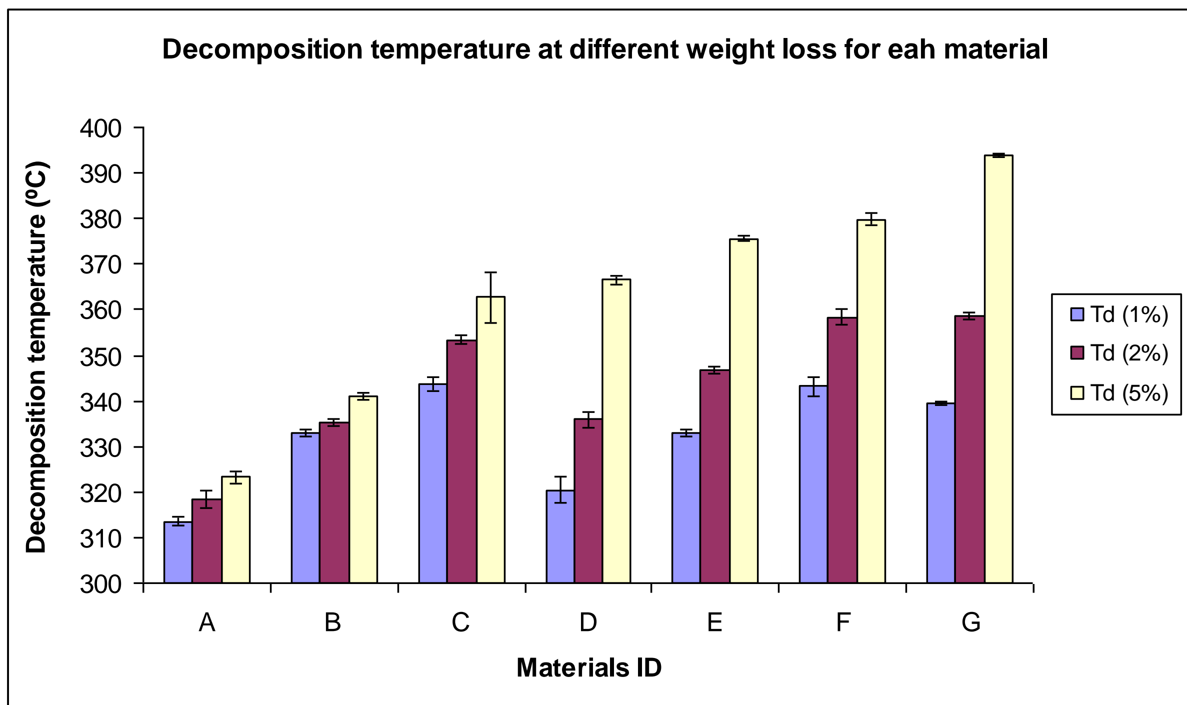

Figure 5-12: Decomposition temperature at different weight loss (1, 2 and 5%) for each material

5.1.4.3 Correlation between T260 and T_d at 1 weight % loss

The temperature to decomposition at 1 weight % loss shows a good correlation with time to delamination at 260˚C (Figure 5-13). This indicates that the thermal stability of the epoxy with or without fillers contribute to delamination. As the materials are more resistant to epoxy degradation at this specific temperature, they have a longer time to delamination. This correlation explains why the

time to delamination is not only dependent on the silica fillers percentage, but also the thermal stability of the epoxy as previously discussed.

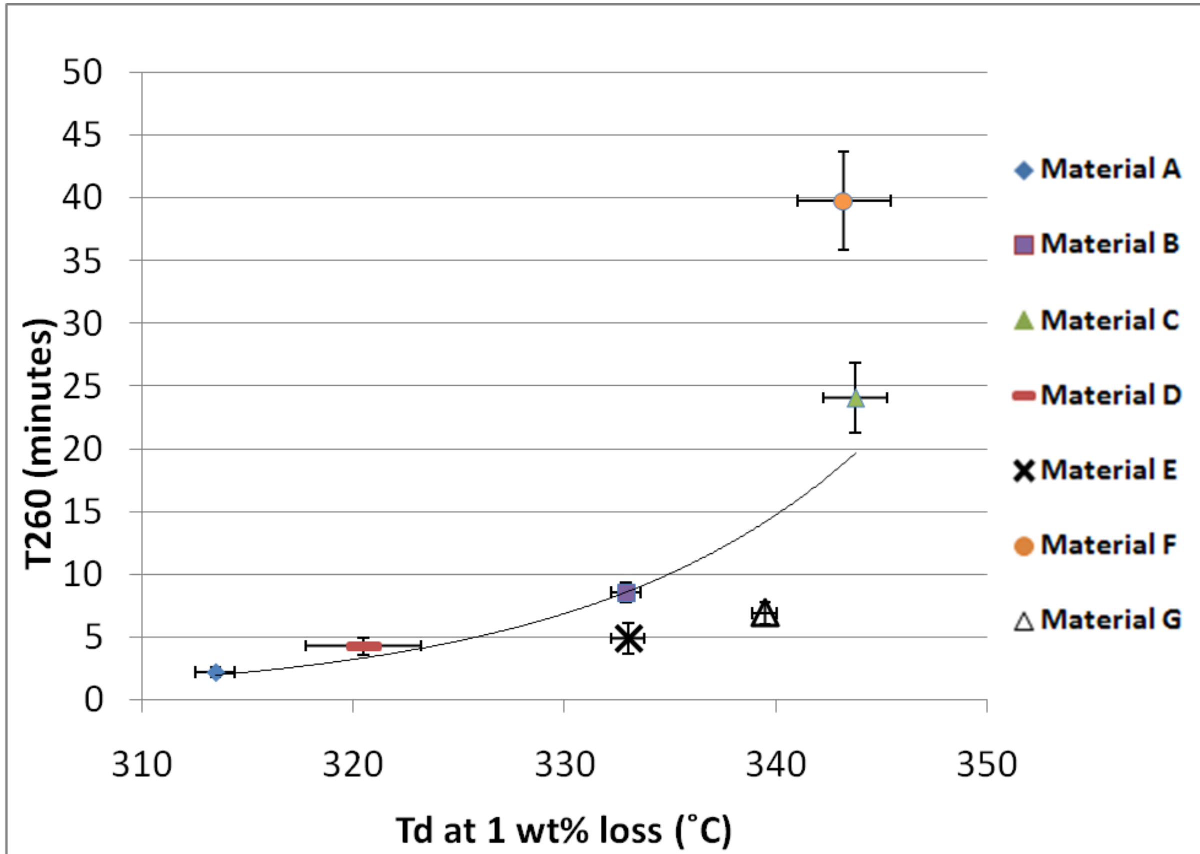

Figure 5-13: Correlation between T_{260} and T_d at 1 weight % loss

5.1.5 Interconnect stress test (IST)

IST testing is used to measure the plated through via and interconnect reliability in PCBs related to the thermal stress temperature [50]. It also measures the impact of lead-free assembly, thermal cycles during rework and predicting the consumption of the PTH life during assembly and manufacturing [51, 52]. The IST testing collects cycles to failure results, which are related to the thermal reliability for specific laminates [53].

5.1.5.1 Crack characterization

Most cracks found in the IST test coupons after failure are barrel cracks, not knee cracks. No post interconnect separation is observed. However, all knee cracks show similar results that the crack path changes as it propagates as shown in Figure 5-14. The SEM images of the etched samples show that

the copper plating might be the reason for this path changes. The PWB fabricator uses multiple plating steps to form the copper circuitry. When the crack propagates into one of the plating lines as shown in Figure 5-14 b), it changes the crack propagation direction.

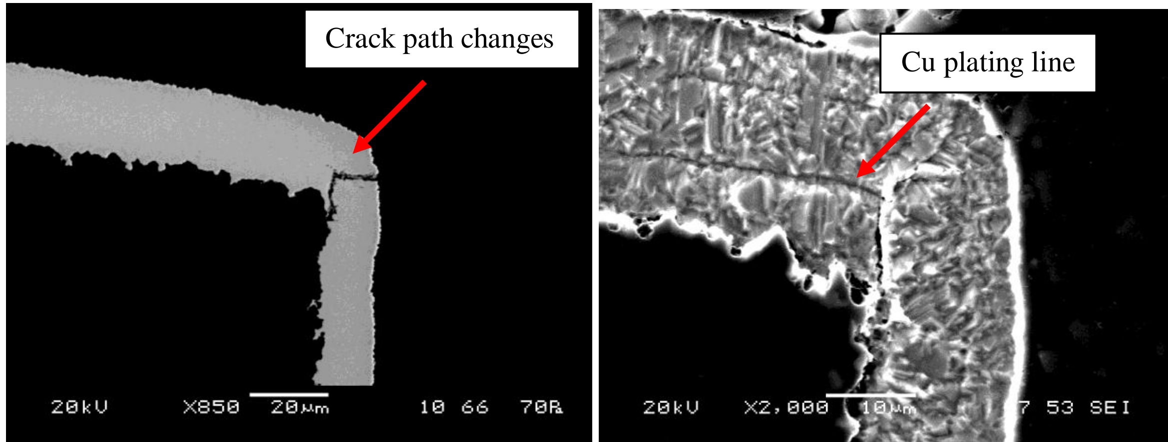

a) Copper without etched b) Etched copper

Figure 5-14: Knee cracks propagation in copper with and without etching

5.1.5.2 Correlation between IST cycles to failure and temperature to decomposition

The temperature to decomposition can be correlated to the IST results. As the material exhibits higher resistance to decomposition, the longer it survives through the IST thermal cycles as shown in Figure 5-15. The temperature to decomposition is related to thermal reliability issue as previously discussed, where IST test indicates plated through via and interconnect reliability in PCB related to thermal stress temperature. Both of them measure the reliability of the PCB materials subjected to thermal stress. Moreover, Liu [54] demonstrates that epoxy resin with high thermal resistance exhibits good IST performance. As a result, the correlation is observed for these data.

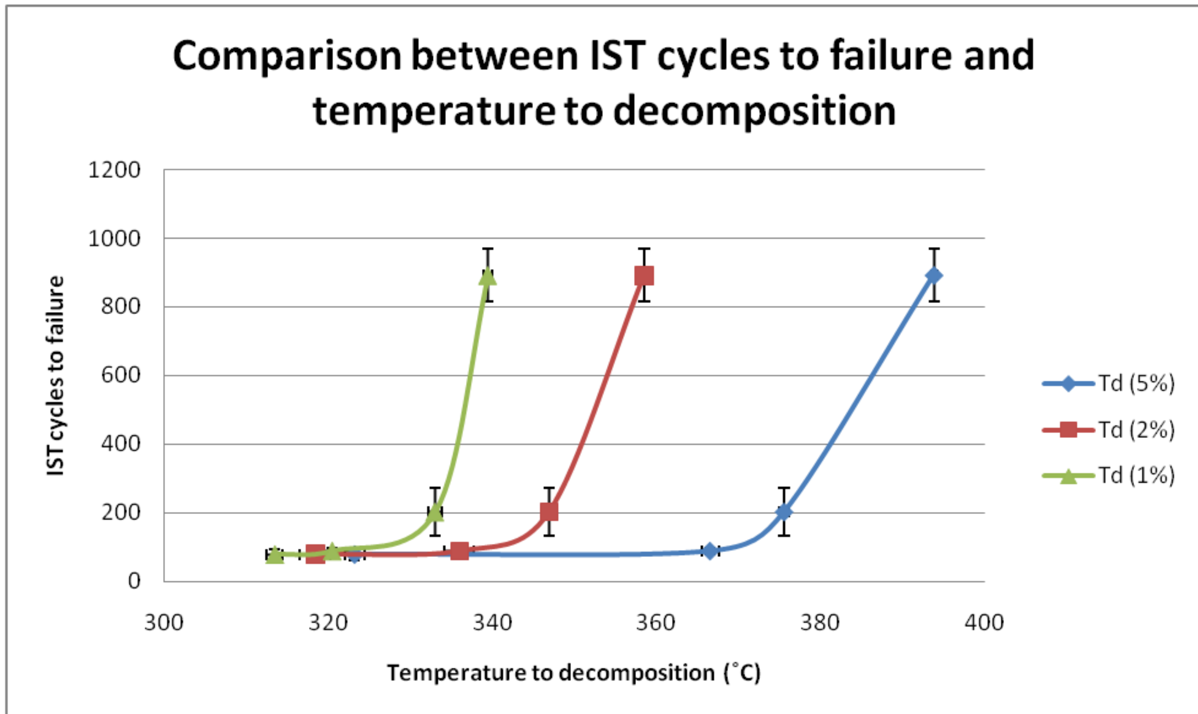

Figure 5-15: Correlation between IST performance and temperature to decomposition

5.2 Mechanical analysis and correlation with fillers properties

In this section, mechanical properties including flexural strength, energy to fracture, flexural modulus, Vickers hardness, and copper peel strength are discussed. The correlation of these properties to the fillers and epoxy characteristics are also included.

5.2.1 Flexural strength

The PCBs in handheld electronic devices are frequently exposed to different forms of mechanical stresses such as bending during assembly. The PCB with poor mechanical strength will cause mechanical damage to both the copper and dielectric material, leading to circuitry malfunction. Therefore, the flexural strength properties of the laminates are important especially for very thin laminates, which are susceptible to damage inside conveyorized equipment during assembly [55].

5.2.1.1 Fracture surface analysis

The fracture surfaces for laminates with and without fillers are different in deformation behaviour. Laminates without fillers experience significant epoxy deformation while laminates with fillers have predominantly filler detachments from the epoxy matrix. This deformation behaviour can affect both

the flexural strength and energy to fracture properties. The fracture surface images are given in Figure 5-16.

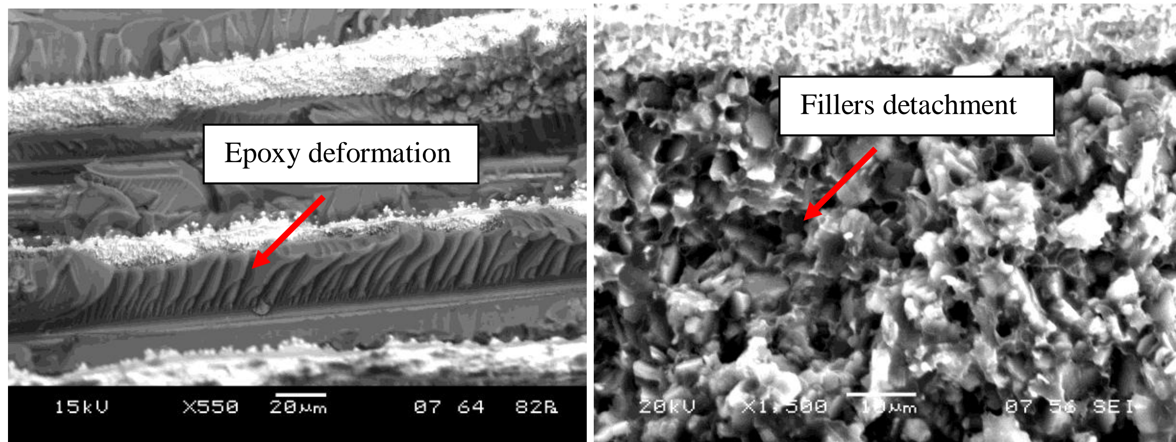

a) Material A b) Material E

Figure 5-16: Fracture surface analysis using SEM for materials with and without fillers

5.2.1.2 Flexural strength and filler loading correlation

Adams [11] explains that the tensile strength of a polymeric composite depends on the filler loading and the types of fillers. If the fillers are well bonded to the polymer matrix, the load is distributed evenly amongst the matrix and the tensile strength will not be decreased. Ramazani [12] also shows that filler compatibility with the matrix transfers stress from the matrix to the filler completely and increases the overall tensile strength. In this study, the flexural strength of each material is compared to the filler loading and is shown in Figure 5-17. It is observed that materials B, F and G have lower flexural strength than material A without fillers. For materials C, D and E, their flexural strengths are slightly higher than material A. Materials B, F and G have silica as the major fillers while materials C, D and E have aluminum hydroxide as the major fillers. This indicates that these metal hydroxides are relatively compatible with the epoxy matrix [12]. In comparison, silica fillers might not bonded as well to the epoxy and slightly decreases the overall flexural strength as shown in Figure 5-18. It is interesting to note that material C with highest amount of silica filler does not exhibit a reduction in flexural strength. Vollenberg [11] demonstrates that small fillers (3-5μm) at high loadings (>25%) dissipate stress during deformation. This might be the explanation for the increase in flexural strength since the fillers used in this study are less than 5 μm.

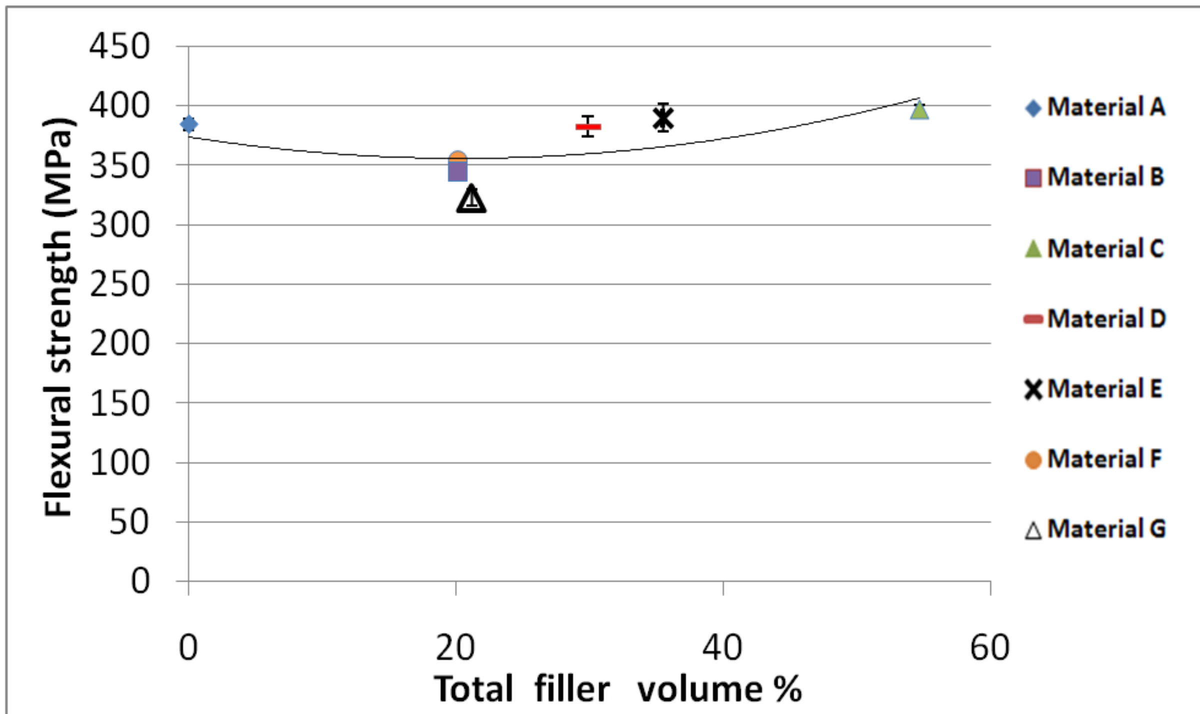

Figure 5-17: Flexural strength as a function of total filler loading

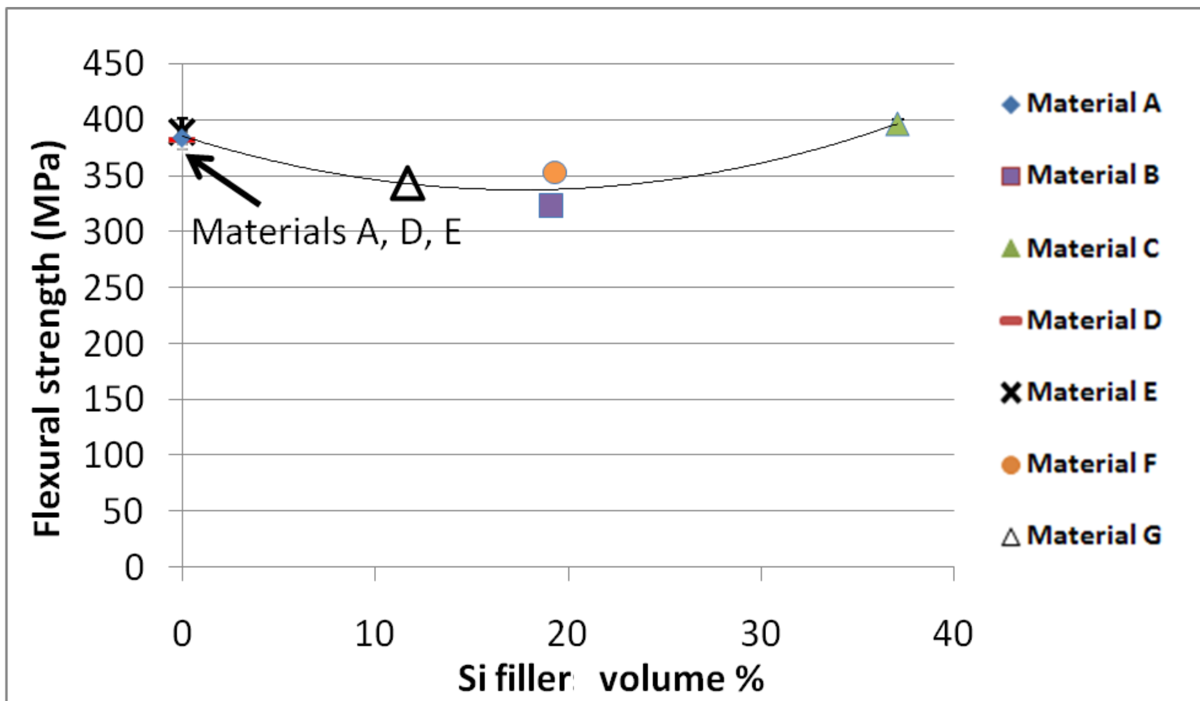

Figure 5-18: Flexural strength as a function of silica filler loading

5.2.2 Energy to fracture

Energy to fracture is calculated from the area under the stress –strain curve and related to the toughness properties. Generally, the tougher the material the higher the impact force it can withstand for polymeric materials, which is an important parameter for handheld device as they are frequently dropped.

5.2.2.1 Energy to fracture and silica fillers loading correlation

As Figure 5-19 shown, material A without any filler has the highest toughness. According to the fracture surface analysis, material A experiences significant amounts of epoxy deformation, which is not observed by other materials. This can be a possible reason for good toughness properties. Addition of fillers such as silica significantly decreases the toughness. This is due to the fact that each particle is a site of stress concentration which leads to micro-crack initiation upon stress [56]. This effect is amplified for particles in the matrix with poor compatibility. As previously mentioned, silica fillers seem to have poor bonding to the epoxy compared to other fillers. Therefore, materials with high silica filler loading exhibit low toughness.

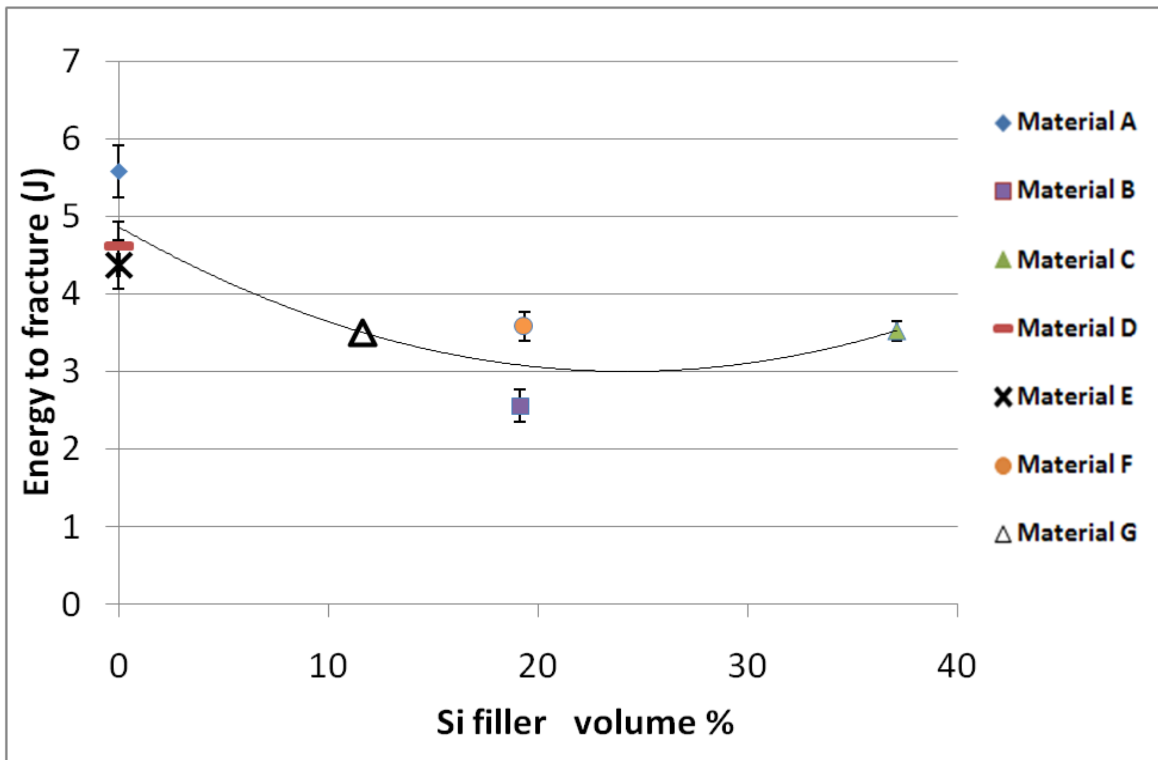

Figure 5-19: Relationship between energy to fracture and silica fillers loading

5.2.3 Flexural modulus

Flexural modulus is an indicator for the stiffness of a composite material and it is important for modeling the stress of the electronic packages during assembly [27]. Different studies [11, 12] demonstrate that stiff composite materials have low impact strength, which can cause mechanical damage to the PCB during assembly and/or usage especially for handheld device.

5.2.3.1 Correlation between flexural modulus and filler loading

Additions of different types of fillers such as silica, aluminum and magnesium hydroxides to a polymeric matrix have been shown by studies [15, 57] that the modulus of the composite is increased linearly according to the filler loading. The same correlation is found in this study and it is given in Figure 5-20.

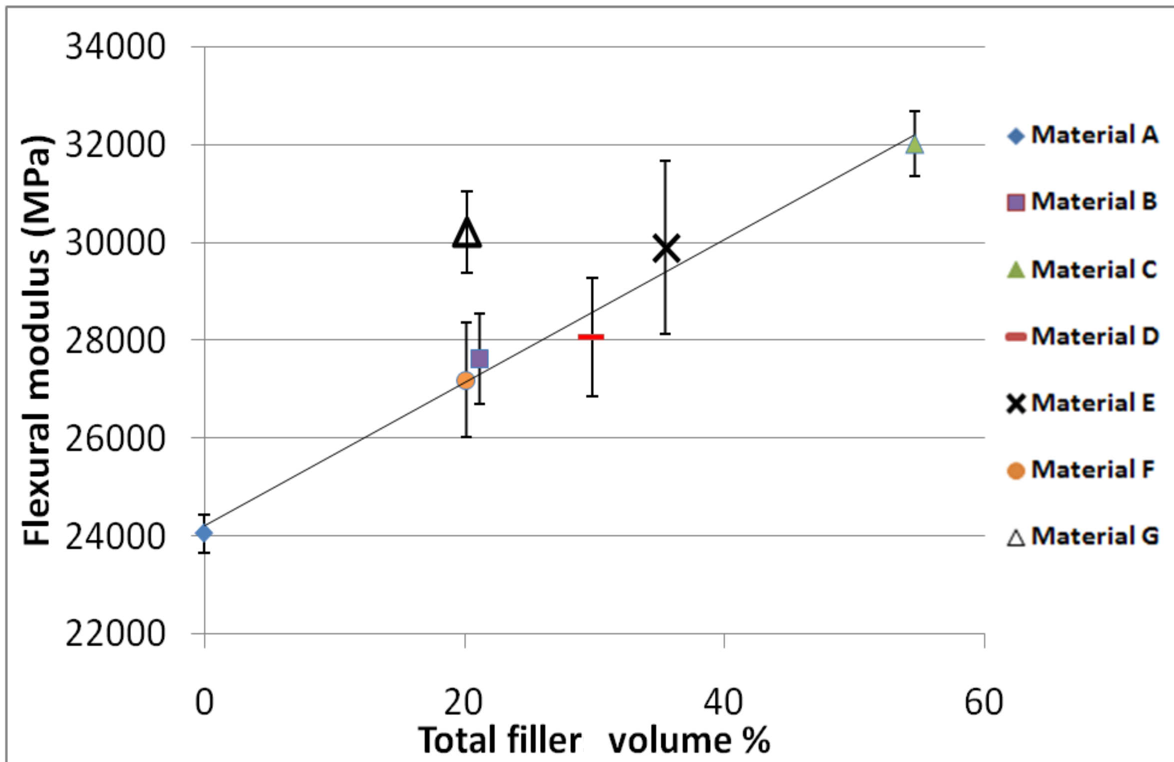

Figure 5-20: Flexural modulus as a function of fillers loading in volume percentage

Similar to the CTE results, the flexural modulus is increased as the filler loading increases regardless of the types of filler used in the materials. Materials with high amount of aluminum hydroxides loading (C, D, and E) also have relatively high flexural modulus. A possible explanation is that the fillers exhibit a good interfacial adhesion to the epoxy matrix as previously mentioned and this results

in a higher modulus of elasticity [15]. Material G does not follow the correlation because its copper thickness in the HDI layers is higher than other materials, which results in an increase in flexural modulus [58].

5.2.4 Vickers hardness

It is well known that hard fillers such as silica reduce PCB drillability by drill bit wearing [59]. Highly cross-linked epoxy also leads to an increase in hardness and causes drill bit damage [60]. Therefore, the hardness of the epoxy with or without fillers is a good indicator for PCB drillability.

5.2.4.1 Correlation between Vickers hardness and filler loading

Vickers hardness is also dependent on the filler loading and both silica and hydroxide fillers enhance the hardness of the epoxy. The relationship between hardness and filler loading is given at Figure 5-21. The cross-section analysis of the Vickers indent indicates that there is no indentation crack. This might be due to the fact that the critical load for epoxies is approximately 1.0-1.5 kN, which is far beyond the load applied (490.3mN) by the microhardness tester [61].

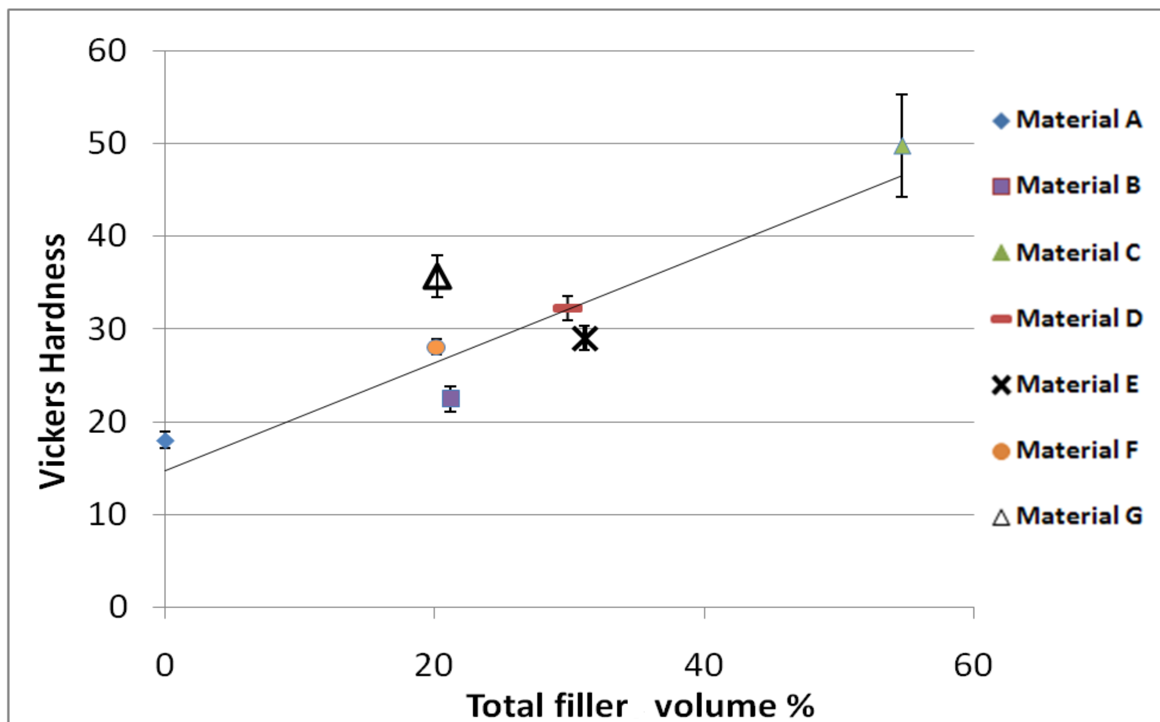

Figure 5-21: Relationship between filler loading and Vickers hardness

Since Material G is cured using a phenolic compound while most of the others are dicyandiamide (dicy) cured, its cross-linking density can be different and exhibit higher Vickers hardness on top of the filler loading. Therefore, not only the filler loading but also the epoxy chemistry can affect the hardness properties.

5.2.5 Copper peel strength

The halogen-free materials are reported in the literature to have reduced adhesion of copper due to the decrease in the number of functional groups in the halogen-free epoxy matrix and also its high chemical resistance [62]. Similar results are shown in this study where the traditional material A has the highest copper peel strength as compared to materials D, E and G which are the halogen-free laminates. The result is given at Figure 5-22.

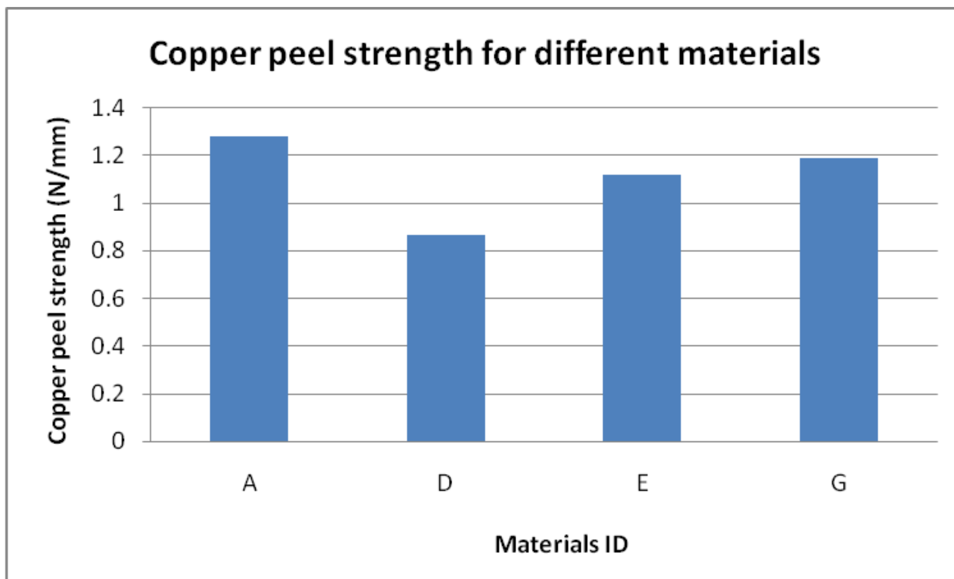

Figure 5-22: Copper peel strength of different materials

5.3 Summary

The aluminum hydroxide filler used in the halogen-free laminates is found to reduce the CTE in z-axis before T_g but is not as effective for CTE after T_g due to its decomposition which lead to an significant increase in the CTE. Silica is found to be more effective in reducing the CTE both before and after T_g due to its thermal stability. Silica also prolongs the time to delamination at both 260 and 288˚C. The temperature to decomposition at 1 wt% loss also correlates to the T260 results where the

thermal stability of the epoxy not only affects the delamination performance, but also other thermal properties such as CTE and IST performance.

Adding fillers in the laminates increase both the flexural modulus and Vickers hardness. However, addition of silica leads to a decrease in energy to fracture and flexural strength for some materials, which increases the brittleness of the substrate materials. Halogen-free materials are also found to have lower copper strength than traditional FR-4 material.

Chapter 6

CONCLUSION

6.1 Materials evaluation based on thermal properties

Table 6-1 indicates the thermal performance properties. Materials A and D are found to have very poor thermal performance properties. Both materials B and E are in the moderate level where materials C, F, and G have very good thermal properties. The numbers in the cells represent the thermal properties ranking 0 to 4 (from worst to best). IST performance is excluded from the ranking because the data are incomplete.

Table 6-1: Table summary of the thermal properties for all materials

Materials ID	CTE in z-axis	T260 and T288	T_d	IST
A	High (1)	Short (1)	Low (1)	Short
B	Medium(2)	Medium (2)	Medium (2)	N/A
C	Very low (4)	Long (3)	Medium (2)	N/A
D	High (1)	Short (1)	Medium (2)	Short
E	Low (3)	Medium (2)	High (3)	Medium
F	Medium (2)	Very long (4)	High (3)	N/A
G	Medium (2)	Medium (2)	High (3)	Long

6.2 Materials evaluation based on mechanical properties

The mechanical performance properties are given in Table 6-2. It is found that materials C and G have very poor mechanical properties. Both materials B and F are in the moderate level where materials A and E have very good mechanical properties. The numbers in the cells represent the mechanical properties ranking 0 to 4 (from worst to best). Copper peel strength is excluded from the ranking because the data are incomplete.

Table 6-2: Table summary of the mechanical properties of all materials

Materials ID	Flexural strength	Energy to fracture	Flexural modulus	Vickers hardness	Copper peel strength
A	Medium (2)	High (3)	Low (3)	Very low (4)	High
B	Low (1)	Very Low (0)	Medium (2)	Low (3)	N/A
C	High (3)	Low (1)	Very high (0)	Very high (0)	N/A
D	High (3)	Medium (2)	Medium (2)	Medium (2)	Low
E	High (3)	Medium (2)	High (1)	Medium (2)	Medium
F	Low (1)	Low (1)	Medium (2)	Medium (2)	N/A
G	Low (1)	Low (1)	High (1)	High (1)	Medium

6.3 Materials ranking based on both thermal and mechanical properties

For handheld electronic application, both thermal and mechanical properties are important to the manufacturing and performance requirements. Thermal properties such as CTE, time to delamination, and temperature to decomposition are significant in that multiple reflow soldering is required for surface mount and rework. Mechanical properties such as energy to fracture are important since handheld devices are frequently dropped. However, others properties such as flexural strength, flexural modulus, and Vickers hardness are not as important, because they are related to the mechanical assembly which does not induce stress as frequently as the reflow soldering process. Therefore, an "importance factor" is assigned for each property to indicate the significance to handheld application and it is given in the ( ) below each property in Table 6-3. The importance factor is multiplied by the numeric ranking given in Table 6-1 and Table 6-2 to reflect a final materials ranking. The values given in the overall column in Table 6-3 are the summation of rankings from all properties. The result shows that material E has the best overall ranking followed closely by material F and makes it a good candidate use in the handheld device.

Table 6-3: Table summary of the overall ranking for each material

Materials ID	CTE in z-axis (2.0)	T260 and T288 (2.0)	T_d (2.0)	Flexural strength (1.0)	Energy to fracture (2.0)	Flexural modulus (1.0)	Vickers hardness (1.0)	Overall
A	2	2	2	2	6	3	4	**21**
B	4	4	4	1	0	2	3	**18**
C	8	6	4	3	2	0	0	**23**
D	2	2	4	3	4	2	2	**19**
E	6	4	6	3	4	1	2	**26**
F	4	8	6	1	2	2	2	**25**
G	4	4	6	1	2	1	1	**19**

6.4 Materials optimization for both thermal and mechanical properties

The goal of this study has been to evaluate the thermal and mechanical properties and correlate these with the manufacturing and performance requirements. Aluminum hydroxide reduces the z-CTE below the T_g but not as effectively above the T_g due to its decomposition. Silica is found to be more effective in suppressing the z-CTE above T_g and it prolongs the time to delamination. However, not only the type of filler used should be considered for optimizing the thermal properties, but also the thermal stability of the epoxy, which affects both CTE and time to delamination. The T_d at 1 wt% correlates with the time to delamination at 260ºC and they can be related to the reliability of the PCB. Materials with high T_d at 1, 2 and 5 wt% also exhibit good IST performance. Adding fillers in the laminates increases both the flexural modulus and Vickers hardness. The addition of silica leads to a decrease in energy to fracture and flexural strength for some materials.

In order to satisfy the manufacturing requirement and mechanical reliability of a handheld electronic device, a balance of both good thermal and mechanical properties are important. According to all the materials examined in this study, material E and F exhibit good thermal and mechanical properties which can make them candidates for halogen-free materials used in the device. In terms of the design aspects for halogen-free materials, the amount of fillers and the thermal stability of the epoxy are very important. Addition of silica can reduce the CTE and prolong time to delamination. However, it can also significantly reduce the energy to fracture and flexural strength. Therefore, the amount of silica

fillers must be optimized. Aluminum hydroxides are found to be thermally unstable above the T_g and it is recommended that other hydroxides can be used such as magnesium hydroxides. The epoxy in the halogen-free laminates must also be thermally stable in order to fulfill the manufacturing requirement.

Appendix

T_g measured by DSC method

Materials	Tg (DSC) in °C				
A	141.44	142.31	141.39	141.78	141.65
B	154.37	153.95	153.97	154.80	153.66
C	169.96	171.50	170.43	171.07	169.65
D	160.31	160.81	159.91	163.10	161.65
E	152.55	152.93	152.47	152.79	154.30
F	152.43	153.00	152.87	152.96	154.31
G	151.08	147.96	146.02	150.86	150.30

T_g measured by TMA method

Materials	Tg (TMA) in °C				
A	142.42	135.30	136.39	133.89	139.01
B	144.82	139.57	142.65	144.49	146.10
C	153.67	148.70	150.85	150.16	153.17
D	150.96	146.37	145.89	146.36	141.17
E	153.38	148.05	153.96	153.69	153.90
F	145.45	140.86	141.82	147.00	142.97
G	139.48	144.48	142.58	142.05	151.45

T_g measured by DMA method

Materials	Tg (DMA) in °C				
A	154.76	155.63	156.06	155.19	156.06
B	167.04	168.10	168.10	168.81	169.52
C	181.61	182.68	181.96	182.68	183.74
D	182.68	183.39	183.39	183.74	184.10
E	171.30	171.66	171.66	172.37	172.72
F	170.95	170.95	171.30	170.95	170.59
G	174.68	175.28	174.15	174.50	175.57

Z-axis CTE before T_g

Materials	z-CTE before Tg (ppm/°C)				
A	50.87	51.20	46.89	48.31	48.98
B	40.52	42.39	38.40	39.38	40.14
C	22.53	26.06	23.58	26.79	23.62
D	52.22	53.25	54.22	54.24	51.39
E	32.06	29.65	28.85	27.99	28.14
F	37.31	39.52	39.34	37.61	38.51
G	42.09	36.04	40.48	45.00	46.16

Z-axis CTE after T_g

Materials	z-CTE after Tg (ppm/°C)				
A	260.90	266.10	258.50	263.00	271.20
B	232.00	231.20	229.00	219.80	222.70
C	131.10	155.50	150.40	172.00	158.30
D	259.40	260.10	265.50	259.30	222.10
E	206.00	207.90	217.00	215.20	219.40
F	219.00	223.80	213.50	219.80	220.70
G	212.00	198.40	234.50	234.30	228.60

X-axis CTE before and after T_g

Materials	X-CTE before Tg (ppm/°C)			X-CTE after Tg (ppm/°C)		
A	14.72	15.57	14.34	12.97	10.92	11.19
B	14.67	15.12	14.09	12.04	13.85	12.42
C	14.08	13.96	13.39	12.86	13.12	8.13
D	13.65	15.64	15.24	13.16	15.43	14.41
E	14.71	14.28	15.20	14.15	14.06	16.07
F	14.08	15.19	14.62	13.92	15.20	14.24
G	16.63	14.83	15.13	15.20	16.14	12.34

Y-axis CTE before and after T_g

Materials	Y-CTE before Tg (ppm/°C)			Y-CTE after Tg (ppm/°C)		
A	14.57	14.88	14.64	12.47	14.89	14.49
B	14.27	14.86	14.22	13.50	12.69	11.04
C	14.46	15.21	14.18	13.43	15.86	14.84
D	16.21	16.19	17.14	15.60	13.33	14.91
E	14.27	14.98	14.88	13.27	13.30	14.02
F	15.20	14.60	14.57	13.88	13.48	13.36
G	15.73	14.04	15.05	17.37	17.80	16.53

Time to delamination at 260°C

Materials	T260 (mins)				
A	1.78	2.07	2.08	2.86	1.97
B	9.35	8.12	8.98	8.78	7.37
C	21.44	24.67	22.40	21.31	27.65
D	3.97	3.97	4.11	3.75	5.43
E	4.85	6.24	5.50	4.83	2.90
F	35.49	35.59	43.25	41.17	43.32
G	7.21	5.83	7.87	6.05	7.42

Time to delamination at 288°C

Materials	T288 (mins)				
A	0.00	0.00	0.00	0.00	0.00
B	0.09	0.80	1.41	0.45	0.27
C	1.16	2.03	1.56	1.60	0.73
D	0.00	0.00	0.00	0.00	0.00
E	0.00	0.00	0.00	0.00	0.00
F	2.47	2.57	2.95	2.62	3.19
G	0.53	0.22	0.69	0.00	0.00

Derivative weight change at 260°C

Materials	Derivative weight change at 260°C (%/°C)				
A	0.001536	0.001524	0.001455	0.001642	0.000845
B	0.000843	0.001909	0.001806	0.001292	0.001126
C	0.002383	0.00308	0.003383	0.003047	0.003127
D	0.006158	0.006863	0.006448	0.005644	0.006297
E	0.003917	0.004948	0.004454	0.004505	0.004809
F	0.001999	0.000808	0.002097	0.001966	0.001928
G	0.003437	0.003561	0.00296	0.00336	0.003363

Temperature to decomposition at 1wt% loss

Materials	Td 1wt% (°C)				
A	315.11	313.32	312.96	312.96	312.95
B	332.22	332.15	333.68	333.54	332.89
C	346.34	342.95	342.99	343.80	342.66
D	317.98	319.92	320.18	319.15	325.13
E	333.78	332.83	333.66	331.82	332.92
F	342.39	342.24	341.99	342.27	347.13
G	338.82	340.09	340.00	339.41	339.00

Temperature to decomposition at 2wt% loss

Materials	Td 2wt% (°C)				
A	316.93	321.65	317.41	317.46	318.47
B	334.74	334.76	336.14	335.97	332.22
C	355.16	352.75	352.82	353.38	352.88
D	334.47	335.00	335.92	335.48	338.95
E	347.77	347.24	346.89	345.72	346.83
F	357.56	357.91	357.50	357.76	361.21
G	357.92	359.50	357.66	358.99	358.58

Temperature to decomposition at 5wt% loss

Materials	Td 5wt% (°C)				
A	323.16	322.31	324.06	324.61	321.80
B	340.28	340.37	341.60	341.52	338.38
C	366.29	364.34	352.99	365.17	364.62
D	365.83	366.43	365.62	366.50	368.29
E	376.37	375.50	375.83	374.57	375.59
F	379.22	379.57	378.83	379.85	381.79
G	393.35	393.67	393.93	394.43	393.91

Interconnect stress test

Materials	IST (cycles to failure)				
A	63	77	60	96	96
D	90	97	76	87	90
E	273	268	163	192	112
G	1000	891	903	887	786

Flexural strength

Materials	Flexural strength (MPa)				
A	384.36	383.79	385.32	376.76	391.00
B	322.92	323.53	321.40	313.91	332.00
C	399.81	395.28	391.32	398.93	395.01
D	381.82	372.26	384.19	379.07	395.10
E	389.88	380.65	387.40	381.25	409.80
F	358.91	351.23	348.49	355.95	352.40
G	343.52	-	-	-	-

Energy to fracture

Materials	Energy to fracture (J)				
A	5.8	5.8	5.7	5	5.6
B	2.6	2.5	2.4	2.4	2.9
C	3.5	3.4	3.4	3.7	3.6
D	4.7	4.6	4.9	4.1	4.8
E	4.7	4.2	4.7	4.3	4
F	3.6	3.7	3.3	3.5	3.8
G	3.5	-	-	-	-

Flexural modulus

Materials	Flexural modulus (MPa)				
A	24333	23539	23839	24048	24517
B	27222	27298	27724	29161	26718
C	31025	32343	32670	32357	31653
D	27955	27559	29249	26346	29161
E	31823	28112	28213	29783	31552
F	27726	27776	25665	26281	28477
G	30915	28800	30434	30700	30188

Vickers hardness

Materials	Vickers Hardness (HV)									
A	18.3	19.8	17.7	18.3	16.5	17.1	17.8	17.6	18.3	18.5
B	22.4	22.0	23.8	21.3	24.5	23.3	23.2	20.1	21.0	22.4
C	51.0	49.2	52.3	49.2	49.9	36.0	56.8	54.6	47.8	50.8
D	32.5	33.2	30.1	30.5	33.6	31.3	33.7	32.7	31.4	33.3
E	27.8	30.7	30.6	28.0	28.1	30.4	27.5	29.5	29.5	27.6
F	28.4	27.8	29.1	28.0	29.0	28.2	27.0	27.9	28.8	26.4
G	37.9	37.0	33.7	35.2	31.7	37.8	36.5	36.0	37.9	32.8

Copper peel strength

Materials	Copper peel strength (N/mm)				
A	1.296	1.300	1.241	1.334	1.212
D	0.581	0.813	0.865	1.007	1.064
E	1.015	1.215	1.233	1.240	0.869
G	1.195	1.196	1.244	1.239	1.042

Dielectric constant at 3.2 GHz

Materials	Dk at 3.2GHz				
A	4.22	4.06	4.01	4.06	3.97
D	4.35	4.45	4.46	4.54	4.42
E	4.66	4.53	4.64	4.69	4.61
G	4.50	4.51	4.51	-	-

Dissipation factor at 3.2 GHz

Materials	Df at 3.2GHz ($x10^{-3}$)				
A	9.67	10.65	10.44	11.02	10.10
D	11.26	7.78	6.99	7.73	8.91
E	6.39	8.58	13.60	11.27	12.58
G	11.74	11.77	11.75	-	-

Reference

1 Whitley, A. (2008), "Dell marketing perspective on halogen-free electronics", paper presented at Intel IPC Halogen-Free Symposium

2 Na, J., Lee, T. (2008), "Novel halogen-free materials for organic packaging substrates", paper presented at Intel IPC Halogen-Free Symposium

3 Chen, W.Y., Wang, Y.Z., Chang, F.C., "Thermal and Flame Retardation Properties of Melamine Phosphate-Modified Epoxy Resins", Journal of Polymer Research, 2004, pp.109-117.

4 Bedner, D., "New Halogen-Free Materials Their Time Has Finally Arrived", Circuitree, 2008.

5 Olson, L.D., "Resins and Reinforcements", Electronic Materials Handbook, 1989

6 Döring, P. D., "Halogen-free Flame Retardants in E&E Application", Karlsruhe Germany: Forschungszentrum Karlsruhe GmbH, Oct 2007.

7 Jeng, R.J., Shau, S.M., Lin, J.J., Su, W.C., Chiu, Y.S., "Flmae retardant epoxy polymers based on all phosphorus-containing components", European Polymer Journal , 2002, pp.683-693.

8 Feinberg D., "To avoid commoditization, is PWB brand-awareness the answer?", Circuitree, 2004.

9 Waterman, P.J., "Designing handheld electronics for survival", Technology for Design Engineering, 2009.

10 Maxim, "Wafer-level packaging (WLP) and its applications", application note 1891, 2008

11 Adams, J. M., "Particles size and shape effects in materials science: examples from polymer and paper systems", Clay Minerals , 1993, pp.509-530.

12 Ramazani, S.A., Rahimi, A., Frounchi, M., Radman, S., "Investigation of flame retardancy and physical-mechanical properties of zinc borate and aluminum hydroxide propylene composites", Materials and Design 29, 2008, pp.1051-1056.

13 Xie, D., Wang, J., Yu, H., Lau, D., Shangguan, D., "Impact performance of microvia and buildup layer materials and its contribution to drop test failure", IEEE, 2007, pp.391-399.

14 Kelley, E. J., "Base material components", Printed Circuits Handbook 5th edition

15 Wong, C.P., Bollampally, R.S., “Thermal Conductivity, Elastic Modulus, and Coefficient of Thermal Expansion of Polymer Composites FIlled with Ceramic Particles for Electronic Packaging”, Jornal of Applied Polymer Science, 1999, pp.3396-3403.

16 Hoevel, B., Valette, l., Gan, J., “New epoxy resins for printed wiring board applications”, Circuit World, 2007, pp.17-27.

17 Iji, M., Kiuchi, Y., “Flame resistant glass-epoxy printed wiring boards with no halogen or phosphorus compounds”, Journal of Materials Science, 2004, pp.175-182.

18 Liu, Y. L., “Flame-retardant epoxy resins from novel phosphorus-containing novolac”, Polymer 42, 2001, pp.3445-3454.

19 Lamprecht, S., Heinz, G., Patoon, N., Kenny, S., Brooks, P., “Green PCB production processes”, Circuit World, 2008, pp.13-24.

20 Vollenberg, P.H.T., “The mechanical behaviour of particle filled thermoplastics”, PhD thesis, Technische Univ. Eindhoven, Netherlands, 1987.

21 Chen, Y.C., Lin, H.C., Lee, Y.D., “The effects of fillers content and size on the properties of PTFE/SiO2 composites”, Journal of polymer research, 2003, pp.247-258.

22 Rozman, H.D., Kon, B.K., Abusamah, A., Kumar, R.N., Ishak, Z.A.M., J. Appl. Polym. Sci., 69, 1993(1998).

23 Bigg, D.M., Polymer Composites, 8(2), 115(1987).

24 Liang, J.Z., Macromol. Mater. Eng., 287(9), 588(2002)

25 Marcovich, N.E., Aranguren, M.I., Reboredo, M.M., “Modified woodflour as thermoset fillers Part I. Effect of the chemical modification and percentage of filler on the mechanical properties”, Polymer 42(2001), pp.815-825

26 Kelly, E.J., “Properties of base materials”, Printed Circuits Handbook 6th edition

27 Roesh, M., Ehrler, S., “Laminate qualification and testing”, Printed Circuits Handbook 6th edition

28 IPC-TM-650 test methods manual 2.4.25, Glass transition temperature and cure factor by DSC

29 IPC-TM-650 test methods manual 2.4.24, Glass transition temperature and z-axis thermal expansion by TMA

30 IPC-TM-650 test methods manual 2.4.24.4, glass transition and modulus of materials used in high density interconnection (HDI) and microvioas – DMA method

31 IPC-TM-650 test methods manual 2.4.41, Coefficient of linear thermal expansion of electrical insulating materials

32 IPC-TM-650 test methods manual 2.4.24.1, Time to delamination (TMA method)

33 IPC-TM-650 test methods manual 2.4.24.6, Decomposition temperature (T_d) of laminate material using TGA

34 IPC-TM-650 test methods manual 2.6.26, DC current induced thermal cycling test

35 IPC-TM-650 test methods manual 2.4.4, Flexural strength of laminates (at ambient temperature)

36 Ziwick, R., www.zwick.co.uk/images/biege3lv.jpg

37 Roesch, M., Ehrler, S., "Laminate qualification and testing", Printed Circuits Handbook 5th edition

38 DMA, http://www.shindosc.co.kr/dma.htm

39 IPC-TM-650 test methods manual 2.4.8, Peel strength of metallic clad laminates

40 IPC-TM-650 test methods manual 2.5.5.1, Permittivity (dielectric constant) and loss tangent (dissipation factor) of insulating material at 1MHz (contacting electrode systems)

41 Kelley, E.J., "Introduction to base materials", Printed Circuits Handbook 6th edition

42 Holden, H.T., "Introduction to high-density interconnection (HDI) technology", Printed Circuits Handbook 6th edition

43 Berkeley lab, http://xdb.lbl.gov/Section1/Periodic_Table/X-ray_Elements.html

44 Kelly, E.J., "The impact of lead-free assembly on base materials", Printed Circuits Handbook 6th edition

45 St. Cry, V.A., "New laminates for high reliability printed circuit boards", Proceedings of IPC Technical Conference, Feb 2006

46 Vaughan, D.J., "Fiberglass reinforcement", Printed Circuit Board Materials handbook

47 Zequn, M., M. H., "An issue in time to delamination (T260) testing for PCBs", Electronic circuit world convention 10 technical conference proceedings, 2005.

48 Wang, C.S., Lin, C.H., "Synthesis and Properties of Phosphorus-Containing Epoxy Resins by Novel Method", Journal of Polymer Science, 1999, pp.3903-3909.

49 Wang, X., Lin, J., "A phosphate-based epoxy resin for flame retardance: synthesis, characterization, and cure properties", Colloid Polymer Science, 2005, pp.593-603.

50 Freda, M., "Via life vs. temperature stress analysis of interconnect stress test", CircuiTree Vol. 18 2005, pp.10-20.

51 Freda, M., Furlong, J., "Application of reliability/survival statistics to analyze interconnect stress test data to make life predicitions on complex, lead-free printed circuit board assemblies," EPC2004, 5 Oct. 2004, Cologne, Germany.

52 Freda, M., Furlong, J., "Advanced testing using real life evaluation and statistical data analysis," EPC2004, 5 Oct. 2004, Cologne, Germany.

53 Tardibuono, M.J., "Characterization of PCB plated-through-hole reliability using statistical analysis", Circuit World vol. 31 2004, pp.8-15.

54 Liu, A., Chen, J.I., "Reliability of high Tg copper clad laminate for lead-free assembly," Microsystems, Packaging, Assembly and Circuits Technology, 2007. IMPACT 2007. International

55 Kelly, E.J., "Base materials performance issues", Printed Circuits Handbook 6th

56 Mareri, P., Bastide, S., Binda, N., Crespy, A., "Mechanical behaviour of polypropylene composites containing fine mineral filler: effect of filler surface treatment", Composites Science and Technology, 1998, pp.747-752.

57 Hippi, U., Mattila, J., Korhonen, M., Seppala, J., "Compatibilization of polyethylene/aluminum hydroxide (PE/ATH) and polyethylene/magnesium hydroxide (PE/MH) composites with functionalized polyethylenes", Polymer 44, 2003, pp.1193-1201.

58 Watkowski, J., "Electroplating", Printed Circuits Handbook 6th

59 Rothon, R., "Mineral Fillers in Thermoplastics: filler Maufacture and Characterisation", Advances in Polymer Science, 1999, pp.67-109.

60 Verghese, N., "PCB drillability: a material science approach development", Circuit World, 2004, pp.44-51.

61 Low, I.M., Shi, C., “Vickers indentation response of epoxy polymers”, Journal of Materials Science Letters, 1998, pp.1181-1183.

62 Patton, N., “Lead/haloge-free lamiantes”, Circuit World Vol. 33, 2007, pp.28-35.